Universidad de Extremadura

TESIS DOCTORAL

DISEÑO DE CIRCUITOS CMOS DE BAJO CONSUMO PARA APLICACIONES BIOMÉDICAS BASADAS EN TÉCNICAS DE IMPEDANCIA BIOELÉCTRICA

Javier Ramos Maganés

Departamento de Ingeniería Eléctrica, Electrónica y Automática

Conformidad del/los Director/res:

Fdo: José Luis Ausín Sánchez **Fdo:** Juan Francisco Duque Carrillo

2015

Reviewed by

Professor Mart Min, Tallinn University of Technology, Estonia
Professor Clara-Helena González-Correa, Universidad de Caldas, Colombia
Professor Guido Torelli, University of Pavia, Italy

"A mi familia y amigos, por todo su cariño, apoyo y comprensión"

Agradecimientos

"Es de bien nacido ser agradecido", y no puedo más que empezar este documento dando las gracias. Gracias.

Gracias en general a todo aquel y todo aquello que se ha cruzado en mi camino durante todo este tiempo que ha durado la elaboración de este trabajo. Todos y todo han participado de la situación que se produce en este momento en el cual se procede a cerrar esta etapa.

En primer lugar me gustaría expresar mi más sincero agradecimiento a mis directores de tesis por todos sus consejos y enseñanzas, no solo en el ámbito académico y profesional sino también en el plano personal.

Gracias a todos los miembros del departamento de Ingeniería Eléctrica, Electrónica y Automática, y en particular a Ignacio Brinquete, José María Valverde, Miguel Ángel Domínguez, José Antonio Moreno, Juan Manuel Carrillo y Raquel Pérez-Aloe por poner amablemente sus conocimientos a mi disposición.

Gracias a mis compañeros Antonio Lorido y Javier Redondo, por hacer, durante el tiempo que hemos compartido juntos, un poquito más agradable, si es posible, el ambiente de trabajo en investigación.

Gracias a la Junta de Extremadura, la cual ha facilitado la realización de este trabajo doctoral poniendo medios a mi disposición para la ejecución y divulgación de las tareas necesarias para la finalización del mismo. Del mismo modo me gustaría agradecer al Ministerio de Economía y Competitividad la ayuda prestada a través del proyecto TEC2010-19019.

En lo personal, me gustaría agradecer a mis amigos su interés de corazón por mi trabajo doctoral y por mis estados de ánimo durante la realización del mismo. Tanto vosotros como yo sabemos bien quienes sois y lo que vuestra presencia ha aportado a este trabajo.

Para finalizar, gracias a mi familia por su apoyo constante y paciencia sin límites en este camino. Gracias por estar y saber estar a mi lado.

"Yo soy yo y mi circunstancia"

Ortega y Gasset

Outline

List of figures

Chapter 1

Chapter 2

Chapter 3

Chapter 4

Chapter 5

Chapter 6

Chapter 7

List of tables

Chapter 2

Chapter 3

Chapter 4

Chapter 5

Chapter 6

Chapter 7

Resumen

Durante décadas, la industria de los semiconductores ha creado circuitos integrados cada vez más potentes, tanto para la comunicación como para el procesado de señales. Máxima escalabilidad, integración compleja y multiplexación de señales han permitido dicha evolución. Se ha establecido la tendencia hacia procesadores más potentes y se han habilitado dispositivos móviles con aún más funcionalidades. De la misma manera que los circuitos integrados han revolucionado la industria de la electrónica, actualmente se encuentran afrontando el cambio demandado en el sector de la salud con la mejora de nuestra vida cotidiana a través de soluciones basadas en silicio.

La tecnología de los semiconductores permite a los diseñadores el desarollo de herramientas a escala microelectrónica que interactúen con la biología, del mismo modo que ofrece el potencial de reducir el coste de la asistencia sanitaria. A su vez, estas pequeñas herramientas microelectrónicas pueden ser integradas en aplicaciones heterogéneas, más rápidas y más inteligentes que las que se utilizan actualmente. Por otra parte, los ingenieros microelectrónicos pueden integrar varias funcionalidades en un solo chip, en lugar de precisar un equipo dedicado para cada tipo de test a realizar.

Hoy en día, estas funcionalidades pueden ser ejecutadas usando nada más que un teléfono inteligente, y que junto con la experiencia de diseñadores en el desarrollo de circuitos y sensores de ultra bajo consumo de energía, permitan la creación de dispositivos wearables que realicen la supervisión continua y prolongada de señales fisiológicas y biológicas. En este sentido, un área emergente en los nuevos métodos de prestación de asistencia sanitaria es el uso de tecnologías inalámbricas para

dispositivos médicos. Con tales instrumentos, la industria de dispositivos médicos se desplaza hacia un sistema de salud más personalizada, preventiva, predictiva y participativa. Esa es la razón por la que, tanto las ciencias de la vida como las compañías de cuidado de la salud están cada vez más interesadas en la soluciones personalizadas basadas en tecnologías CMOS, obteniendo así dispositivos útiles que mejoren la asistencia sanitaria.

Como se ha mencionado anteriormente, el tamaño y el consumo de energía establecen restricciones para los dispositivos encargados de enfrentarse a las nuevas tendencias en la asistencia sanitaria, las cuales implican que los diseñadores de microelectrónicos trabajen hacia circuitos y sistemas de bajo consumo eléctrico y de bajo voltaje de alimentación para el procesamiento de señales biomédicas, foco principal del trabajo que se detalla en este documento. En particular, las señales de bioimpedancia eléctrica, que producen una gran cantidad de información sobre los cambios de parámetros corporales durante diferentes tipos de actividades, son el objetivo de esta tesis. El diseño, la realización y la evaluación de un sistema inalámbrico de medición multicanal basado en un circuito integrado de aplicación específica de alto rendimiento para mediciones de bioimpedancia eléctrica en el rango de frecuencias que van desde 1 kHz a 1 MHz, es mostrado en los diferentes capítulos que componen este documento. El espectrómetro on-chip resultante, junto con circuitos de radiofrecuencia de bajo coste disponibles comercialmente, proporciona altas capacidades de medición y también constituye el nodo básico para redes de sensores inalámbricos basados en bioimpedancia. La solución propuesta se comporta como un espectrómetro multicanal e inalámbrico de bioimpedancia eléctrica de altas prestaciones, donde el número de nodos, es decir, el número de canales, es completamente escalable para satisfacer los requisitos específicos de las nuevas tendencias en el sector de la salud.

Abstract

For decades now, the semiconductor industry has created ever more powerful chips for computation and communication. Maximal scaling, complex integration, and extreme multiplexing have enabled this evolution. It has set the trend towards even more powerful computers and enabled mobile devices with even more functionalities. In the same way that chips have revolutionized the electronics industry, chips are facing the change of the current healthcare field improving our daily lives through silicon-based solutions.

Semiconductors allow designers to design microsized tools that interface with biology and, at the same time, they have the potential to allow reducing the cost of healthcare. They can integrate these small tools into heterogeneous applications, faster and more intelligently than the tools currently used. Moreover, microelectronics engineers can integrate several functionalities on a single chip, instead of having one bulky tool for every test.

Nowadays, these functionalities will be executed using nothing more than a smartphone, and together with the experience of designers in ultralow-power circuits and sensors, enabling the development of wearable devices that allow for continuous and long-term monitoring of physiological and biological signals. In this sense, one emerging area in the new methods of healthcare delivery is the use of wireless technologies for medical devices. With such instrumentation, the medical device industry shifts towards a more personalized, preventive, predictive, and participative healthcare system. That is the reason why life sciences and healthcare companies are

increasingly interested in customizing CMOS technologies to turn them into useful devices for improved healthcare.

As it has been mentioned above, size and power consumption constraints for devices facing new trends in healthcare involve semiconductors designers to work towards low-power, low-voltage circuits and systems for processing physiological signals, which comprises the main focus of the work detailed in this document. In particular, electrical bioimpedance signals, which produce a great deal of information about the changes of body parameters during different kinds of activities, are the aim of this thesis. The design, realization and evaluation of a wireless multichannel measurement system based on a cost-effective high-performance application specific integrated circuit for electrical bioimpedance measurements in the frequency range from 1 kHz to 1 MHz, are shown through the different chapters of this document. The resulting on-chip spectrometer, together with low-cost commercially available radio frequency transceiver devices, provides high measuring capabilities and also constitutes the basic node to built bioimpedance-based wireless sensor networks. The proposed solution behaves as a high-performance wireless multichannel electrical bioimpedance spectrometer where the number of nodes, i.e., number of channels, is completely scalable to satisfy specific requirements for the new healthcare trends.

Chapter 1

INTRODUCTION

A short overview of the current trends in healthcare and medical devices development, which constitute the motivation of this research, is carried out in this Chapter. In addition, the objectives of the work as well as the organization of this dissertation are addressed.

1.1. MOTIVATION OF THE RESEARCH

Life expectancy at birth is continuously increasing for the world population. In fact, it grew by 20 years between 1950-1955 and 2005-2010, from 48 years to 68 years (Fig. 1.1) [1.1]. As observed, the larger life expectancy occurs in the citizens of the developed countries. These demographic trends involve that, over the years, the elderly segment of population is representing a higher percentage of the total population and, therefore, more and more healthcare is required. On the other hand, along with the aging population, the high quality of life demanded by the population in general requires new healthcare programs where concepts like early detection of diseases, prognosis and prevention of illnesses, and pervasive and personalized healthcare are of great importance.

Meanwhile, even without the aforementioned demographic and social tendencies, healthcare is becoming more and more unaffordable as medical cost rises high rapidly. In addition, current economical trend pushes National Health Systems to face new healthcare demands with less financial resources.

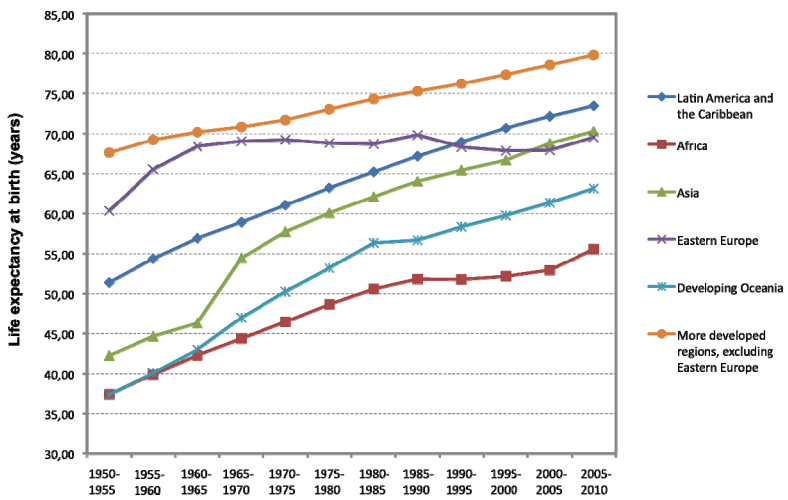

Figure 1.1. Life expectancy at birth, in selected regions, from 1950-1955 to 2005-2010.

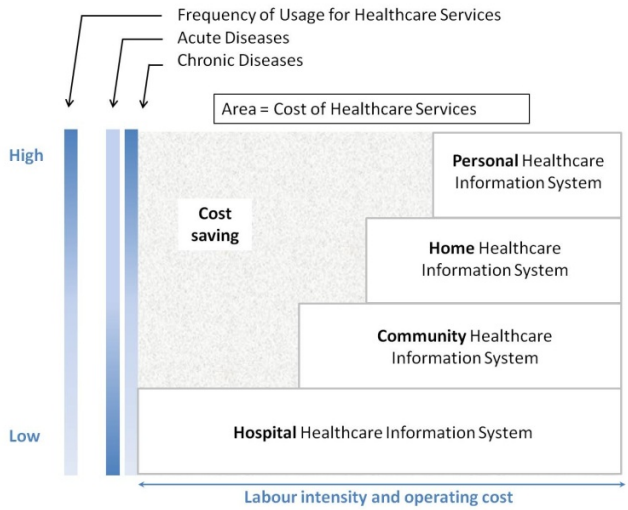

Figure 1.2. The PHCH four-layer architecture. Redrawn from [1.3].

In order to provide a satisfactory response to this social contrast, the definition of healthcare and the way it is delivered are currently undergoing a great change. In this sense, National Health Systems are being reorganized accordingly and low-cost medical devices for diagnosis and clinical assessment are being developed [1.2-1.4]. Figure 1.2 schematically illustrates an PHCH architecture[1], where the key point is the high frequency of use of medical resources of least cost in order to make highest cost resources to be used efficiently.

When compared to the traditional healthcare system, this four-layered PHCH structure allows the reduction of medical costs by optimizing labour resources. However, even more importantly from the point of view of the context of this work, the implementation of this kind of new and sustainable healthcare system structure claims the introduction of medical technologies and devices with some of the following characteristics:

[1] PHCH architecture: Personal Healthcare Information System (PHIS), Home Healthcare Information System (HHIS), Community Healthcare Information System (CHIS), Hospital Medical Information System (PHIS),

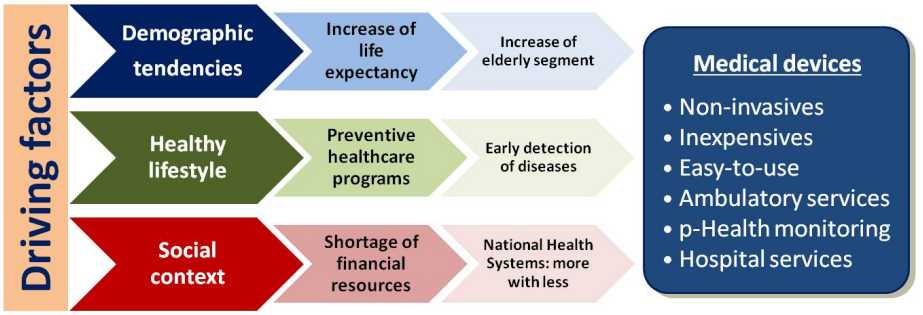

Figure 1.3. Current trends in medical devices for low-cost healthcare.

- being suited to be incorporated in daily ambulatory practice (Primary Healthcare Centers), instead of having a restricted use to hospital and specialized services which involves the necessity of being carried out by skilled technicians and/or with bulky and costly equipments;
- being suited to early detection and even for prognosis of diseases, which reduces the cost of therapies and treatments and simultaneously increases their effectiveness;
- being suited to be used at home –home monitoring– with specialized remote supervision, which reduces the number of visits to a healthcare center.

Considering a cost perspective, the primary goal of the above structure has its roots in moving healthcare away from where it is most expensive (clinic, emergency room) and moving toward preventative measurements and outpatient monitoring. The objective is to create technologies that will enable us to continuously monitor our health and track our progress in all stages of our life and disease. Future forms of medical interventions will likely involve not just pharmacology but also electronic devices. In the future, a treatment prescribed by a doctor will include both medicines as well as electronic devices –physiology sensors, mobile phones, wireless communications, etc.– [1.5, 1.6].

As Fig. 1.3 summarizes, medical devices with features such as being innocuous, autonomous, wireless, easy-to-use even by the own patient, and able to early detect alterations in structure and functionality of organs and tissues and assess the effectiveness of therapies and treatments are highly demanded for the future medical scenario, where the traditional concept of *Managing Illness* wants to be replaced by the concept of *Managing Health* [1.7]. Consequently, terms such as Personal Healthcare (p-Health), Home Monitoring, Wearable/Implantable Medical Devices, Non-invasive Medical Technologies, etc., involve a field of research with increasing activity and are currently associated to interesting business chances for healthcare providers.

1.2. OBJECTIVES OF THE WORK

Electrical bioimpedance (EBI) technology is a technique that partially provides adequate responses to the challenges pointed out in the above Section [1.8-1.13]. This will be seen in more detail in Chapter 2, where the fundamental basis of this technology, its advantages and constraints, as well as the main application fields that are of interest in the context of this work, are described.

According to the considerations indicated in Section 1.1, the main objective of this thesis consists in establishing the first steps for the realization of an EBI technological platform, which apart from taking advantage of the general features of this technology, includes the following characteristics:

- the technology platform should be adequate for a number of applications suitable for the consumer/patient context and also for the professional context;
- for EBI-based devices at the customer/patient level, the technology platform should be lightweight, reduced size, cost-effective, and autonomous;
- for EBI-based devices at the professional level, the technology platform should provide high performance.

For a number of *in-vivo* clinical uses, many existing EBI devices are not practical. Significant physical size and weight, as well as non-optimized power consumption, are common characteristics of traditional EBI measurement systems. In addition, many systems need to combine several instruments to form the measurement equipment –i.e., often a PC is required for acquiring the response data for further processing and acting as a controller–. These requirements strongly limit the portability and mobility of EBI applications and, of course, are useless for the development of modern wearable devices for EBI measurements/monitoring.

Therefore, a feasible technological alternative to simultaneously fulfill the above requirements necessarily consists in carrying out a cost-effective silicon realization of a programmable high-performance EBI sensor (AFE, analog-front-end). Based on this core, and adequately combined with other electronic components or devices, a high-performance and configurable EBI spectrometer, which occupies a printed circuit board of few square centimeters, is the basic node of a technological platform for efficient realization of EBI applications as well as the development of new ones.

Concretely, the specific objectives of this thesis are the following:

- design, fabrication, and test of a low-power high-performance on-chip EBI sensor with measuring ranges to cover the magnitude and phase angle variations in living organisms in the frequency band of interest and also, suitable for wearable and present future EBI applications;
- combination of the above full-custom CMOS AFE circuit with RF technology to generate the basic node that allow building scalable and flexible EBI wireless sensor networks (WSNs);
- realization of a EBI-WSN development system as a powerful tool able of providing adequate response to the requirements of a number of EBI applications as well as many other today unknown.

Finally, it should be pointed out that, even though the main application field of the developed EBI platform is within the area of medical devices, its use is not limited to this field. In fact, although out of the scope of this work, other fields like technology foods, microbiology and/or civil engineering can benefit of this technology through the development of interesting applications.

1.3. ORGANIZATION OF THE THESIS

In this Chapter, the current driving forces of healthcare systems and medical devices have been introduced. Also, the motivation and the objectives of the research have been addressed.

The rest of this dissertation has been organized as follows.

Chapter 2 accounts for the fundamentals of EBI technology. In particular, it starts describing the main features of biological materials from the electrical behavior point of view. The basic operation principles of mainly used for EBI measurements are concisely described. Next, the monolithic EBI sensors that can be found in literature, as well as the commercial available solutions, are provided. Multisite bioimpedance measurements at different body locations –multichannel measurements– are promising techniques for monitoring complex physiological events. Traditional solutions for multichannel measurements are also revisited. The Chapter concludes with an overview of clinical applications of the electrical bioimpedance technology from a critic point of view and finally, gives a review of the different on-chip EBI measurement instruments that have been reported.

Chapter 3 deals with a more complete description of the technological platform where the present work is encompassed. In addition, due to its relevance in the context of this dissertation, the Chapter provides the basics of EBI technology as an emerging technique for healthcare applications as wireless sensor networks are. Finally, the operation principle of the developed EBI sensor is described based on a general block diagram of the chip.

Next, Chapters 4, 5, and 6 correspond to the microelectronic design section of the thesis. These Chapters respond to a common structure but deal with different main electronic functional blocks of the CMOS EBI sensor –namely, instrumentation amplifier, gain/phase detector, and AC excitation current source, respectively–. Measured and simulated results illustrative of their performance are also provided.

The experimental performance of the implemented system is presented in Chapter 7. Specifically, this Chapter includes the experimental behavior of the CMOS EBI sensor as well as EBI spectrometer. Also, the Chapter deals with the implementation of the wireless node for EBI-WSN realizations as well as the developed technology platform for EBI applications. The main conclusions of this work and closing remarks are drawn in Chapter 8.

Finally, a formal consideration must be mentioned regarding the organization of references in this work. Besides the complete list of references at the end of this dissertation, in order to facilitate its reading it has been considered appropriate to include the corresponding reference list at the end of each Chapter and according to the following criterion. The references in the text are denoted by two figures within square brackets. The first one corresponds to the number of the chapter where the reference is listed and the second one indicates the order in the list.

1.4. REFERENCES

[1.1] United Nations, Population Facts: Towards global equity and longevity, Population Facts, No. 2012/2, April 2012. Available: http://www.un.org/esa/population/publications/popfacts/popfacts__2012-2.pdf

[1.2] Y. T. Zhang and C. C. Y. Poon, "Innovative biomedical information technologies for low cost healthcare," *6th International Special Topic Conference on Information Technologies Applications on Biomedicine*, pp. 64-65, Nov. 2007.

[1.3] C. C. Y. Poon and Y.–T. Zhang, "Perspectives on high technologies for low–cost healthcare. The Chinese scenario," *IEEE Engineering in Medicine and Biology Magazine*, pp. 42-47, September/October 2008.

[1.4] E. Mosslialos, M. Wenzl, R. Osborn, and C. Anderson, "International Profiles of Health Care Systems, 2014," *The Commonwealth Fund*, Jan. 2015.

[1.5] R. R. Fletcher, M.–Z. Poh, and H. Eydgahi, "Wearable sensors: opportunities and challenges for low-cost health care," *Proceedings of the 32nd Annual International Conference of the IEEE Engineering in Medicine and Biology Society (EMBS)*, pp. 1763-1766, Sept. 2010.

[1.6] R. Allan, "Get your prescription for personal medical electronics," *Electronic Design*, pp. 14-23, 2013.

[1.7] A. Honka, K. Kaipainen, H. Hietala, and N. Saranummi, "Rethinking health: ICT-enabled services to empower people to manage their health," *IEEE Reviews in Biomedical Engineering*, vol. 4, pp. 119-140, 2011.

[1.8] U. Mulasi *et al.*, "Bioimpedance at the bedside: current applications, limitations, and opportunities," *Nutrition in Clinical Practice*, vol. 30, pp. 180-193, April 2015.

[1.9] R. Bayford and A. Tizzard, "Bioimpedance imaging: an overview of potential clinical applications," *Analyst,* vol. 137, pp. 4635-4643, 2012.

[1.10] S. F. Khalil, M. S.Mohktar, and F. Ibrahim, "The theory and fundamentals of bioimpedance analysis in clinical status monitoring and diagnosis of diseases," *Sensors*, vol. 14. pp. 10895-10928, 2014.

[1.11] T. Kanti Bera, "Bioelectrical impedance methods for noninvasive health monitoring: a review," *Journal of Medical Engineering*, 28 pages, http://dx.doi.org/10.1155/2014/381251, 2014.

[1.12] F. G. F. Mitchell, "Clinical achievements of impedance analysis," *Med. Biol. Eng. Comput*., vol. 47, pp. 153-163, 2009.

[1.13] T. Maheshwari and N. Bhardwaj, "Bioelectrical impedance analysis: A healthcare technology of the future," *International Journal of Enhanced in Science Technology & Engineering*, vol. 3, pp. 102-110, 2014.

Chapter 2

ELECTRICAL BIOIMPEDANCE TECHNOLOGY

This Chapter deals with the basic fundamentals of EBI technology. In particular, the physiological structure of living organisms from the electrical behavior point of view, as well as the operation principles for EBI measuring and clinical application fields, are revisited. Finally, the Chapter occupies of the state of the art of monolithic realizations for electrical bioimpedance measurements.

2.1. FUNDAMENTALS OF EBI TECHNOLOGY

The term *electrical bioimpedance*, or simply *bioimpedance*, refers to all methods based on the study of the passive electrical properties of biological tissues. The passive electrical properties of biological tissues are determined through their response to the injection of external electrical energy. In other words, tissues are characterized as if they were electrical circuits made up of resistors, capacitors, and inductors, although some biological tissues, i.e., nerves, show active electrical properties since they are capable of generating electrical potentials [2.1].

The level of electrical signals in EBI technology remains always below the corresponding perception threshold of living beings without causing any negative effects, in such a way that the technology can be used even in neonates. In this sense, EBI technology presents outstanding advantages as the following:

- it is innocuous (non-invasive, non-destructive, non-ionizing);
- equipments are relatively inexpensive;
- it is easy-to-use, rapid, and portable.

These features are in the same direction as the current trends of healthcare programs and medical devices described in Chapter 1 (see Fig. 1.3), although this is not the only application field of EBI technology, as will be seen in the next section. As a consequence, new medical EBI applications, as well as refinement of other existing techniques, are continuously being reported[1]. However, the need for further research on EBI technology has also been confirmed in specialized forums stating that a vast

[1] A survey of publications on BIA (Bioimpedance Analysis), retrieved by using Boolean methods through the internet database 'PubMed', revealed that the number of papers per annum from 1990 to 2000 increased seven-fold, and continues to rise at an annual growth rate of nearly 22% [2.2].

number of questions still need adequate response and the full range of EBI applications has not yet been investigated.

The basic idea of EBI technology consists in injecting a low-amplitude alternating electrical current –i.e., less than 1 mA_{rms}, although higher values can be found in some applications– between two specific points of the *in-vivo* biological material and measuring the resulting voltages in other two points. Depending on the EBI measuring technique, these two monitoring points can coincide or not with the injection points. The frequency range of the excitation current goes from a few hundreds of Hz to several MHz –e.g., 1 kHz to 1 MHz is a typical frequency range– since, as will be seen below, this range corresponds to the most interesting physiological conditions and events related with tissues and cell membranes, which determine the electrical behavior of the biological tissue.

In particular, a biological tissue can be understood as a group of similar cells and associated intracellular matter acting together to perform specific functions in an organism. The cell is therefore the basic unit of living tissues. In healthy tissues, the basic structure of a cell consists of a semipermeable phospholipid bi-layer (cell membrane) with a thickness of 5-10 nm that physically separates the intracellular components and the extracellular medium.

Apart from acting as a physical separation barrier (passive role), cell membrane has an active role, which consists in selectively controlling the exchange of different chemical species. In particular, it allows lipids and water molecules to pass through it but, in principle, is a complete barrier for ions.

In the bi-layer lipid membrane, there are embedded proteins, transport organelles, ionic channels, and ionic pumps. Regarding to the membrane active role, the following elements are of particular interest:

- *Ionic channels* — they are porous structures that allow some ions to flow from the outside to the inside of the cell and vice versa or to flow from one cell to another one (gap junctions);
- *Ionic pumps* — they are energy-consuming structures that force some ions to flow through the membrane.

From the electrical behavior point of view, a cell membrane is a low-conductivity material and can be assumed as a dielectric material. Both intracellular and extracellular mediums can be considered as liquid electrolytes (ionic solutions) with similar ionic concentration values although with different types of ions and charged molecules [2.3]. Therefore, the structure formed by the extracellular medium, the cell membrane, and the intracellular medium is a conductor-dielectric-conductor structure and behaves as a capacitor, C_m, with a capacitance density of 1 μF/cm^2, approximately.

Figure 2.1 illustrates the main constituents of the cell membrane as well as its equivalent electrical circuit. The resistor in parallel with the capacitor, R_m, represents the current flow through the ionic channels of the cell membrane depicted in Fig. 2.1 (a). According to the above considerations a simple electrical circuit of a cell is depicted in Fig. 2.1 (b). The current injected into the extracellular medium can flow in the cell through the membrane capacitor (C_m) or through the ionic channels (R_m) or can also circulate around the cell (R_e). Once the current enters the cell, it flows through the intracellular medium, which is represented by resistor R_i, and leaves the cell through the membrane represented by the parallel combination $R_m||C_m$. The same circuit can be used to represent a tissue composed by many cells. The above equivalent circuit can be further simplified if the membrane conductance, which is very low (R_m is a very high value), is neglected. If so, the resulting equivalent circuit, widely known as *2R-1C* circuit, is rather simple and an acceptable deviation from the non-simplified circuit exists (Fig. 2.1 (c)).

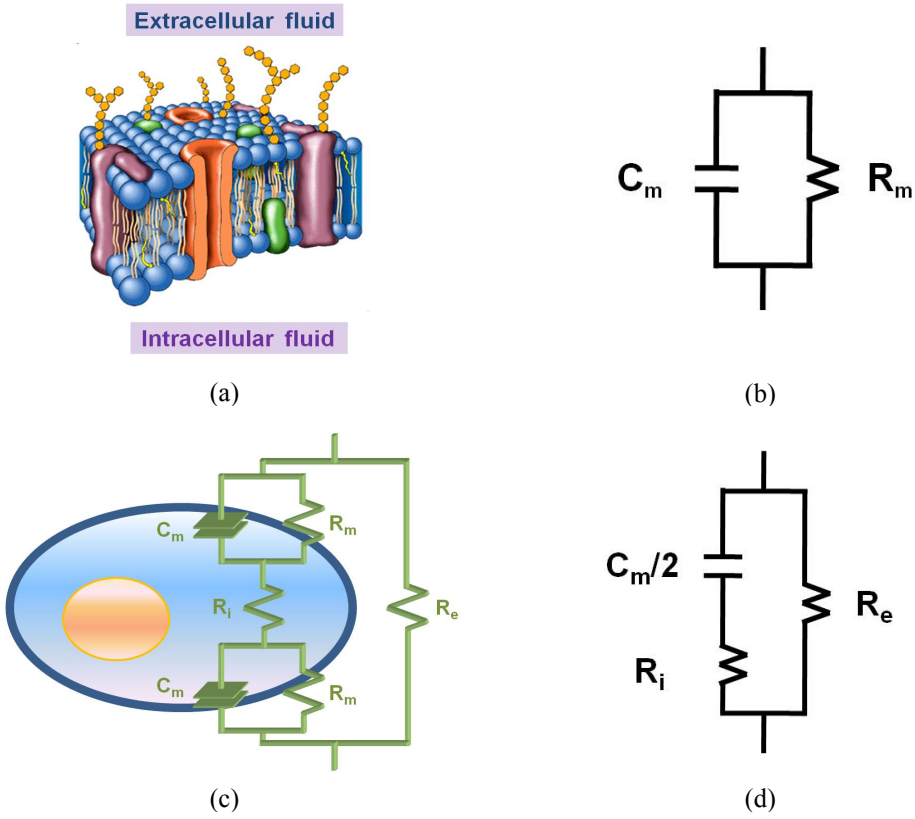

Figure 2.1. a) Membrane cell drawing. Redrawn from [2.4]; b) Electrical model of the cell membrane. R_m is the membrane resistance; C_m is the membrane capacitance; c) Equivalent circuit of a single cell in the extracellular medium. R_e is the extracellular fluid resistance; R_i is the intracellular fluid resistance and d) Simplified equivalent circuit (*2R-1C*) of a single cell in the extracellular medium.

This circuit model is adopted by most authors and explains the bioimpedance behavior from a few hundred of Hz to some tens of MHz. Thus, at low frequencies (< 1 kHz) the most important current paths are found through the extracellular environment due to the fact that the current is not able to penetrate the cells. On the contrary, as it is illustrated in Fig. 2.2, the electrical current penetrates the cell membranes and flows through both the intra- and the extra-cellular environment for higher frequencies up to 1 MHz.

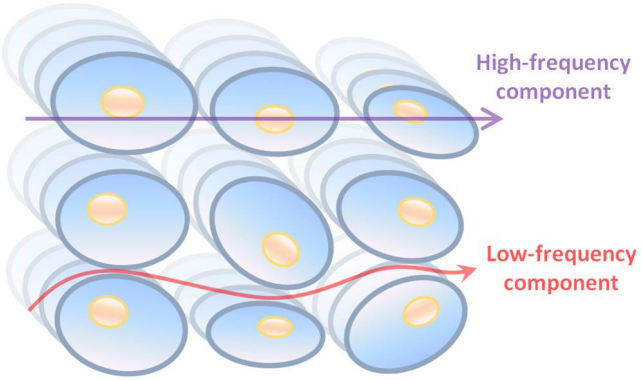

Figure 2.2. Current paths for low and high frequencies.

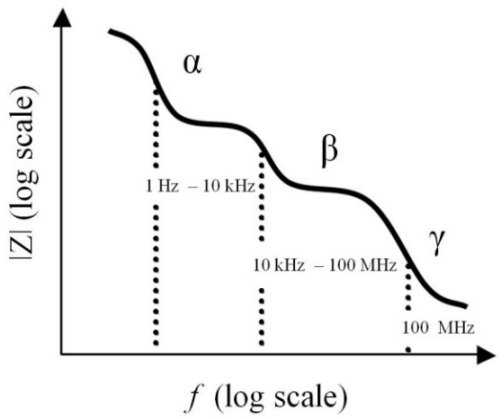

Figure 2.3. Main dispersion regions of the magnitude of the electrical impedance of a biological material.

In addition to the above-mentioned frequency range where the electrical bioimpedance magnitude decreases when the frequency increases, there are other different frequency regions where impedance decreases with increasing frequency. Figure 2.3 illustrates such behavior as well as the respective frequency ranges. These regions are known as *dispersions*, and each one responds to a specific electrochemical process or phenomenon.

Three dispersion regions –namely, the α-, the β-, and the γ-dispersion region– can be observed in Fig. 2.3. α-dispersion is mainly associated with the diffusion processes of the ionic species, and C_m presents great opposition to the current flow inside the cell. β-dispersion is associated to the dielectric properties of cell membranes and their interactions with intra- and extra-cellular electrolytes, where C_m admittance has enough value to allow electric current to penetrate the cell. Finally, the γ-dispersion reflects relaxation of water and other small molecules and C_m impedance contribution is negligible. It is important to notice that most of the clinically relevant information of tissues is contained in the frequency range corresponding to β-dispersion region.

According to the above considerations, the parameters of the complex electrical bioimpedance, $Z = |Z|e^{j\theta} = R + jX_C$, carry different information about the biological material under EBI test. Thus, the following characteristics can be derived from the bioimpedance components in a EBI analysis [2.2]:

- the impedance magnitude ($|Z|$) is a measurement of the overall opposition to conduct the electrical current through a biological medium, with resistive *(R)* and reactive *(X_c)* components;
- the impedance phase angle (θ) is proportional to the reactance (X_c) and C_m, and is therefore an indicator of the cellular membrane integrity and cellular health. In particular, phase angle is proportional to the ratio of reactance and resistance.

2.2. EBI MEASURING SYSTEMS

2.2.1. Two- and four-electrode electrical bioimpedance measurements

As previously mentioned, EBI technology consists in the characterization of a biological material in terms of its electrical impedance measured over a wide frequency range. In particular, bioimpedance is obtained by the ratio between measured voltage across two points when a current is injected into the biological material. Needless to say, the placement of injection and measuring points has a crucial importance for measurement results.

Electrodes are always necessary in EBI systems in order to make adequate electrical contacts with the biological material for injecting the predetermined current and measuring the ensuing voltage, because they represent the physical connections for injecting the stimulus and collecting the response signal with the biological information. The geometry and the number of electrodes used to perform an EBI measurement have an important influence on the obtained results [2.5].

In [2.6], it is established that the physical effect that occurs when a current is injected into a semi-infinite homogenous medium of conductivity σ, in our case the biological tissue, by a perfect hemispherical conductor, i.e., the electrode, is the generation of a potential V set up by the injected current I as depicted in Fig. 2.4, which can be obtained by means of the following expression:

$$V = \frac{I \cdot \rho}{2 \cdot \pi \cdot r} \tag{2.1}$$

where $\rho = 1/\sigma$ represents the electrical resistivity of the medium under study and r stands for the radius of the electrode.

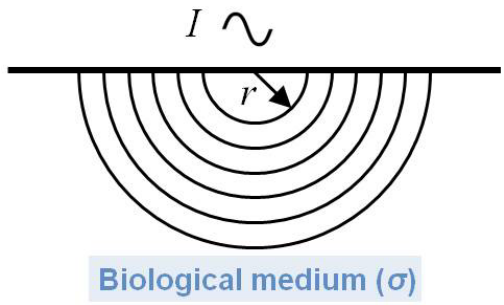

Figure 2.4. Representation of the equipotential lines developed when an electrode is placed in contact with a volume conductor. Redrawn from [2.6].

The value of the impedance which comes from applying the electrode to the biological tissue can be derived directly from Eq. (2.1). As a result, the electrode-to-tissue interface impedance Z_e, hereinafter also briefly referred to as electrode impedance, can then be derived by considering the electrode as a small hemisphere of radius $(a/2\pi)^{1/2}$, where a accounts for the area of the electrode. That is,

$$Z_e = \frac{\rho}{\sqrt{2 \cdot \pi \cdot a}} \tag{2.2}$$

An additional point to take into account concerning the electrodes for current injection is the relation between the penetration depth of the current into the biological material and the excitation frequency, the size of and the distance between electrodes, and the physical properties of the tissue under study [2.7, 2.8]. The penetration depth of the currents can be assumed to be approximately half the distance between the electrodes, as shown in Fig. 2.5. At the same time, high frequencies penetrate deeper than lower frequencies [2.6].

Apart from the physical effects associated to the use of electrodes for EBI measurements, there is a crucial issue regarding the number of electrodes involved in

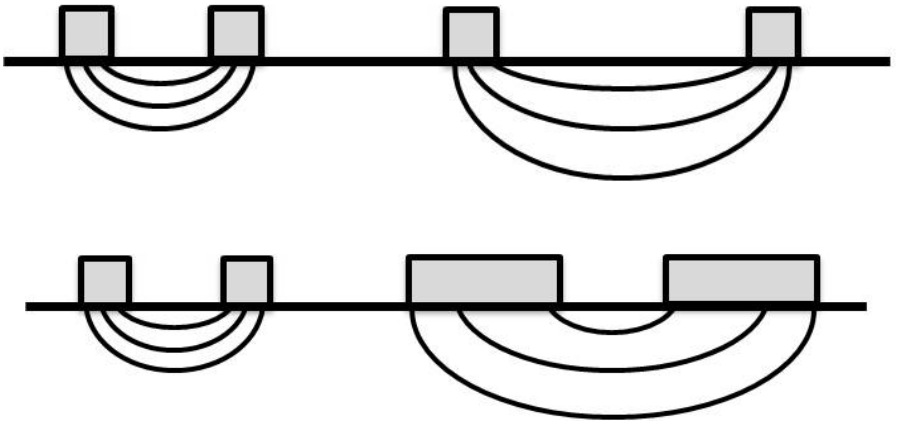

Figure 2.5. Penetration depth of current into the biological material related to the size and the distance between injection electrodes. Redrawn from [2.1].

an EBI measuring system. There are several techniques using two, three, or four electrodes [2.1], however, in this section, only the two most widely used techniques, namely the two- (*bipolar*) and the four- (*tetrapolar*) electrode technique, are concisely examined.

In the bipolar impedance method, a current source with an output impedance Z_{out} , injects an alternating current source, I_{exc}, through a pair of electrodes, Z_e, and, the impedance-dependent voltage appearing across these electrodes, V_x, is measured with an instrument (a differential amplifier) having a high-input impedance with respect to the sum of the two electrode impedances and the impedance of the tissue between the electrodes, Z_x. That is, the two electrodes are simultaneously used for sensing and stimulating, as illustrated in Fig. 2.6.

The ideal differential amplifier measures the voltage caused by the current flowing through the biological tissue and, in addition, the voltage created by the current flowing through the electrode. Taking into account the typical high value of Z_{out}, it can be easily derived that the measured impedance Z_m is given by the following expression:

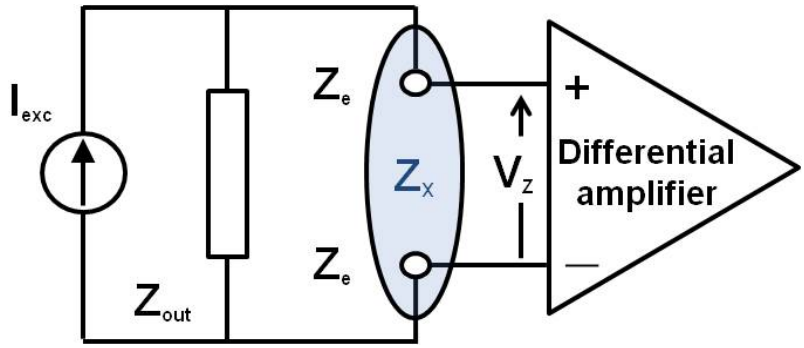

Figure 2.6. Bipolar impedance measurement technique scheme.

$$Z_m = \frac{V_X}{I_{exc}} = Z_X + 2Z_e \tag{2.3}$$

where Z_X accounts for the impedance of the biological tissue.

It can be derived from the previous equation that bipolar method involves ambiguity in the impedance measurement, because it is not possible to separate the contribution of the electrode impedance from the whole voltage V_m measured by the differential amplifier of the sensing circuit.

In 1884 [2.9], Bouty was the first in utilizing a pair of electrodes for injecting current –current-injecting or excitation electrodes– and a second pair of electrodes, placed between the current-injecting electrodes, for measuring the impedance-dependent voltage –voltage-sensing or sensing electrodes– during his researches in the determination of the resistivity of electrolytes. This corresponds to the basis of the four-electrode technique for measuring impedance, also called tetrapolar system, where two electrodes are used for injecting and collecting the excitation current and other two electrodes are used as sensing electrodes. The tetrapolar measurement technique can be represented by the equivalent electrical circuit in Fig. 2.7.

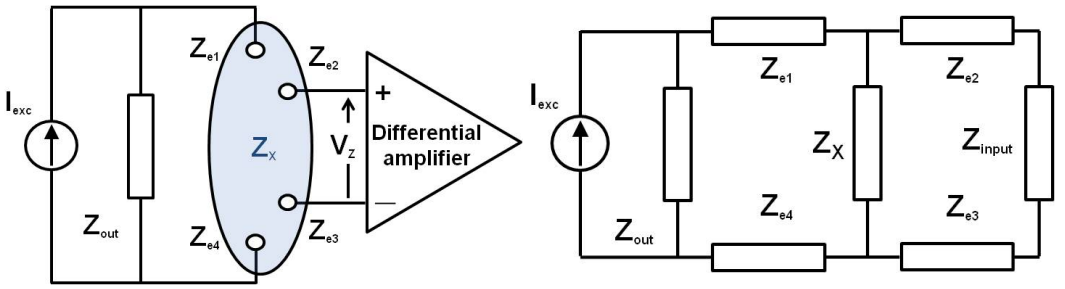

(a) (b)

Figure 2.7. a) Four-electrode impedance measurement technique scheme and b) its equivalent electrical circuit.

By assuming equal electrode impedances, i.e. $Z_{e1} = Z_{e2} = Z_{e3} = Z_{e4} = Z_e$ in Fig. 2.7, the measured impedance, Z_m, i.e., $(v^+ - v^-)/I_{exc}$, can be evaluated according to the expression [2.6]:

$$Z_m = \frac{Z_X}{1 + Z_X \cdot \left[\frac{4Z_e + Z_{OUT} + Z_{input}}{Z_{OUT} \cdot Z_{input}}\right] + 2Z_e \cdot \left[\frac{2Z_e + Z_{OUT} + Z_{input}}{Z_{OUT} \cdot Z_{input}}\right]} \quad (2.4)$$

where Z_{input} corresponds the input impedance of the differential amplifier that senses the voltage signal.

This tetrapolar method is relatively insensitive to changes in the electrode/tissue impedance of both voltage-sensing and current-injecting electrodes [2.6], [2.10] as Eq. (2.4) states. The tetrapolar technique can, in an ideal case, eliminate the effect of the electrodes on the measurement, which involves that the measured impedance equals the biological tissue impedance of interest, i.e., $Z_m = Z_X$. The insensitivity conditions of the four-electrode measurement are satisfied when the output impedance of the current generator, Z_{out}, and the input impedance of the differential amplifier, Z_{input}, are large

when compared with the sum of the electrode and tissue impedances, which involves the terms in the denominator of Eq. (2.4) affected by the product $Z_{out} \cdot Z_{input}$ to be negligible.

However, there is a disadvantage of the tetrapolar method. Because of the fact that the voltage-sensing electrodes are placed between the current-injecting electrodes, the biological material under analysis acts as a voltage divider and the voltage appearing across the sensing electrodes is less than that across the current-injecting electrodes. Consequently, the measured impedance signal is reduced, which must be taken into account when selecting the area of interest and placing the sensing electrodes for measuring the bioimpedance. Another point to be considered is that the four-electrode approach does not prevent the effect of stray capacitances that provide the injected current with a possible separate path different from the expected one.

2.2.2. Principle of operation for EBI measurements

Electrical bioimpedance measurements have been used since the late 1800s in order to determine the electrical properties of biologic tissue or extract biological information. Instrumentation techniques used for complex impedance measurements have been previously reviewed in several research works [2.11, 2.12], since the first electrical impedance measurements over human body were performed (1932) [2.13]. In this case, the measuring method consisted on a radiofrequency resonant circuit, being the human body the dielectric of a capacitance, in order to determinate the cardiac stroke volume. However, the beginning of modern clinical applications of EBI measurements can be attributed, in large part, to the reports by Nyboer concerning the determination of variations in size of organs or body parts on the basis of the amount of blood passing through or present in the part [2.14-2.16].

In particular, the most common electrical bioimpedance measurements can be classified as follows:

- Frequency domain analysis *Z(ω)*: The frequency response of a single wide-spectrum excitation signal or several individual frequency components provides detailed information about the composition of organic matter. This also known as EBI spectroscopy;
- Time domain analysis *Z(t)*: Typically, time-domain bioimpedance measurements are based on a single-frequency excitation signal –EBI analysis– . Tracking the variations in bioimpedance magnitude and phase angle over time enables the extraction of variations in tissue/organ compositions or dynamic parameters. For many situations, variations in magnitude $|Z(t)|$ have been sufficient. However, recently, variations in phase angle –bioreactance– have been shown to represent a more sensitive monitoring parameter since they also provides a much better signal-to-noise ratio and also, they are less susceptible to detection problems because they do not degrade with the distance between detecting electrodes [2.17, 2.18].

The way to measure the electrical bioimpedance does not differ from the conventional impedance measuring, which consists of supplying a small alternating current signal, and measuring the variation in the voltage, then the impedance is calculated with the amplitude and phase changes between the original signal and the recorded one.

During several years, the two-electrode Wheatstone bridge method had traditionally been the most commonly used instrumentation technique applied to biological material for electrical impedance measurements, providing the major advantage of high measurement resolution and accuracy. The principle of bridge measurement is well

known. Basically, it consists in placing an unknown impedance sample in series with an adjustable bridge arm, and obtaining a null current by adjusting the resistive and capacitive components of the bridge. Considerations regarding several bridge configurations, accuracy, and resolution for measurements in biologic tissues as well as special considerations for several frequency ranges have been presented in detail [2.11], [2.19].

As previously mentioned, the major advantages of a bridge measurement are the high resolution and accuracy that can be attained. This is particularly valuable since much biological material, with a predominant water component, is highly conductive, thus resulting in a small reactive component to real component ratio, which entails phase angles of less than 10° over a wide frequency range. However, an important disadvantage of the bridge method is that the measurements are time consuming due to the need for bridge balance. So, this is not the most suitable measurement method for tissues in which impedance changes in time due to ongoing physiological processes or for real-time monitoring applications, which involve a continuous record of variable complex electrical bioimpedance. Another disadvantage of the above mentioned two-electrode bridge method, which is common to any two-electrode impedance measurement system, refers to the fact that the measured impedance values are the sum of the impedance of the sample under test itself and the electrode impedance.

As a consequence of the bridge method drawbacks, an alternative technique for measuring complex electrical bioimpedance was developed with the aim of allowing continuous monitoring. This technique is widely known as phase-sensitive detection (PSD) or analog-quadrature demodulation (AQD), and has become the preferred method in modern electrical bioimpedance measurement systems [2.20-2.22].

A basic architecture of the AQD method based on the four-electrode structure is shown in Fig. 2.8, in which two current electrodes are used for AC current injection and two voltage electrodes for AC voltage signal detection. The operation principle of

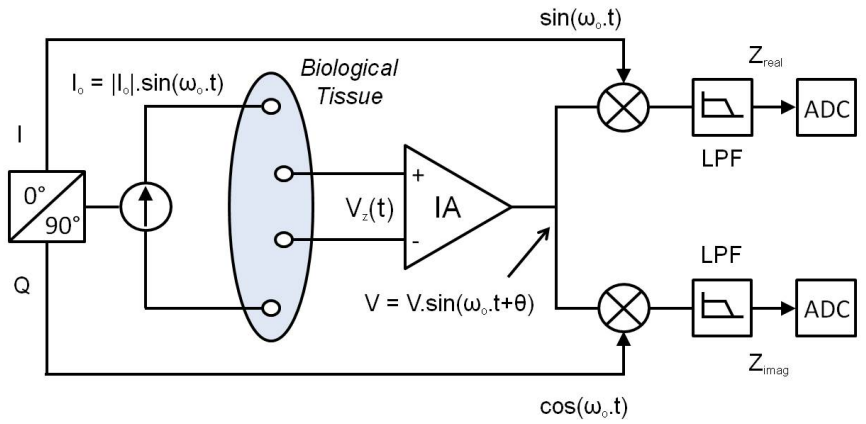

Figure 2.8. Block diagram of the conventional analog quadrature demodulation (AQD) method based on a tetrapolar structure.

this approach has its roots in the two-phase reference coherent demodulation method [2.20]. The voltage across the sensing electrodes is

$$v_z(t) = Z \cdot I_0 \cdot \sin(\omega_o t + \theta) \tag{2.5}$$

The output of the instrumentation amplifier (IA), $v(t)$, can be presented as

$$v(t) = V \cdot \sin(\omega_o t + \theta) = V \cdot \cos\theta \cdot \sin(\omega_o t) + V \cdot \sin\theta \cdot \cos(\omega_o t) \tag{2.6}$$

Then, the $v(t)$ signal is multiplied with the in-phase [$\sin(\omega_o t)$] and the quadrature [$\cos(\omega_o t)$] reference signal components, respectively. By using the formulas for the product of sine and cosine, it is straightforward derived that the demodulated in-phase and quadrature DC voltage levels obtained at the demodulator outputs are proportional to the real and the imaginary components of the unknown impedance, respectively: $Z_{real} \propto (V \cdot \cos\theta / I_0)$, $Z_{imag} \propto (V \cdot \sin\theta / I_0)$. The use of a low-pass filter enables extracting

these DC voltages, which can be sampled and converted by analog-to-digital converters (ADCs) for further processing.

Practical implementation of the AQD method relies on two channels in which the analog components and the in-phase and the quadrature references must be extremely well matched. As shown in Fig. 2.8, each channel includes an analog demodulator followed by a low-pass filter and an ADC. It can be easily derived the critical issue concerning to the fact that two unmatched channels will give rise to phase shift between voltages at the demodulator outputs [2.23], which involves incorrect values for real and imaginary impedance components. Digital quadrature demodulation (DQD) can be used for avoiding phase errors coming from mismatching in the AQD measurements by using look-up-tables for storing the in-phase and quadrature clocked signals. DQD implementation requires digital demodulators based on digital signal processing (DSP) [2.24], field-programmable gate arrays (FPGAs) [2.25], or application-specific integrated circuits (ASICs) [2.26, 2.27], which adds complexity to the whole measurement circuit realization, and often leads to high cost, high size and high power consumption [2.28]. Moreover, the increasing number of applications of electrical bioimpedance measurements in biomedical practice performing measurement at relatively high frequencies involves higher sample rates and, consequently, higher power consumption systems [2.29, 2.30]. Therefore, quadrature-demodulation techniques, both AQD and DQD, present some drawbacks when the design of wide-band, minimum-size, and portable, even wearable EBI measurement systems with reduced power consumption and size are required.

An indirect measurement technique for extracting complex electrical bioimpedance of local tissue has been proposed as a compact and cost-effective solution for real-time impedance measurement [2.31]. The principle of the indirect method (MRPDD, Magnitude-Ratio Phase-Difference Detection) is based on the determining the magnitude and the phase of the polar form of a complex magnitude through the

extraction of two independent voltages signals, V_Z and V_S, from the two voltage measuring electrodes and a reference resistor, respectively. The real part Z_{real} and imaginary part Z_{imag} of the complex impedance between two voltage electrodes can be acquired from the modular ratio, $|V_Z|/|V_S|$, and the phase difference, $\theta_Z - \theta_S$, of the two voltage signals through simple calculations. When compared with the quadrature-demodulator four-electrode method, the indirect method shows the advantage of simplicity in circuit realization and may alleviate the traditional electrical bioimpedance measuring system from an excessive complexity of electronics.

The structure of an electrical bioimpedance measurement device based on the indirect method is depicted in Fig. 2.9 [2.31]. In this figure, Z_X represents the (unknown) impedance of the material under test (MUT) and R_S is a reference resistor connected in series with Z_X. The basis of the device performance relies on measuring the amplitude and the phase of a complex parameter by comparing the magnitudes and the phases of two complex signals using a gain-phase detector (GPD). A reference current I_0 is injected through two electrodes (H_C, L_C) to stimulate the tissue of unknown impedance Z_X. At the same time, current I_0 also flows through a reference resistor R_S connected in series with Z_X. Two other electrodes (H_V, L_V) sense the voltage drop V_Z across Z_X, which is amplified by an instrumentation amplifier, IA_1. The voltage signal V_S across R_S is amplified by another instrumentation amplifier, IA_2. Provided that the input impedances of IA_1 and IA_2 are infinite, there will be no current flowing through the two voltage-sensing electrodes and, hence, the two output voltages of IA_1 and IA_2 can be expressed as

$$\begin{aligned} V_{AZ} &= A_1 \cdot V_Z = A_1 \cdot I_o \cdot Z_X \\ V_{AS} &= A_2 \cdot V_S = A_2 \cdot I_o \cdot R_S \end{aligned} \tag{2.7}$$

where A_1 and A_2 are the voltage gains of IA_1 and IA_2, respectively.

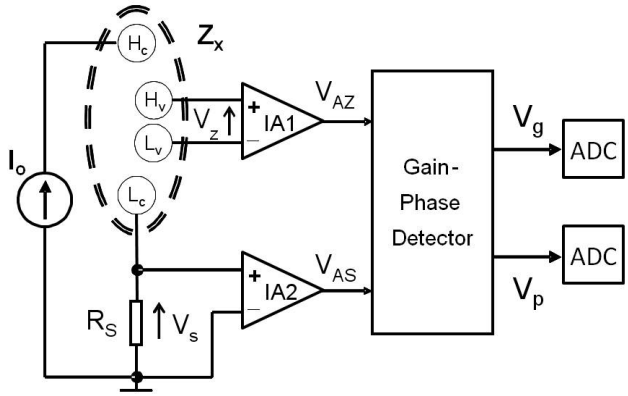

Figure 2.9. Block diagram of magnitude-ratio and phase-difference detection based on tetrapolar structure.

The two above voltage signals are processed by the GPD so as to obtain, after low-pass filtering, two DC voltages proportional to their magnitude ratio $|K|$ and phase difference θ, respectively:

$$\begin{aligned} |K| &= \frac{|V_{AZ}|}{|V_{AS}|} \\ \theta &= (\theta_{AZ} - \theta_{AS}) \end{aligned} \tag{2.8}$$

Taking into account that amplifiers IA_1 and IA_2 are implemented identically, it is straightforward to obtain that the unknown impedance Z_X can be expressed as

$$Z_X = R_S \cdot \frac{A_1}{A_2} \cdot \frac{V_{AZ}}{V_{AS}} = R_S \cdot \frac{A_1}{A_2} \cdot |K|_{\angle\theta} \tag{2.9}$$

Needless to say, if IA_1 and IA_2 are constructed identically, the gain ratio can be ideally assumed as $A_2/A_1 = 1$. Then, Eq. (2.9) is simplified and the measured impedance Z_X is obtained as

$$Z_X = R_S \cdot |K|_{\angle\theta} \tag{2.10}$$

It is worth to point out that R_S is a standard resistor with known value, and $|K|$ and θ are the outputs of the GPD, which can be sampled by ADCs for further processing.

The implementation of the indirect approach requires mainly two different kinds of circuits, namely an instrumentation amplifier and a gain-phase detector, together with low-pass filtering circuitry for extracting the DC voltages corresponding to the magnitude and the phase of impedance Z_X. This fact results in low circuital complexity. Both the above circuit blocks are suitable for monolithic implementation with reduced area and power consumption.

Table II.I summarizes the three basic electrical bioimpedance measurement techniques [2.32].

Table II.I. A comparison of EBI measuring techniques.

Measuring Method	***Advantages***	***Disadvantages***
Bridge method	High measurement resolution	Time consuming
Classical analog quadrature demodulation	_____	Large phase error. Need for avoiding any mismatch between in-phase (I) and quadrature (Q) references
Digital quadrature demodulation	No need for analog I and Q references	High cost. High power consumption
Magnitude-Ratio Phase-Difference Detection (MRPDD)	Cost-effective alternative for real time impedance measurement	_____

In addition, it is worth to point out the important influence of an accurate value for the injected current to obtain real and imaginary components (Z_{real} and Z_{imag}) with the AQD technique, which is not the case for the indirect MRPDD method due to the fact that the magnitude and phase values of the unknown impedance are obtained by comparing voltage signals related to the same injected current I_0 which, therefore, does not need to be accurately known. This fact reaches an special relevance for high-frequency bioimpedance spectroscopy where a reduction in the output resistance of the excitation current source always occurs.

2.2.3. Monolithic implementations of EBI sensors

During the last years, different approaches have reported to provide a monolithic solution for low-cost, low-power, high-performance bioimpedance measurement systems. This section provides a brief review of the monolithic solutions presented for a bioimpedance integrated circuit that can be found in literature.

To the best of our knowledge, the first integrated circuit (IC) for the measurement of tissue impedances was presented in 2005 by Yúfera *et al*. [2.22]. In particular, the proposed circuit is intended for sensing myocardium tissue impedance as a biomedical parameter in living bodies that allows ischemia detection. The designed chip is the core of a four-electrode based measurement system, two injecting electrodes and two sensing electrodes, and includes a circuit to generate the stimulus signals (sinusoidal current). Circuit operation is based on the two-phase referent coherent demodulation method mentioned above. The sensed voltage response is processed to simultaneously obtain the real and the imaginary component of the unknown complex impedance, Z_x. For that purpose, two demodulators with the corresponding clock phases, Φ and Φ_{quad}, in quadrature of phase are required to provide two digital signals corresponding to the digital representation of the real and the imaginary part, respectively, of the tissue impedance Z_x.

The whole system fulfills the following general specifications. The excitation current is set to 5 μA_{rms}, with a frequency in the range from 1 kHz to 20 kHz. The expected range of magnitude to be measured goes from 100 Ω to 10 kΩ, whereas the expected phase counterpart is in the range [0°, 30°]. The above phase range covers the usual values up to 10º. Nevertheless, it is worth to point out that the frequency range does not allow the use in the whole β-dispersion region. At the same time, applications with magnitude impedance values below 100 Ω are out of the allowed range of this system.

A compact system for impedance measurement in the kHz-MHz frequency range has been reported by Rottigni *et* al. [2.33]. The designed system addresses micro- and nano-scale bio-sensing applications, such as impedimetric flow, cytometry or molecular affinity bio-sensors. In this measurement system, a sinusoidal voltage is generated and applied to the sample under test, while the current flowing through the sample is read by using a low noise amplifier, whose output signal is demodulated by means of two multipliers with 90° and 0° phase shift with respect to the excitation signal. The output of the multipliers is then converted to a digital signal and low-pass filtered to obtain the real and imaginary part of the admittance of the sample under test. The excitation signal is supplied by a direct digital synthesizer implemented in an FPGA together with auxiliary circuitry such as digital-to-analog converter, output buffer, and level shifter included for excitation amplitude control. The overall system structure involves a power-hungry system not suitable for wearable solutions.

Triantis *et al*. [2.34] presented a bioimpedance sensor ASIC for the measurement of tissue impedances as a part of a wearable electrical impedance tomography-based imaging system. The ASIC was fabricated in 0.6-μm CMOS technology and is able to measure the real and the imaginary part of tissue impedances for wideband *multifrequency* electrical impedance tomography applications. It includes circuitry for both current injection and impedance measurement. The basis of the impedance

measurement part lays on the multiplication of the signal picked up by the recording electrodes by a square-wave signal with the same frequency. The real and the imaginary part of the tissue impedance can be extracted by setting the phase of the square wave signal to 0° and 90º, respectively. The ASIC occupies a core area of 4.5 mm^2 and dissipates about 10 mW from a ±2.5 V power supply. Its bandwidth covers the range from 10 kHz to about 1 MHz. Measurement accuracy is better than 1 Ω. A second version of this chip design, now fabricated in a 0.35-µm CMOS process, was presented in [2.35].

A 0.35-µm CMOS magnitude/phase measuring circuit is presented for spectroscopy and tomography EBI applications in [2.36]. The maximum operating frequency is 100 kHz, whereas the total supply voltage (±2.5 V) as well as the power consumption 21 mW makes the circuit implementation not very suitable for wearable EBI applications. In addition, most of the used microelectronic design techniques are very sensitive to the unavoidable tolerances of process fabrications. This fact limits strongly the design for practical applications further the R&D lab domain.

A wireless bio-impedance monitor for wearable applications is described in [2.37]. The system is made of two staked modules, where one of them includes a bioimpedance ASIC sensor (analog front end). The authors do not provide too much details about the sensor implementation and operation. Nonetheless, the circuit operates in a very narrow operating measuring range ($R < 50\ \Omega$) and needs to be on-board calibrated before every measurement.

Other proposed IC realizations for bioimpedance measurements that have been reported [2.38] carry out the signal processing in the digital domain. Indeed, this way simplifies the design process since the always complex analog signal processing part is replaced by high-resolution ADC and a programmable digital signal processor. The price paid consists in high power consumption and area and as consequence, the

resulting system is not very appropriate for wearable bioimpedance monitoring applications.

Bioimpedance measurement sections have also designed for multi-sensor biomedical ICs. In [2.39] a high-performance, low-power AFE system-on-chip is described. The AFE provides three ECG readout channels, one bioimpedance channel, as well as general purpose analog readout channel. The bioimpedance channel is designed for a specific parameter monitoring (hydration) and its processing is based on the AQD method.

A second group of monolithic EBI measuring circuits is made of those realizations addressed to implantable monitoring devices. For instance, depending on the configuration used, impedance sensors provides information about lung congestion and edema –typical of blood congestion in the pulmonary system due to a deteriorated pumping function of the left ventricle [2.40]–, directly assessing the hemodynamic of the heart –intracardiac impedance [2.41, 2.42]– or other intended applications implantable impedance plethysmography acting directly over large arteries to monitor cardiovascular parameters such as blood pressure and long term arteriosclerotic progression [2.43]. From the point of view of the integrated circuit design a common characteristic to all implantable bioimpedance sensor consists in the simplicity, since they have to perform measurements over a very restricted range of magnitude or phase angle –typical measuring magnitude ranges go from 40 Ω to 90 Ω with 0.25 Ω of resolution [2.42]–. Indeed, power consumption constraints reaches a paramount importance in this kind of EBI sensor applications [2.44].

An alternative approach for implantable sensors that tries to avoid these stringent limitations consists in providing electrical power through an inductive coupling with an external transmitter also valid for communication [2.45, 2.46]. However, this kind of implantable devices are superficial implants (skin implants) and the reading of physiological variables is carried out when the external reader provides wireless power.

In other words, the use of bateryless sensors is limited for continuous, or even periodic, physiological monitoring applications.

Together with the scientific and academic work, it is worthy to point out the interest that monolithic solutions for bioimpedance measurements have raised in the market. In this sense, semiconductor companies of great importance, such as Texas Instruments and Analog Devices, have invested significant effort in the development of integrated circuits for processing bioimpedance data.

One of the most widely used system-on-chip electrical bioimpedance analyzer/spectrometer that can be found in the market is the AD5933 circuit from Analog Devices [2.47]. In particular, the system has not been specifically designed for electrical bioimpedance measurement purposes, and original requirements related to loudspeakers characterization are satisfied more efficiently than the EBI measurements counterparts. AD5933 alone is not suitable for EBI measurements on patients or for several EBI applications due to several limiting factors. One of these limiting factors corresponds to a safety issue due to the imbalance of DC voltage level at the voltage output of the circuit. The AD5933 circuit is a voltage-driven system without control over the injected current, which involves a safety hazard since the injected current can be larger than the limits set by IEC-60601, which is equal to 1 mA_{rms} [2.48].

A significant point to note is that the AD5933 circuit is a two-electrode impedance measurement device. This fact limits the use of the circuit by itself since the obtained impedance measurement will also contain the electrode-skin impedance contribution. In this sense, an additional AFE [2.49] was proposed to adapt the AD5933 circuit to a four-electrode strategy, thus allowing its use in biomedical applications. At the same time, an adaptation circuit for measurements of small impedance was used. Measurements were carried out in the frequency from 5 kHz to 100 kHz. The magnitude value of the working load was adapted to fall in the range from 50 Ω to 1.6 kΩ. In addition, it is worthy to point out that the use of the AD5933 integrated circuit

requires a calibration process previous to the measurement for the system to be adapted according the load to be measured.

Texas Instruments has launched a specific application circuit, AFE4300 [2.50]. The system is designed for incorporation into scales which, in addition to weight assessment, derives body composition for an individual from regression equations based on anthropometric data –weight, height, gender–, thus resulting in overall bioimpedance analysis. For this reason, the circuit is a low-cost front-end incorporating two channels: one channel is devoted to measure the weight of a person, and the second to assess body composition. AFE4300 operation for EBI analysis is based on the principle of quadrature demodulation and requires up to four external impedances for calibration. It includes a five-input multiplexer to perform segmental analysis (impedance analysis separately for arms, legs, and trunk). If it is intended for use beyond the application for which the product was designed, i.e., analysis of body composition, it should be taken into consideration that AFE4300 limits its operation to a single frequency, so that it is not possible to perform spectrometry bioimpedance, or even just bioimpedance analysis with another excitation current.

Recently, Analog Devices has just announced the released version of its ADCuM350 integrated circuit for 2015 [2.51]. It is a 120-pins circuit with several different functionalities and subsystems, where one of them is dedicated to impedimetric measurements. In particular, electrical impedance circuit operation is based on the two-phase referent coherent demodulation method and the use of Discrete Fourier Transform hardware for obtaining the magnitude and phase values of the impedance under test, which involves a high level of complexity and also processing power consumption. Finally, it should be pointed out that the frequency range where impedance values can be measured with Analog Devices ADCuM350 circuit is upper limited up to ~75kHz.

2.2.4. Multichannel bioimpedance measurements

As stated, electrical bioimpedance represents an useful technology for relating the electrical properties of a living organism with its composition or for monitoring a physiological event or functionality. In certain cases, the information provided by a single EBI measurement may not be enough to overcome complex physiological problems, and simultaneous multisite bioimpedance measurements at different body locations are necessary –multichannel EBI measurements–.

Several EBI segments are very prone to incorporate multichannel bioimpedance measurements. Thus, and for citing a few, time-domain EBI measurements at different sites of the arterial tree provide valuable information about cardiovascular system –cardiac output, arterial stiffness, peripheral blood flow, etc.– or with other physiological parameters such as respiratory function [2.52, 2.53]. EBI spectroscopy analysis performed at symmetrical anatomical regions such limbs, allows efficiently detection of extracellular fluid accumulation –limphoedema– and much earlier than any other technique [2.54, 2.55]. Electrical Impedance Tomography is a technique for generating low-cost medical images from the bioimpedance responses obtained at different locations and processed with a reconstruction software [2.56, 2.57].

Multichannel bioimpedance measurements aim at giving an adequate response to the challenge of EBI measurements at different locations of the same biological material. Theoretically, several approaches exist for connecting EBI measuring systems to the same organism and avoid corrupted results due to the overlapping of the corresponding excitation signals.

From a general point of view, if more than one excitation current signal are simultaneously injected into the same biological material, the voltage response corresponds to the sum of the individual voltage responses that each single excitation signal would produce on its own [2.58], i.e., the biological material can be regarded as

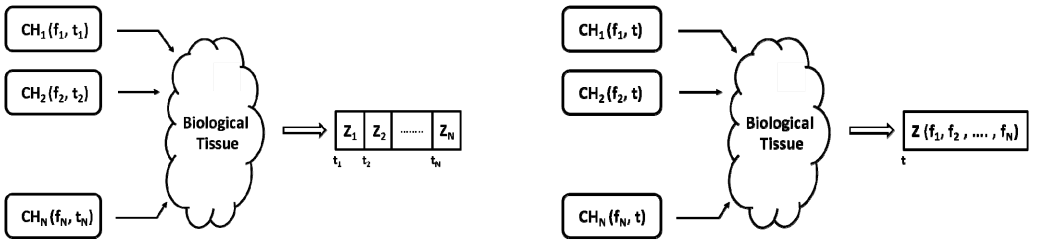

(a) (b)

Figure 2.10. a) Time division multiplexing (TDM) and b) Frequency division multiplexing (FDM) concepts.

a linear system in this respect. The separation of the individual responses can be carried out if certain signal processing techniques for EBI are used, however, they require a great computation task.

In any case, for avoiding overlapping in the individual voltage response signals the following strategies can be incorporated:

- Time division multiplexing (TDM): It utilizes fast switching between multiple EBI channels. Although, strictly speaking, the resulting system does not carry out the measurement simultaneously, the excitation signals do not overlap [2.59] as it is illustrated in Fig. 2.10 (a);
- Frequency division multiplexing (FDM): If non-overlapping frequency signals, Fig. 2.10 (b), are injected, their responses can be separated again through frequency separation techniques [2.60];
- Synchronous sampling: It has been shown that frequency separation methods utilized in FDM require high computational resources [2.61]. Some researchers have proposed schemes of synchronous sampling to simplify signal-processing FDM calculations [2.62].

In this sense, conventional multichannel bioimpedance solutions, which utilize multiple single-lead EBI measurement systems connected to the same organism, involve difficulty and complexity for constructing high-fidelity multi-channel, multi-frequency data acquisition instruments. Therefore, solutions that facilitate the measurement of separated bioimpedances in a human body with maximum accuracy comprise a field of great interest and importance for the widespread development of multiple spectroscopic electrical impedance measurements in different locations.

2.3. EBI MEDICAL APPLICATIONS: PITFALLS AND NEW PERSPECTIVES

Although EBI technology can be applied in many fields, the segment of medical devices is one of its major working areas. In addition, within the segment of medical applications, the flexibility of the EBI method can be used for the evaluation of assorted physiological variables and detect a wide variety physiological events. In particular, EBI medical applications are encompassed in the following three main categories [2.63]: *Impedance Spectroscopy*, *Impedance Plethysmography* and *Impedance Imaging*.

Impedance Spectroscopy, also called Bioimpedance Spectroscopy (BIS), which consists in the study of the impedance for tissue characterization and functional monitoring in a determined frequency range of the excitation current signal, which is typically from 1 kHz to a few MHz. A particular case is the single-frequency bioimpedance analysis (SF-BIA), where a unique input frequency is used (usually 50 kHz). At this frequency, the internal current flows through the extracellular space as well as through the intracellular space, which provides valuable information about the health/integrity of cell walls. Practical applications of BIS and SF-BIA are body composition analysis, early detection of alterations in organs and tissues, and assessment of the effectiveness of therapies and treatments.

Global body composition analysis [2.64, 2.65] is based on exciting the whole body with an electrical current –e.g. foot-to-foot, foot-to-hand, segmental analysis– and applying sophisticated regression equations along with anthropometric data to the measured impedance results to determine total body water, extra- and intra-cellular water contents, fat-mass contents, etc.

The other two BIS application areas –i.e., detection of alterations or monitoring of organs and tissues and assessment of the effectiveness of therapies and treatments– are

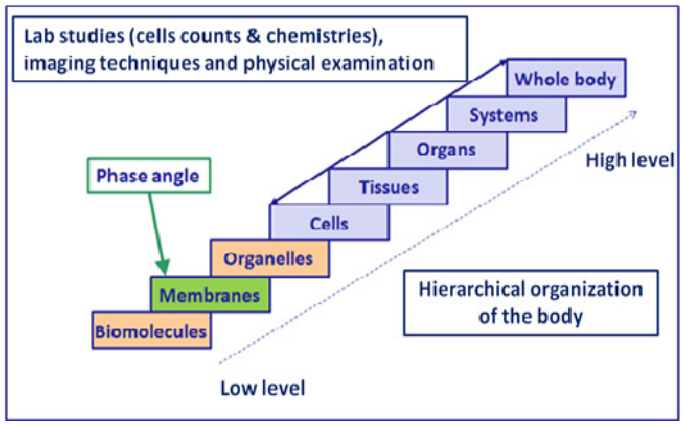

Figure 2.11. Clinical studies and hierarchical organization of the body.
Redrawn from http://vitalityanalyzer.com.

based on the same approach: compare the measured EBI parameters with reference EBI values that serve as a basis from evaluations in clinical settings. These reference values can be absolute values derived from serial studies [2.66-2.68] or differential values obtained from consecutive trials taken at different times [2.69], which allow one to observe the change of the corresponding EBI parameters over time. An important aspect is this second approach (differential assessment) consists in guaranteeing the same (predetermined) positions of the assessment points in the body surface [2.70].

In principle, any EBI parameter can be used as monitoring/assessing variable, however, phase angle is the one that better illustrates the presence and progression of a disease, as well as the effectiveness of a pharmacologic or non-pharmacologic treatment intervention. As stated above, phase angle is proportional to the health of the cell and the plasma cell membrane and, therefore, its value clearly reports information about changes at cellular level, which reliable illustrate variations before they can be determined through typical diagnosis methods such as blood chemistries/cell counts, physical signs, or imaging techniques. In other words, as illustrated in Fig. 2.11, phase angle provides a level of understanding that occurs prior to techniques

currently utilized and in that sense can be considered a prognosis indicator. Phase angle can be used as a global indicator and excellent predictor of a whole-body disease condition [2.71] or as local parameter indicative of the health in a well-localized body area.

Impedance Plethysmography consists in recording the instantaneous volume of an object by measuring electrical impedance [2.72]. In practice, the term of impedance plethysmography is mostly associated to the assessment of blood volume changes in any part of the body from changes caused in the electrical impedance of such body segment. Thus, typical applications of this method can be found in monitoring the stroke volume of the heart –usually called impedance cardiography or thoracic electrical bioimpedance–, assessing peripheral blood flow and arterial stiffness [2.73], respiration monitoring [2.74], and so on.

Thoracic bioimpedance is currently the most widely used truly non-invasive method for cardiac output monitoring yielding interesting results in controlled settings [2.75]. However, in complex cardiac patients, as typically found in intensive care units and post-operative settings, the accuracy of this approach is limited. This is in part due to the inherently low signal-to-noise ratio of this approach.

Traditional impedance plethysmography systems measure the magnitude of the bioimpedance as a magnitude that varies proportionally to the amount of body fluid in the thorax for the case of cardiac output monitoring. However, it has been recently shown that changes in the blood volume of a body segment also produces changes in the imaginary part (bioreactance or capacitive component) of the bioimpedance [2.17]. This change in bioreactance or in the phase of the signal response can be detected as a change in the frequency of this signal. As usual, techniques for accurately measuring modulation of frequencies are inherently more accurate and robust –i.e., they provide better signal-to-noise ratio– than techniques that measure changes in signal amplitude. This is the basic principle of bioreactance technology, which shows

the same difference from traditional EBI technology as FM from AM techniques in radio systems. In addition, as stated above, other advantage of bioreactance method compared with thoracic bioimpedance consists in the independence of phase shift with the relative placement on the body of the sensing electrodes [2.76].

Impedance Imaging, which is based on multiple impedance measurements by injecting current and recording the voltage with a multiple electrode system located in a cross-section of the body [2.77]. A reconstruction algorithm applied to the collected data generates an image that provides information about conductivity inside the body. Depending on the collected data (transimpedance, resistance, or capacitance), the corresponding technique is referred to as electrical impedance tomography (EIT), electrical resistance tomography, or electrical capacitance tomography, respectively. In any case, although the spatial resolution of these techniques is poor when compared to other imaging techniques, the time of resolution (in the order of microseconds) is unique for EIT. Affordability and non-invasive performance are other exclusive features of EIT.

Nonetheless, in spite of the attractive features of EBI technology mentioned above, it suffers from others non less important drawbacks, such as the measurement results are influenced by factors such as motion, there is absence of standardized procedures, etc [2.63]. However, the main drawback of this technology arises from the fact that bioimpedance is not a physiological variable and it suffers from the limitations inherent to many indirect techniques [2.78]. Therefore, bioimpedance measurements must be translated –calibrating– in true physiological terms for which complex empirical prediction model have been created that frequently produce inconsistent results.

The combination of raw bioimpedance measurements with the avoidance of mathematical prediction equations overcome the above limitations in certain EBI applications [2.79]. In addition, for the rest of applications the availability of efficient

bioimpedance measurement devices for personal and ambulatory uses, allow the monitoring of the corresponding physiological variables. Indeed, the happened progresses in microelectronic and telecommunication technologies have prompted this new and interesting perspective for EBI technology. In this context the research presented in this work fits.

2.5. REFERENCES

[2.1] S. Grimnes and Ø. G. Martinsen, *Bioimpedance and Bioelectricity Basics* (2nd edition), Academic Press, 2008.

[2.2] A. Stahn, E. Terblanche, and H.–C. Gunga, "Use of bioelectrical impedance: general principles and overview," *Handbook of Anthropometry*, Ch. 3, pp. 49-90, Springer-Verlag, 2012.

[2.3] D. Miklavcic, N. Pavšelj, and F. X. Hart, "Electric properties of tissues," *Wiley Encyclopedia of Biomedical Engineering*, vol. 6, pp. 3578-3589, John Wiley & Sons, 2006.

[2.4] J. G. Webster, *Medical Instrumentation. Application and Design* (Fourth edition), John Wiley & Sons, 2010.

[2.5] E. T. McAdams, *A Study of Electrode-Tissue Impedance Encountered in Cardiac Pacing*, Ph. D. Thesis, University of Leeds, UK, 1987.

[2.6] P. Bertemes-Filho, *Tissue Characterization using an Impedance Spectroscopy Probe*, Ph. D. Thesis, University of Sheffield, U.K., 2002.

[2.7] P. Aberg, "Method and apparatus for diagnosing a diseased condition in tissue of a subject," U.S. Patent 2010/0191141, Jul. 2010.

[2.8] F. Goldkuhl *et al*., "Switch probe for multiple electrode measurement of impedance," U.S. Patent 2011/0282180, Nov. 2011.

[2.9] E. Bouty, "Sur la conductibilité electrique de dissolutions salines très étendues," *Journal de Physique Théorique et Appliquée*, vol. 3, pp. 325-355, Aug. 1884.

[2.10] A. O. Ragheb, L. A. Geddes, J. D. Bourland, and W. A. Tacker, "Tetrapolar electrode system for measuring physiological events by impedance," *Medical & Biological Engineering & Computing*, vol. 30, pp. 115-117, Jan. 1992.

[2.11] H. P. Schwan, "Determination of biological Impedances," *Physical Techniques in Biological Research*, Academic Press, 1963, 323.

[2.12] R. Patterson, "Bioelectric Impedance Measurements," *The Biomedical Engineering Handbook*: (Second Edition), CRC Press LLC, 2000.

[2.13] E. Atzler and G. Lehmann, "Über ein neues Verfahren zur Darstellung der Herztätigkeit (Dielektrographie)," *European Journal of Applied Physiology*, vol. 5, pp. 636-680, May 1932.

[2.14] J. Nyboer, *Electrical Impedance Plethysmography* (Second Edition), U.S.A., Charles C. Thomas, 1970.

[2.15] J. Nyboer and J. G. Kornmesser, "Electrical impedance of the abdomen during maternal labor," *Annals of the New York Academy of Science*, vol. 170, pp. 801-803, July 1970.

[2.16] J. Nyboer, "Workable volume and flow concepts of biosegments by electrical impedance plethysmography," *Tower International Technomedical – Journal of Life Sciences*, vol. 2, pp. 1-13, Jan. 1972.

[2.17] P. Squara, "Bioreactance: A New Method for Non-invasive Cardiac Output Monitoring" in *Intensive Care Medicine* (J. L. Vincent, Ed.), pp. 619-630, Springer-Verlag, 2008.

[2.18] D. G. Jakovljevic, M. I. Trenell, and G. A. MacGowan, "Bioimpedance and bioreactance methods for monitoring cardiac output," *Best Practice & Research Clinical Anaesthesiology*, vol. 28, pp. 381-394, 2014.

[2.19] C. D. Ferris, *Introduction to Bioelectrodes*, Plenum Press, 1974.

[2.20] R. Pallàs-Areny and J. G. Webster, *Analog Signal Processing*, John Wiley & Sons, 1999.

[2.21] J. Songer, "Tissue ischemia monitoring using impedance spectroscopy; Clinical evaluation," in *Biomedical Engineering*, vol. Master´s degree, Worcester Polytechnic Institute, 2001.

[2.22] A. Yufera *et al.*, "A tissue impedance measurement chip for myocardial ischemia detection," *IEEE Transactions on Circuits and Systems–I, Regular Papers*, vol. 52, pp. 2620-2628, Dec. 2005.

[2.23] R. Pallàs-Areny and J. G. Webster, "Bioelectric impedance measurements using synchronous sampling," *IEEE Transactions on Biomedical Engineering,* vol. 40, pp. 824–829, Aug. 1993.

[2.24] R. D. Cook *et al.*, "ACT3: A high-speed, high-precision electrical impedance tomograph," *IEEE Transactions on Biomedical Engineering*, vol. 41, pp. 713-722, Aug. 1994.

[2.25] N. Liu, G. J. Saulnier, and J. C. Newell, "A multichannel synthesizer and voltmeter for electrical impedance tomography," *Proceedings of the 25th Annual International Conference of the IEEE Engineering in Medicine and Biology Society,* pp. 3110-3111, Sept. 2003.

[2.26] J. Balendonck and M. A. Hilhorst, "Application of an intelligent dielectric sensor for soil water content, electrical conductivity and temperature," *Proceedings of the 18th IEEE Instrumentation and Measurement Technology Conference*, vol. 3, pp. 1817-1822, May 2001.

[2.27] M. Min, O. Märtens, and T. Parve, "Lock-in measurement of bio-impedance variations," *Measurement*, vol. 27, pp. 21-28, Jan. 2000.

[2.28] R. Casanella, O. Casas, and R. Pallàs-Areny, "Differential synchronous demodulator for modulating sensors and impedance measurements," *Measurement Science and Technology*, vol. 16, pp. 1637-1643, Aug. 2005.

[2.29] P. Aberg, *Skin Cancer as seen by Electrical Impedance*, Ph. D. Thesis, Karolinska Institutet, Stockholm, Sweden, 2004.

[2.30] L. Beckman, D. van Riesen, and S. Leonhardt, "Optimal electrodes placement and frequency range selection of lung water using bioimpedance spectroscopy," *Proceedings of the 29th Annual International Conference of the IEEE Engineering in Medicine and Biology Society*, pp. 2685-2688, Aug. 2007.

[2.31] Y. Yang, J. Wang, G. Yu, F. Niu, and P. He, "Design and preliminary evaluation of a portable device for the measurement of bioimpedance spectroscopy," *Physiological Measurement*, vol. 29, pp. 1293-1310, Dec. 2006.

[2.32] D. Bouchaala, A. Fendri, and O. Kanoun, "Handheld bioimpedance spectrometer for the total frequency range of β–dispersion," *Proceedings SENSOR*, pp. 175-180, 2013.

[2.33] A. Rottigni, M. Carminati, G. Ferrari, and M. Sampiestro, "Handheld bio-impedance measurement system based on an instrument-on-chip," *7th Conference on Ph.D. Research in Microelectronics and Electronics (PRIME)*, pp. 49-52, July 2011.

[2.34] I. F. Triantis *et al*., "A multi-frequency bioimpedance measurements ASIC for electrical impedance tomography," *Proceedings of the European Solid-State Circuits Conference (ESSCIRC)*, pp. 331-334, Sept. 2011.

[2.35] P. Kassanos et al., "An integrated analog redout for multi-frequency bioimpedance measurements," *IEEE Sensors Journal*, vol. 14, pp. 2792-2800, 2014.

[2.36] P. Kassanos, I. F. Triantis, and A. Demosthenous, "A CMOS magnitude/phase measurement chip for impedance spectroscopy," *IEEE Sensor Journal*, vol. 13, pp. 2229-2236, 2013.

[2.37] S. Lee *et al*., "A low-power and compact-sized wearable bio-impedance monitor with wireless connectivity," *Journal of Physics: Conference Series (XV Int. Conf. on Electrical Bio-Impedance, ICEBI),* vol. 434, pp. 12013-12016, 2013.

[2.38] M.–C. Cho, Y.–G. Yoon, and S. Cho, "Design of highly programmable bio-impedance measurement IC in 0.18 μm CMOS", *International System-on-Chip (SoC) Conference*, pp. 79-82, 2009.

[2.39] N. Van Helleputte et al., "A 345 μW multi-sensor biomedical SoC with bio-impedance, 3-channel ECG, motion artifact reduction, and integrated DSP", *IEEE Journal of Solid-State Circuits*, vol. 50, pp. 230-244, 2015.

[2.40] J. Kirchner et al., "Heart failure monitoring with implantable defibrillators," *Biomed. Tech*., vol. 57, pp. 1079-1082, 2012.

[2.41] M. R. Cowie, "Monitoring heart failure using an implantable device measuring intrathoracic impedance – Technical and clinical overview," *Business Briefing: European Cardiology*, pp. 1-4, 2005.

[2.42] L. Wang, "Fundamentals of intrathoracic impedance monitoring in heart failure," *The American Journal of Cardiology*, vol. 99, pp. 3G-10G, 2007.

[2.43] M. Theodor *et al*., "Implantable impedance plethysmography," *Sensors*, vol. 14, pp. 14858-14872, 2014.

[2.44] W. H. Ko, "Early history and challenges for implantable electronics," *ACM Journal on Emerging Technologies in Computing Systems*, vol. 8, p. 8:1-8:9, 2012.

[2.45] J. Colomer-Ferrarons, P. Miribel-Catalá, I. Rodríguez and J. Samitier, "CMOS front-end architecture for in-vivo biomedical implantable devices," *35th Annual Conference of the IEEE Industrial Electronics*, pp. 4401-4408, 2009.

[2.46] S. Rodriguez, S. Ollmar, M. Waqar, and A. Rusu, "A batteryless sensor ASIC for implantable bio-impedance applications," *IEEE Transactions on Biomedical Circuits and Systems*, (accepted for publication), 2015.

[2.47] AD5933 Analog Devices Application Note: http://www.analog.com/en/AD5933/productsearch.html

[2.48] IEC 60601-1-2, Medical electrical equipment – Part 1-2: General requirements for safety –Collateral standard: Electromagnetic compatibility – Requirements and tests.

[2.49] F. Seoane, J. Ferreira, J. J. Sánchez, and R. Bragós, "An analog front-end enables electrical impedance spectroscopy system on-chip for biomedical applications", *Physiological Measurement*, vol. 29, pp. S267-S278, June 2008.

[2.50] AFE4300 Texas Instruments: http://www.ti.com/lit/ds/symlink/afe4300.pdf

[2.51] ADuCM350 Analog Devices Datasheet: http://www.analog.com/media/en/technical-documentation/data-sheets/ADuCM350.pdf

[2.52] J. Lamp, "Multi-channel impedance cardiography and method of multi-channel impedance cardiography," US Patent 2011/0301492, Dec. 8, 2011.

[2.53] G. D. Jindal *et al*., "Early detection of coronary heart disease using peripheral pulse analyzer," *BARC Newsletter*, Issue no. 326, pp. 15-21, May-June 2012.

[2.54] L. Ward and B. H. Cornish, "Method and device for measuring tissue oedema," US Patent 8,233,974, Jul. 31, 2012.

[2.55] M. Takeuchi *et al*., "Detecting subclinical secondary lymphoedema using bioimpedance: a preliminary study," *Journal of Lymphoedema*, vol. 8, pp. 16-20, 2013.

[2.56] R. Bayford and A. Tizzard, "Bioimpedance imaging: an overview of potential clinical applications," *Analyst,* vol. 137, pp. 4635-4643, 2012.

[2.57] J. C. Baeg *et al*., "An amplitude-to-time conversion technique suitable for multichannel data acquisition and bioimpedance imaging," *IEEE Transactions on Biomedical Circuits and Systems*, vol 7, pp. 349-354, 2013.

[2.58] Y. Yamamoto, T. Nakamura, T. Kusuhara, and Adli, "Considerations of conditions required for multi-channel simultaneous bioimpedance measurement," *Proceedings of the IEEE Instrumentation and Measurement Technology Conference*, pp. 231-234, 1998.

[2.59] S. Pyo, K. J. Loh, T.–C. Hou, E. Jarva, and J. P. Lynch, "A wireless impedance analyzer for automated tomographic mapping of a nanoengineering sensing skin," *Smart Structures and Systems*, vol. 8, pp. 139-155, July 2011.

[2.60] J. Gracia, V.–P. Seppä, J. Viik, and J. Hyttinen, "Multilead measurement system for the time-domain analysis of bioimpedance magnitude," *IEEE Transactions on Biomedical Engineering*, vol. 59, pp. 2273-2280, Aug. 2012.

[2.61] P. Annus, *Multichannel Bioimpedance Spectroscopy: Instrumentation Methods and Design Principles*, Ph. D. Thesis, Tallin University of Technology, Estonia, 2009.

[2.62] M. Min, T. Parve, A. Ronk, P. Annus, and T. Paavle, "Synchronous Sampling and Demodulation in an Instrument for Multifrequency Bioimpedance Measurement," *IEEE Transactions on instrumentation and Measurement*, vol. 56, pp. 1365- 1372, April 2007.

[2.63] J. Jossinet, "Bioimpedance and p-Health" in *Personalized Health Management Systems: The Integration of Innovative Sensing, Textile, Information and Communications Technologies* (C. D. Nugent *et al*., Eds.), pp. 35-42, IOS Press, 2005.

[2.64] U. G. Kyle *et al*., "Bioelectrical impedance analysis–part I: review of principles and methods," *Clinical Nutrition*, vol. 23, pp. 1226-1243, Dec. 2004.

[2.65] U. G. Kyle *et al*., "Bioelectrical impedance analysis–part II: utilization in clinical practice," *Clinical Nutrition*, vol. 23, pp. 1430-1453, Dec. 2004.

[2.66] M. C. Barbosa-Silva *et al*., "Bioelectrical impedance analysis: population reference values for phase angle by age and sex," *The American Journal of Clinical Nutrition*, vol. 82, pp. 49-52, July 2005.

[2.67] A. V. B. Margutti, J. P. Monteiro, and J. S. Camelo, "Reference distribution of the bioelectrical impedance vector in healthy term newborns," *British Journal of Nutrition*, vol. 104, pp. 1508-1513, Nov. 2010.

[2.68] S. B. Rutkove, P. M. Forgerson, L. P. Garmirian, and A. W. Tarulli, "Reference values for 50-kHz electrical impedance myography," *Muscle & Nerve*, vol. 38, pp. 1128-1132, Sept. 2008.

[2.69] S. C. Eror *et al.*, "Method for diagnosing disease," U.S. Patent 2010/0094160, Apr. 2010.

[2.70] R. L. Gaw, "Impedance measurement process," U.S. Patent 2011/0313311, Dec. 2011.

[2.71] H. C. Lukaski and M. G. Singer, "Phase angle as a prognostic indicator in cancer," *Computational Physiology* (*Association for the Advancement of Artificial Intelligence, Spring Symposium)*, pp. 37-39, 2011.

[2.72] J. Malmivuo and R. Plonsey, "Impedance Plethysmography" in *Bioelectromagnetism – Principles and Applications of Bioelectric and Biomagnetic Fields*, Ch. 25, pp. 405-419, Oxford University Press, 1995.

[2.73] M. –C. Cho *et al*., "A bio-impedance measurement system for portable monitoring of heart rate and pulse wave velocity using small body area," *Proceedings of the IEEE International Symposium on Circuits and Systems (ISCAS)*, pp. 3106-3109, 2009.

[2.74] S. Lee *et al*., "A low power and convenient bio-impedance monitor and its application to respiration monitoring," *Proceedings of the 4th Conference on Wireless Health*, Article No. 13, 2013.

[2.75] G. Cybulski, "Impedance Cardiography" in *Ambulatory Impedance Cardiography: The Systems and Their Applications*, Springer-Verlag, 2011.

[2.76] D. G. Jakovljevic et al. "Bioimpedance and bioreactance methods for monitoring cardiac output," *Best Practice & Research Clinical Anaesthesiology*, vol. 28, pp. 381-394, 2014.

[2.77] R. H. Bayford, "Bioimpedance tomography (Electrical impedance tomography)," *Annual Review of Biomedical Engineering*, vol. 8, pp. 63-91, Aug. 2006.

[2.78] D. –W. Kim, "Detection of physiological events by impedance," *Yonsei Medical Journal*, vol. 30, pp. 1-11, 1989.

[2.79] H. C. Lukaski, "Evolution of bioimpedance: a circuitous journey from estimation of physiological function to assessment of body composition and a return to clinical research," *European Journal of Clinical Nutrition*, vol. 67, pp. S2-S9, 2013.

Chapter 3

A PLATFORM FOR EBI BIOMEDICAL APPLICATIONS

General requirements of a high-performance multisite EBI measuring system for the development of biomedical applications, are pointed out in this Chapter. It is also shown how the optimal realization leads to a solution inspired in the operation principle of body sensor networks. Architecture and functionality of the multichannel system adopted, as well as the block diagram and operation of the wireless basic node of the network, are also described in this Chapter.

3.1. CONSIDERATIONS AND REQUIREMENTS OF A HIGH-PERFORMANCE MULTISITE EBI MEASUREMENTS

Usually, current applications of bioimpedance measurement are limited to being recorded in a single place of the body. The possibility of having available simultaneous bioimpedance measurements over the whole body provides the opportunity of having more information of physiological events, as well as studying the relationship among them. However, in order to develop a high-performance multichannel device for multisite EBI measurements, the approach must differ from the classical ones which were concisely described in section 2.2.4.

The final target towards of the multichannel bioimpedance system approach should be to measure the bioimpedance in several points simultaneously and in an independent way. In addition, a high-performance multichannel bioimpedance system should be addressed to cover a wide set of applications, even some of them still unknown.

Taking into account the above considerations, three characteristics arise as fundamental ones for development of a multichannel bioimpedance system with high measuring capabilities. They are:

- flexibility: Each channel must perform as bioimpedance analyzer or spectrometer and the functional parameters independently defined;
- scalability: The number of channel must be completely open to the requirements of the application on the contrary to the multichannel traditional approaches where the number of channels is fixed in the design phase and for practical reasons the number of channel is limited to a few;
- simultaneity: All the channels should operate at the same time or according any timing sequence defined by the user. The only limit should be imposed by the maximum allowable current limit in the body (i.e. 1 mA or a few mA).

Needless to say that in order to satisfy the above requirements a completely different approach from the classical multichannel operations must be followed. The practical realization of the above requirements with a new high-performance multichannel bioimpedance measurement approach is dealt in the next sections of the Chapter.

3.2. A NOVEL APPROACH FOR MULTICHANNEL EBI MONITORING

3.2.1. Body sensor networks (BSN)

Sensor networks have been heralded as one of the most important technologies for the 21st century [3.1], and, in particular, have drawn a lot of attention from the research community and the industry during the last decade for wearable health-monitoring systems [3.2]. Most researchers agree on the fact that a sensor network consists of a large number of inexpensive and smart devices with multiple onboard sensors, networked through wired or wireless links and densely deployed, that cooperatively collect information of the physical world that embodies them and may control the surrounding environment [3.3, 3.4]. However, this definition is not very specific. In fact, national power grids, with their many sensors, can be considered as a large sensor network although they were developed before the term sensor network came into vogue. Despite their immense variety, all sensor networks have one fundamental feature in common: each sensor is limited in its ability to monitor a situation. The power of a sensor network comes from the fact that even though individual nodes are quite limited, the whole array becomes very powerful when networked. In this sense, wireless sensor networks (WSNs) exhibits one of its potential uses in the form of body sensor networks (BSN) for remote measurement of physiological signals.

As it was mentioned-above, healthcare is one of the fields of interest for the use of WSN. Despite the interest in the application of WSNs to healthcare, a significant gap remains between existing sensor network designs and the requirements of medical monitoring. Most WSNs are intended for the deployment of stationary nodes that transmit data at relatively low data rates, with the focus on best effort data collection at a central base station. By contrast, medical monitoring requires relatively high data rates, reliable communication, and multiple receivers.

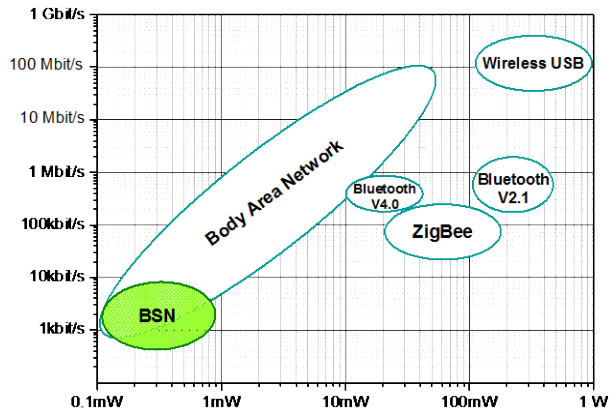

Figure 3.1. Average power consumption *vs* data rate of available wireless technologies.

Whilst WSN technology continues to evolve for the broad range of possible applications, it does not specifically tackle the challenges associated with human body monitoring and patient care. The principal reason is that most sensor network applications have very different data, communication, and lifetime requirements. Unlike WSN applications, medical deployments are characterized by mobile nodes with varying data rates and few opportunities for in-network aggregation. In addition, the human body environment is on a smaller scale and also requires a different type and a different frequency of monitoring.

Professor Guang-Zhong Yang was the first researcher who properly defined the term body sensor network (BSN) [3.5]. BSN technology represents the lower bound of power and bandwidth in the body area network (BAN) scenario [3.6]. A BAN is formally defined as a system of wireless devices in close proximity to or inside a person body that cooperate to enable monitoring for the benefit of the user [3.5]. When compared to conventional WSNs, BANs consist of a lower amount of smaller nodes, typically from 20 to 50 nodes, and provide less space coverage [3.7].

Figure 3.1 shows average power consumption and data rate for a number of popular wireless technologies. The range of BAN devices can vary significantly in terms of

Table III.I. Human biopotential and biophysical signals [3.8] and their typical data rate, bandwidth and accuracy.

	Data rate	**Bandwidth**	**Accuracy**
ECG (12 leads)	288 kbit/s	0.1 – 1000 Hz	12 bits
Electromyogram	320 kbit/s	5 – 10000 Hz	16 bits
EEG (12 leads)	50 kbit/s	0.1 – 100 Hz	12 bits
Movement	35 kbit/s	0 – 500 Hz	12 bits
Temperature	120 bit/s	0 – 1 Hz	8 bits
Blood saturation	16 bit/s	0 – 1 Hz	8 bits

bandwidth and power consumption in order to support a great variety of medical and non-medical applications and, hence, data rates vary from few kbit/s for simple data to several Mbit/s in video streams. The use of BANs in the medical area consists of wearable and implantable sensor nodes that sense biological information from the human body and transmit it wirelessly over a short distance to a control device worn on the body or placed in an accessible location. As shown in Table III.I, the data rates needed for vital-sign monitoring are usually low for the individual sensor.

The pursuit of long-term and continuous monitoring without human activity restriction has promoted the concept of BSNs. A BSN is a fusion of sensing and wireless technologies consisting of a series of miniaturized and low-power sensors wholly or partially covering the body area that collect, process, and communicate physiological information from the body [3.5], [3.9]. Those sensors can be either wearable or implantable. As illustrated in Fig. 3.2, one of the sensor acts as a master node, i.e., as a base station, for central control, and a number of vital sensors act as slave nodes. The base station thus play a different role from the slave nodes in the

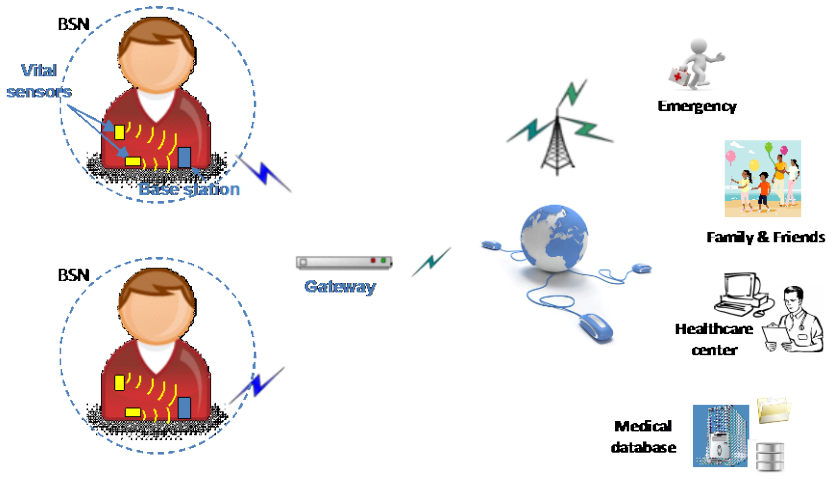

Figure 3.2. Architecture of a BSN in a pervasive eHealth scenario.

network, and it has more resources in terms of bigger size, available energy, longer radio range, and more computing power.

Although the challenges faced by BSNs are in many ways similar to BANs, there are several important differences between the very small and low-power sensors of BSNs and their BAN counterparts. First, the body itself prevents the reuse of the same node across many roles due to the particularities of measuring physiological data. Second, the proximity of the base station makes node-to-node communication largely unnecessary. BSNs tend to use star topology with each sensor node communicating only with the master node. Third, the sensor nodes have limited energy resources available as they have a very small form factor. In addition, for most sensors it is not possible to recharge or change the batteries although a long lifetime of the node is required.

The purpose of a medical sensor is to provide information to a physician as to the function and performance of an organ, a group of organs, or a system within the body of a patient. In the context of pervasive eHealth, the acquisition of biomedical signals,

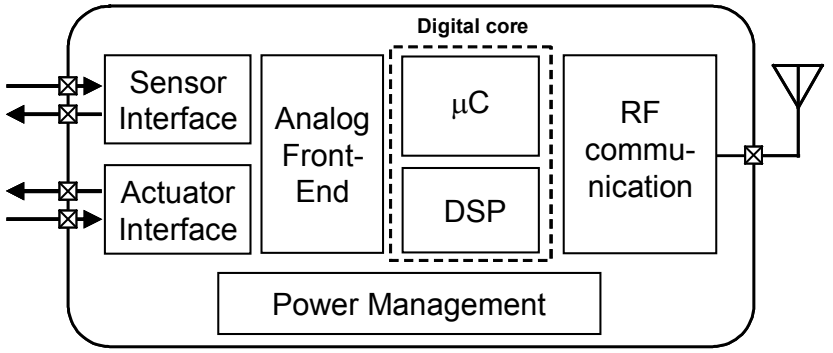

(a)

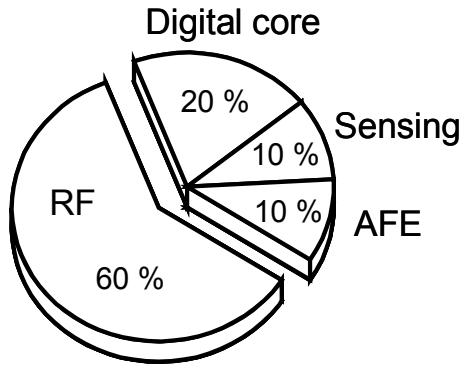

(b)

Figure 3.3. a) Conceptual block diagram and b) Power breakdown of a BSN sensor.

such as those for measuring vital signs, can be performed through BSN sensors attached on the patient's body or special wearable sensors. Most often, the acquisition of a biomedical signal is not sufficient and it is required to process the signal to get the relevant information buried in it. The transmission of the collected information to the base station is performed through an appropriate wireless technology.

As shown in Fig. 3.3 (a), a BSN sensor can be divided into five major function blocks: 1) the sensing/actuating components for biomedical sensing and stimulating, 2) an analog front-end for signal acquisition, 3) a digital core for controlling and local

processing, 4) a power-management unit, and 5) an active bidirectional radio frequency transceiver for data link. Although power consumption depends on the specific nature of the application, energy is mainly spent on processing sampled data by the microcontroller and forwarding the data out via a wireless link. Fig. 3.3 (b) shows the power breakdown of a BSN sensor illustrating this relationship, where in general communication accounts for the majority of the energy expenditure of a sensor.

At a first glance, a BSN sensor can be identified as an integrated smart sensor with wireless communication capabilities. Nowadays, technological developments in materials and electronics have led to the miniaturisation and integration of sensors into intelligent devices and systems that not only measure and analyse data but also act on the resultant information. The size and the cost of smart sensors have been decreasing with time, and the improvement in the technologies for other important components such as memory and radio transmitters will allow more capable and long lasting devices, also reducing their maintenance cost [3.10].

3.2.2. System description: structure and functionality

In this thesis a completely different approach for multichannel EBI measurement based on the operation principle of BSNs, with respect to the classical approaches described in section 2.2.4 of this work, has been undertaken. Figure 3.4 illustrates the basic concept of the proposed approach compared with the classical multichannel EBI techniques addressed above.

Basically, conventional multichannel approach consists on a single impedance analyzer wired-connected to the different bioimpedance channels needed for the required measurement. On the other hand, the proposed multichannel scheme is composed by a number of nodes acting each one as independent high-performance bioimpedance measurement instrument wirelessly connected to a central node. It is

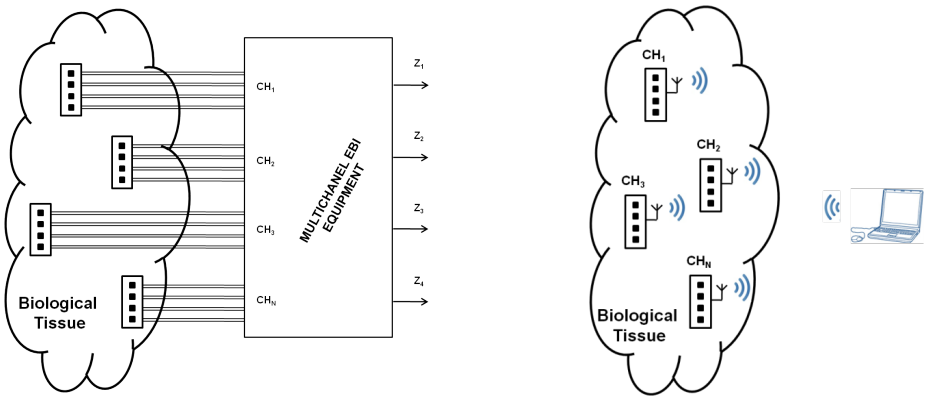

(a) (b)

Fig. 3.4. Conceptual scheme of multichannel EBI measurement systems:
a) Classical approach and b) Proposed architecture based on BSN.

assumed that nodes are identical but configurable modules, which provides the necessary flexibility and modularity to the whole system. Therefore, nodes must contain an AC programmable current generator, an EBI sensor, and controlling and transceiver units, as well as its own battery.

In addition, two important considerations must be taken into account for the node design. The PCB area occupied by a node should be small enough for guarantying the portability of the system. Therefore, a custom integrated circuit for the bioimpedance analog-front-end must be designed. The circuit performance must be high enough to relax the hardware and software requirements and thus, reduce the area and also the power consumption requirements. Besides, the magnitude and phase measuring ranges of a node must cover the corresponding variation ranges of such parameters in living organisms. Hence, each resulting wireless node must perform local, regional, and whole-body EBI analyses.

The proposed universal multichannel EBI measuring device is a BSN with a much more superior performance than any other multichannel approach reported up to now.

The following features of the proposed EBI-BSN are worth to be pointed out.

- scalability: The number of nodes –channels– is completely open to satisfy specific requirements, in contrast with classical multichannel approaches, where the number of channels is fixed in the design phase and is no more than a few units.
- flexibility: The functionality of each node is independently configured. That is, parameters such as EBI analysis or spectrometry operation, signal excitation frequency, analysis duration, etc., are defined for every EBI test.
- simultaneity: Nodes are independent EBI instruments capable of working at the same time or in any other operation mode –working by events–. This fact allows optimizing the current value injected in the body, whilst avoiding to overcome the maximum limit of 1 mA.
- applicability: A multichannel system based on BSN is open to different EBI application fields and R&D activities. It provides a lot of use possibilities, some still unknown;
- portability: Differently than classical systems, EBI-BSN multichannel are easily portable. It consists of a number small-size light-weight nodes and a device –laptop, tablet or even smart-phone– to control the network and show the measured results.

An EBI-BSN along with a specifically tailored user-friendly graphic development environment becomes a powerful R&D tool. The interface software allows the following operations.

- configuration: Implementing the network topology and the functional operation of nodes (coordinator, routers, and sensors) more suitable for a

specific EBI trial/application. Relative positions among nodes are also configurable;

- programming: Defining, by means of the wireless link, the functionality of every node (analysis or spectroscopy, time interval, analysis by EBI events, frequency range, etc.);
- analysis and graphical representation: Defining the mathematical operations (delays, time derivatives, integrals, ratios, etc.) to be performed over the EBI signals and/or measured results transmitted by nodes;
- customization: Storing different configuration, programming, and analysis settings for successive EBI trials.

3.2.3. High-performance wireless EBI spectrometer

In order to meet the requirements of the described social scenario for medical devices in Chapter 1 of this thesis, a technology platform for a number of BSN applications based on EBI technology, has been developed according to the approach outlined in section 3.2.2. In particular, a cost-effective CMOS silicon-chip implementation of a flexible high-performance EBI sensor has been considered as a feasible way to fulfil the objectives of this work, previously mentioned in Chapter 1. Of course, appropriate low-power low-voltage CMOS circuit design techniques have been incorporated in the design phase.

Figure 3.5 illustrates the main circuit sections of the proposed EBI node.

The CMOS analog front-end section –EBI sensor/spectrometer– injects a low level AC excitation current, detects the voltage signals in other two points of the biological tissue under test, and processes these signals to provide two DC voltages proportional

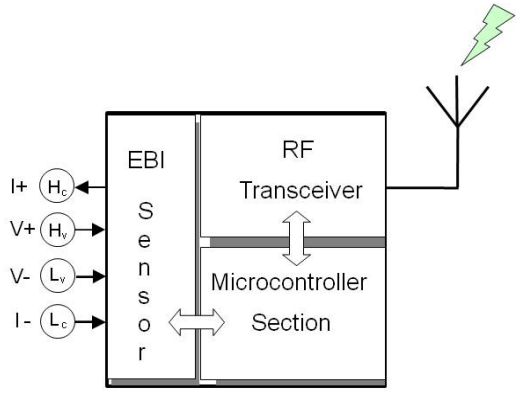

Figure 3.5. Functional blocks of the proposed EBI node.

to the magnitude and the phase, respectively, of the biological sample electrical bioimpedance. A tetrapolar system –two electrodes for current injection and two electrodes for voltage sensing– is used to decrease measurement errors caused by electrode/skin interface with respect to the case of its bipolar counterpart [3.11]. The microcontroller section supervises the operation of the whole node, controls the amplitude and the frequency of the excitation current source according to the program sequence to be implemented, and converts the resulting DC voltages representing the magnitude and the phase of the measured EBI to a digital code. At the same time, the microcontroller supports the calibration task for avoiding systematic measurement errors. The corresponding digital words are transmitted by the RF section to its corresponding BSN node-coordinator following a low-power, short-range wireless protocol such as ZigBee or Bluetooth low-energy.

A detailed block diagram of the proposed EBI sensor is shown in Fig. 3.6.

Basically, it consists of measuring the amplitude and the phase of a signal by using a gain-phase detector (GPD). More concretely, the sensor bases its operation in the MRPDD method which has been described in section 2.2.2. The excitation current is

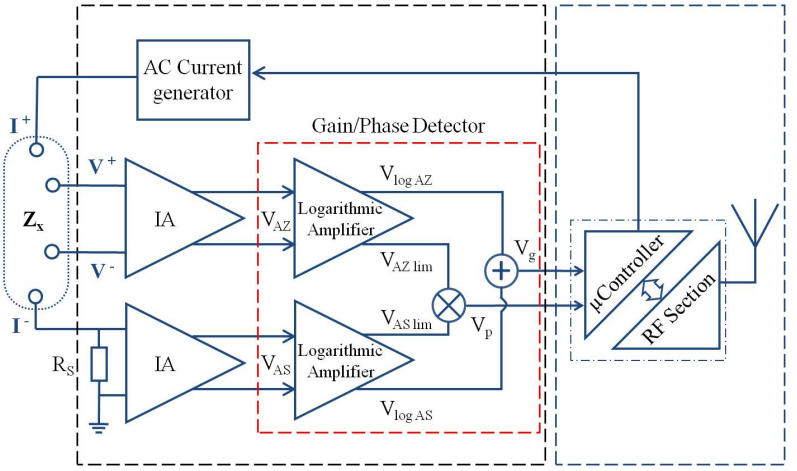

Fig. 3.6. Block diagram of an EBI-BSN node (EBI sensor is enclosed by black dashed box) [3.12].

injected through two electrodes (I+, I–) to stimulate the tissue having an unknown impedance Z_x. Excitation current also flows through a reference resistor R_s connected in series with Z_x. Two other electrodes (V+, V–) sense the voltage drop across Z_x, which is amplified by an instrumentation amplifier (IA). The voltage signal across R_s is amplified by a second IA. These two amplified voltage signals are processed by the GPD circuit so as to obtain two DC voltages proportional to their magnitude ratio $|K|$ and phase difference θ, respectively. If both instrumentation amplifiers are considered identical and having infinite input impedance, it is straightforward to obtain that the unknown impedance Z_x can be expressed as

$$Z_x = R_s \cdot |K| \angle \theta \tag{3.1}$$

The excitation current magnitude is chosen to be small enough so as not to be perceived by the patient, but large enough to produce voltage signals that are above interfering noise, which might arise from bioelectrical sources such as muscle tissues.

In practice, relatively small current magnitudes are involved, i.e., less than 1 mA, which are below the threshold of human perception.

The section enclosed by the red dashed box represents the block diagram of a very compact GPD, which consists of two matched limiting/logarithmic amplifiers (LLAs), a multiplier circuit, and a subtracting circuit. Each LLA is a non-linear amplifier which main function is obtaining the logarithmic version of the input signal, and, in particular, presents two voltage outputs: a) a pseudo-logarithmic output, V_{Log}, which represents a (pseudo-)logarithmic conversion of the input voltage, and b) a limited output V_{LA}, which is a saturated signal over most of the amplifier input dynamic range and varies linearly with the input voltage in the remaining part.

Essentially, the GPD utilizes two LLA structures coupled to circuitry that process the outputs provided by the LLAs to perform useful functions. Additionally, a phase detector can be utilized to measure the relative phase of two signals that are applied to the LLAs. In this sense it is desirable that the two LLAs are co-integrated as a single integrated circuit in order to improve accuracy in the implementation of a gain-phase detector. A detailed description of the operation and performance of the gain-phase-detector is given in Chapter 5 of this thesis.

The input signal of the two limiting/logarithmic amplifiers can be expressed as

$$V_{AZ} = \left|V_{AZ}\right| \cdot \sin(\omega_o t + \theta) \tag{3.2.a}$$

$$V_{AS} = \left|V_{AS}\right| \cdot \sin(\omega_o t) \tag{3.2.b}$$

The logarithmic output signals $v_{\log AZ}$ and $v_{\log AS}$ are given by the following equations:

$$v_{\log AZ} = v_{SLP} \cdot \log(V_{AZ} / V_N) \tag{3.3.a}$$

$$v_{\log AS} = v_{SLP} \cdot \log(V_{AS} / V_N) \tag{3.3.b}$$

where v_{SLP} and V_N are constant values determined by the limiting/logarithmic amplifier design. Taking the difference of the logarithmic outputs from the logarithmic amplifiers eliminates the intercept constant term, V_N, when measuring the ratio of two signals V_{AZ} and V_{AS}. Making use of the arithmetic of logarithms, the difference, v_g, between the two logarithmic output voltages can be described as

$$v_g = v_{SLP} \cdot \log\left(\frac{|V_{AZ}| \cdot \sin(\omega_o t + \theta)}{|V_{AS}| \cdot \sin(\omega_o t)}\right) = v_{SLP} \cdot \left[\log\left(\frac{|V_{AZ}|}{|V_{AS}|}\right) + \log\left(\frac{\sin(\omega_o t + \theta)}{\sin(\omega_o t)}\right)\right] \quad (3.4)$$

It can be derived from Eq. (3.4) that the DC value is proportional to the logarithm of the ratio between the amplitudes of the amplified versions of the two voltage electrodes and a reference resistor, respectively. The expression for the ratio relation is described by

$$v_{g,dc} = v_{SLP} \cdot \log\left(\frac{|V_{AZ}|}{|V_{AS}|}\right) \quad (3.5)$$

Thus, the intercept constant term, V_N, which depends on the specific design of the logarithmic amplifier and is source of error, is completely eliminated when determining v_g: indeed, v_g is simply proportional to the logarithm of V_{AZ}/V_{AS}, V_{SLP} setting the slope.

Another, separable, aspect involves the use of a phase detector to measure the relative phase of the two signals applied to the LLAs. However, rather than utilizing the logarithmic outputs, we utilize the limited outputs in each LLA, which are typically almost perfect, hard-limited square waves.

The phase relationship between the two input signals V_{AZ} and V_{AS} is embedded in

the limited outputs. A phase detector core, which is preferable implemented as a multiplier, processes the limited outputs to generate a phase output v_p. Trigonometric relations determine the GPD output with phase information, considering the main harmonic of the limited outputs of the limiting/logarithmic amplifiers expressed as

$$v_{AZ\lim} = V_{\lim} \cdot \sin(\omega_o t + \theta) \tag{3.6.a}$$

$$v_{AS\lim} = V_{\lim} \cdot \sin(\omega_o t) \tag{3.6.b}$$

The product of the expressions given by Eq. (3.6) can be established as

$$v_p = v_{AZ\lim} \times v_{AZ\lim} = V_{\lim}^2 \cdot \frac{1}{2} \cdot \left[\cos\theta\right] - V_{\lim}^2 \cdot \frac{1}{2} \cdot \left[\cos(2\omega_o t + \theta)\right] \tag{3.7}$$

From Eq. (3.7), the phase information is obtained by the DC component of v_p:

$$v_{p,dc} = V_{\lim}^2 \cdot \frac{1}{2} \cdot \left[\cos(\theta)\right] \tag{3.8}$$

So, the phase detector core can be added to the system to obtain a system that simultaneously measures both the gain and phase of the two input signals V_{AZ} and V_{AS} applied to the LLAs. This results in a very compact structure because the circuit that determines the difference utilizes the logarithmic outputs of the limiting/logarithmic amplifiers, whereas the phase detector core utilizes the limited outputs of the amplifiers.

Once the DC voltages carrying the magnitude and phase information of the complex bioimpedance has been obtained, the control section of the overall system should convert the voltages to the digital domain. It is important to point out that due to the fact that the signals that must be converted are DC values, it does not involve a

great complexity of the conversion circuitry which in turn means power saving. The measured information should be wirelessly transmitted using an RF circuit which is configured by the control section. In addition, the control section governs the current source generator block through the digital selection of the frequency and amplitude excitation signal. These control tasks can be performed by using low-power commercially available microcontrollers.

Finally, it is worth to point out that two operation modes of the EBI sensor ASIC have been considered. One of them is to be included as the analog front-end in the EBI-BSN node of the multichannel measurement system. Since a high-performance is a paramount characteristic of this system, the generator of the AC excitation electrical current (see Fig. 3.6) is an external block in order to provide wide programmability range in all parameters and definitively, higher flexibility and applicability in the general multichannel measurement system.

The second operation mode of the EBI sensor, however, is addressed to wearable/implantable bioimpedance applications. In such applications the working environment of the devices is, in general, very well defined. Therefore, a complete monolithic implementation of the AC current source have been carried out with a more limited performance with respect to previous mode. Chapter 6 deals with the design and practical performance of the current source generator. EBI sensor design trade-offs, such accuracy/power consumption, which are of special relevance for EBI applications, are discussed in following chapters dedicated to microelectronic design.

3.3. REFERENCES

[3.1] "21 ideas for the 21st century," *Business Week*, pp. 78-167, Aug. 1999.

[3.2] A. Pantelopoulos and N. G. Bourbakis, "A survey on wearable sensor-based systems for health monitoring and prognosis," *IEEE Transactions on Systems, Man, and Cybernetics–Part C: Applications and Reviews*, vol. 40, pp. 1-12, Jan. 2010.

[3.3] C.–Y. Chong and S. P. Kumar "Sensor networks: evolution, opportunities, and challenges," *Proceedings of the IEEE*, vol. 91, pp. 1247-1256, Aug. 2003.

[3.4] R. Verdone, D. Dardari, G. Mazzini, and A. Conti, *Wireless sensor and actuator networks*, Academic Press, 2008.

[3.5] K. Van Dam, S. Pitchers, and M. Barnard, "From PAN to BAN: Why body area networks?," *Wireless World Research*, Second Meeting, 2001.

[3.6] G. Z. Yang, *Body sensor networks*, Springer-Verlag, 2006.

[3.7] B. Latré, B. Braem, I. Moerman, C. Blondia, and P. Demeester, "A survey on wireless body area networks," *Journal of Wireless Networks*, vol. 17, pp. 1-18, Jan. 2011.

[3.8] J. H. Nagel, "Biopotential amplifiers," *Medical devices and systems*, CRC Press, Ch. 52, pp. 1-14, 2006.

[3.9] M. A. Hanson *et al.*, "Body area sensor networks: Challenges and opportunities," *IEEE Computer*, vol. 42, pp. 58-65, Jan. 2009.

[3.10] J. H. Huijsing, "Smart sensor systems: Why? Where? How?," *Smart sensor systems*, U.K., Wiley, Ch. 1, pp. 1-21, 2008.

[3.11] A. O. Ragheb, L.A. Geddes, J. D. Bourlan, and W. A.Tacker, "Tetrapolar electrode system for measuring physiological events by impedance," *Medical & Biological Engineering & Computing*, vol. 30, pp. 115-117, Jan. 1992.

[3.12] J. L. Ausín, J. Ramos, J. F. Duque, "Unit, modular system and method for measuring, processing and remotely monitoring electrical bioimpedance," Patent Num. P201131426, 30-August-2011. International application: PCT/ES2012/070635, 29-August-2012.

Chapter 4

INSTRUMENTATION AMPLIFIER

This Chapter deals with the instrumentation amplifier included in the bioimpedance sensor ASIC. In particular, first, design considerations and trade-offs are discussed and from them, the corresponding specifications are defined. Next, the design of the preamplifier and its realization in a standard CMOS technology are provided. Finally, the Chapter concludes with the experimental behavior of the instrumentation amplifier obtained from the measurement of a test-chip prototype.

4.1. SPECIFICATIONS AND DESIGN CONSIDERATIONS

Instrumentation amplifiers (IAs) are essential analog circuits at the front-end of any readout system that deals with low-level signals in the presence of large common-mode interferences. This is the case of bioelectric recordings such as a typical electrical bioimpedance measurement system, where a differential alternating current is applied through a pair of surface electrodes to the body tissue and the resulting voltages are picked up by another electrode pair for further processing [4.1]. Differential signals measured between electrodes in electrical bioimpedance measurement can be as small as few tenths of a microvolt (μV), whereas the common-mode interference can be in the hundreds of millivolts (mV) range. In particular, the amplitude of the signals to be measured in applications addressed by this work is approximately in the range from 10 μV to 15 mV in a frequency range that goes from 1 kHz to 1 MHz.

An instrumentation amplifier is usually the first stage in the sensor system and, consequently, it is strongly affected by high-level common-mode signals coupled to the human body from the measuring system. There are two main mechanisms by which a high-common mode voltage may adversely affect electrical bioimpedance measurements. The first one is due to the finite common-mode rejection ratio (CMRR) of the amplifier. This mechanism is often not problematic with amplifiers where a common-mode rejection ratio of 80-90 dB is provided [4.2, 4.3]. A second and much more important way refers to the fact that a high common-mode voltage may cause interference when there are differences (mismatches) in electrode impedances and/or input impedances, which convert common-mode voltage into a differential input voltage. This mechanism has been called *the potential divider effect* [4.4, 4.5], and it is the main reason of the importance of reducing the common-mode voltage as much as possible. Another kind of common-mode interference in electrical bioimpedance measurements occurs when not the whole current injected into the body during the measurement flows into the tissue under test [4.6]. Consequently, the front-end

amplifier is required to have high-input impedance to prevent a part of the injected current from being shunted into the recording electrodes, which would cause errors in the measurement.

Another important parameter that affects the design of the instrumentation amplifier concerns the acceptable noise level of the circuit, taking the magnitude of the signals involved in biomedical applications into account. As referred in previous chapters of this work, several electrical bioimpedance spectroscopy applications involve measurements over a wide frequency range (from a few kHz up to 1 MHz). Since the bandwidth (BW) of electrical bioimpedance applications extends to relatively high frequencies (≈ 1 MHz), the thermal noise component dominates over the flicker noise component of the overall noise contribution and must be taken into account during the design of the instrumentation amplifier. Several low-noise monolithic IAs for biomedical applications have been reported previously [4.7-4.9]. However, these approaches require supply voltages higher than 3 V. Although low-voltage IAs have also been reported [4.10], they generally exhibit high noise level at low frequencies and are not suitable for biomedical signal processing.

Consequently, electrical bioimpedance applications require the design of an instrumentation amplifier with high common-mode rejection ratio for avoiding interferences of common-mode voltages, high-input impedance for avoiding current not flowing into human body, and a good noise performance over the bandwidth of interest. Furthermore, low voltage and low-power consumption operation is desirable as most portable biomedical monitoring systems operate under battery power supply.

Early approaches for the design of instrumentation amplifiers for physiological signals were based on the classical configuration with two or three operational amplifiers, which actually could accomplish the desired feature of high common-mode rejection ratio required for biomedical applications [4.11-4.17]. The conventional instrumentation amplifier based on three operational amplifiers is probably the most

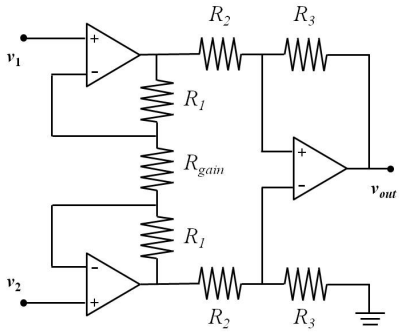

Figure 4.1. Conventional three-opamp instrumentation amplifier structure.

well-known structure able to extract and amplify low-amplitude differential signals [4.18]. In this topology, two operational amplifiers are used to implement a pseudo fully-differential buffer, which is followed by single operational amplifier configured as a differential amplifier. The widely used conventional instrumentation amplifier structure with resistive feedback is shown in Fig. 4.1.

The main properties of this conventional circuit architecture are high-input impedance, high CMRR, and simple gain control [4.19-4.21]. However, the CMRR of the conventional three-opamp IA has a limited value due to the need for accurate and precise matching of the resistors that implement the feedback networks [4.22, 4.23]. This matching usually requires laser-trimmed resistors, which is an expensive technique and not available in standard CMOS fabrication processes. Indeed, this conventional topology needs operational amplifiers with low output impedance to drive the feedback resistors. The requirement of low output impedance amplifiers implies high DC current levels which makes this conventional structure not suitable for low-power integrated sensor systems because of the excessive power dissipation.

A second circuit technique for implementing instrumentation amplifiers consists of using switched-capacitor (SC) circuits [4.24, 4.25]. However, the main drawback of the switched-capacitor approach is the fold-over of noise above Nyquist frequency [4.26].

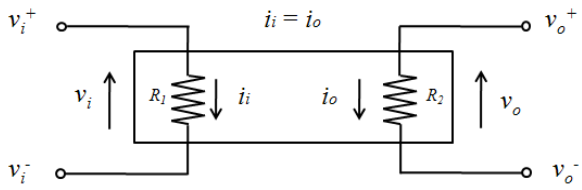

Figure 4.2. Conceptual circuit schematic of current-feedback instrumentation amplifier.

Thus, neither the three-opamp nor the SC approaches are convenient for low-power and low noise front-ends.

An approach to design IA more appropriate for monolithic implementation was proposed by Krabbe in 1971 [4.27]. The IA structure does not need any matched resistors or trimmed components for achieving high CMRR. Instead, the operation of the circuit is based on common-mode voltage isolation and techniques for balancing the currents of the input stage to obtain an improved value of CMRR, whereas the gain is defined by the ratio of two resistors. The input stage of the amplifier is designed to isolate the common-mode input voltage from the rest of the circuit and, because isolation will never be perfect, additional balancing is used to enhance the CMRR. The technique is widely known as current feedback due to the use of current balancing for achieving high CMRR. In addition, the current feedback approach offers a higher operating BW than resistive feedback for the same biasing current [4.28]. Additionally, there is no need for low output impedance amplifiers.

Current-feedback instrumentation amplifier is a well-established alternative that tackles the different drawbacks inherent in the conventional three-opamp instrumentation amplifier topology, whose basic structure is presented in Fig. 4.2.

The current-feedback technique became a standard for instrumentation amplifiers and was later applied to the design of many monolithic instrumentation amplifiers [4.29-4.32] where, together with a high-pass filter, these current feedback

instrumentation amplifiers can be used to filter the DC electrode offset [4.8, 4.9]. Important contributions were reported by Martins *et al.* [4.8], Brokaw and Timko [4.30], van de Plassche *et al.* [4.31], and, more recently, by Zhao *et al.* [4.33] and by Worapishet *et al.* [4.34], with the development of clever circuits, which implement instrumentation amplifiers that exploit this current-balancing technique.

Referring to Fig. 4.2, circuital analysis of the input and the output stage gives rise to the following expression for the gain of a current-feedback instrumentation amplifier:

$$\begin{aligned} i_i &\equiv i_o \\ \frac{v_i}{R_1} &= \frac{v_o}{R_2} \\ \frac{v_o}{v_i} &= \frac{v_o^+ - v_o^-}{v_i^+ - v_i^-} = \frac{R_2}{R_1} \end{aligned} \tag{4.1}$$

where R_1 and R_2 are the resistances in the output and the input section, respectively.

A typical current feedback IA basically consists of a resistive-degenerated input transconductor, which operates as a *V-I* converter, a resistive-degenerated output transconductor, which is feedback connected so as to substantially operate as an *I-V* converter, and one or more high-gain feedback loops. In the input section, the input differential voltage signal v_i is converted into a current i_i, which is then transferred to the output section, usually with unity gain.

In the output section, this current, which is now named i_o, is converted into a voltage by means of a resistor, whose value, together with the value of the degeneration resistor in the input stage, establishes the overall gain. If a single feedback loop is applied around the two transconductors, the IA is classified as direct [4.9] or indirect [4.35] current feedback amplifier. In the direct current feedback IA, the two transconductors are stacked, and this limits the input common-mode voltage

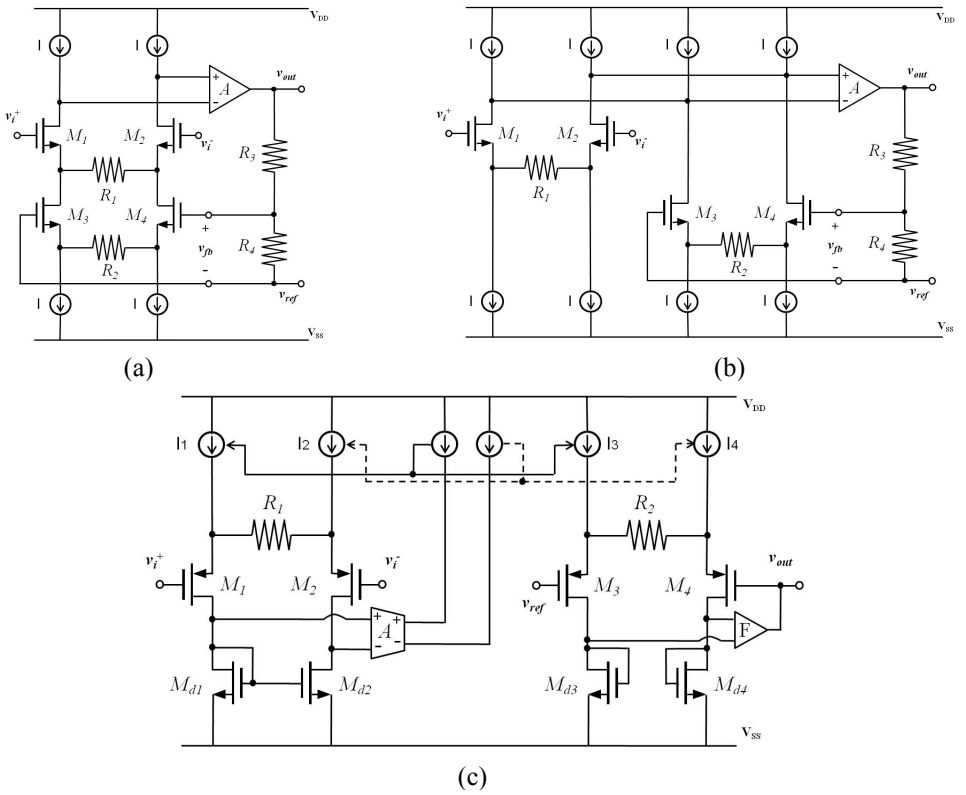

Figure 4.3. a) Direct current-feedback structure [4.9]; b) Indirect current-feedback structure [4.35] and c) Local current-feedback structure [4.30].

range and the minimum supply voltage, which is avoided for the case of the indirect structure. If two separate local feedback loops are used around the input and the output transconductor, respectively, the IA is classified as local current feedback IA [4.30]. Both the direct and indirect current feedback IA topologies are affected by a number of parasitic poles associated with each of the stages in the loop. As result, this makes frequency compensation difficult and limits operation frequency. On the contrary, in the local current feedback IA topology, each local loop contains a smaller number of internal parasitic poles and, thus, this topology potentially offers a higher operating BW for a given current consumption.

Figure 4.3 illustrates the structures of the direct, the indirect and the local current-feedback topology.

4.2. CIRCUIT DESIGN AND IMPLEMENTATION

A number of different current feedback IA topologies have been evaluated as suitable candidates for the target specifications previously mentioned. High-frequency and low-voltage performance of the instrumentation amplifier is required for the target bioelectrical impedance application. Consequently, the local feedback instrumentation amplifier topology has been chosen for the proposed design. In this structure a reduced number of stacked transistors is necessary, thus improving DC behavior at low voltage supplies. In addition, only a pair of transistors is needed in the input stage, which results in an optimal noise performance.

Figure 4.4 shows the circuit diagram of the designed CMOS instrumentation amplifier for electrical bioimpedance spectrometry. The whole circuit is composed of

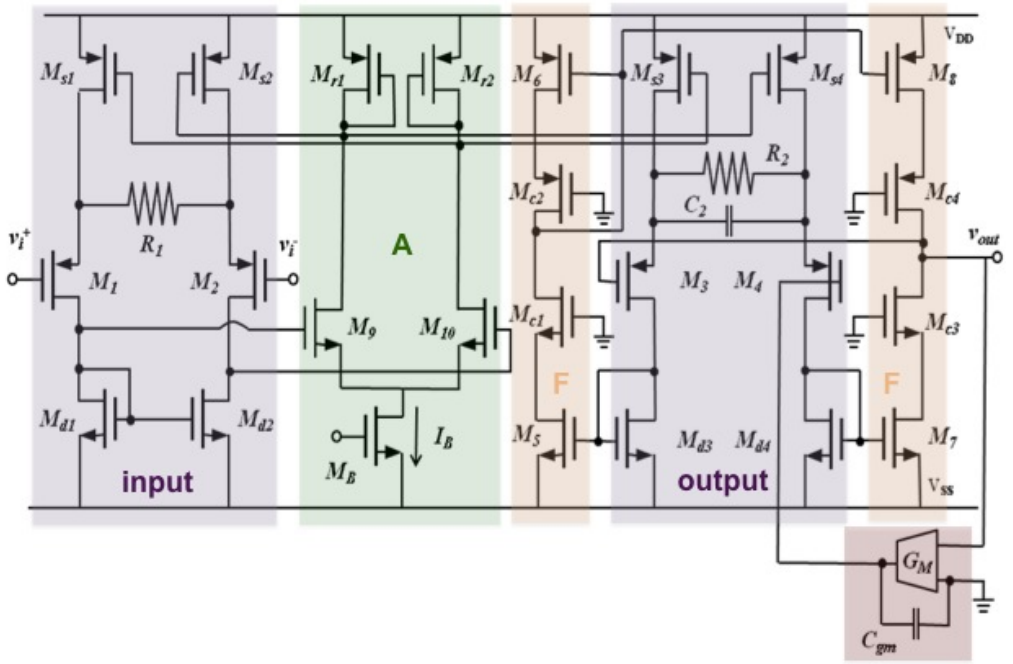

Figure 4.4. Circuit schematic of the proposed instrumentation amplifier.

three different stages, namely an input stage, a feedback stage (amplifier *A*) around this input stage, and an output stage (that also includes a local feedback loop, *F*). The input transconductor stage consists of a differential pair, M_1 and M_2, in degenerated common source configuration with a high transconductance of the input pair in order to allow achieving a good linearization of the pair. PMOS transistors exhibit low flicker noise and, consequently, have been used as input devices.

The feedback amplifier (*A* in Fig. 4.3) is implemented by a simple differential pair (transistors M_9, M_{10} biased by M_B and loaded by M_{r1}, M_{r2}) and serves to exactly balance the drain currents of transistors M_1 and M_2 (and, hence, the gate-to-source voltages of these two devices) by adjusting the complementary currents through M_{s1} and M_{s2}, I_{Ms1} and I_{Ms2} (provided that the current feedback gain is sufficiently large). A direct result of this is that the input differential voltage $v_i = v_i^+ - v_i^-$ is forced across resistor R_1, which means that transistors M_1 and M_2 of the input stage essentially act as a unity-gain buffer. Similarly, the output stage is realized by a differential pair, M_3 and M_4, in degenerated common source configuration together with a high-gain CMOS operational transconductance amplifier with cascode transistors pairs (*F* in Fig. 4.3, transistors M_5 to M_8 and M_{c1} to M_{c4}), which exactly balances the drain currents of transistors M_3 and M_4 in the output transconductor stage, so that these two transistors also act as a voltage buffer, and the voltage across their gates turns out to be equal to the voltage across resistor R_2.

When no signal is applied, ideally, the circuit is perfectly balanced, so all currents in the corresponding components are equal and v_{out} is set to quiescent point. When a differential signal is applied, the output currents of the transconductance amplifier, *A*, become unbalanced in order to maintain the drain currents of M_1 and M_2 equal. In this situation, if these two transistors are well matched, their gate-to-source voltages are ideally equal and, hence, as pointed out above, the input voltage is applied across resistor R_1. Since the currents through M_{s3} and M_{s4}, I_{Ms3} and I_{Ms4}, are exact copies of

I_{Ms1} and I_{Ms2}, respectively, the feedback loop around the output stage makes the voltage across resistor R_2 and, therefore, the voltage across the gates of M_3 and M_4, to be equal to $(R_2/R_1)v_i$. Hence, the DC gain of the IA is given by the ratio R_2/R_1.

Since the BW of the IA extends to high frequencies, IA noise performance is dominated by thermal noise. Hence, using only the thermal noise contribution and neglecting flicker noise components, the input-referred voltage noise of the IA can be calculated as

$$\frac{\overline{v_{iN}^2}}{\Delta f} = 4kTR_1 + 2\left(4kT\frac{2}{3}\frac{1}{g_{m1,2}} + 4kT\frac{2}{3}\frac{g_{md1,2}}{g_{m1,2}^2}\right) \tag{4.2}$$

where k is the Boltzmann´s constant, T is the absolute temperature, g_{mi} and g_{mdi} (i = 1, 2) are the small-signal transconductance and the small-signal output conductance, respectively, of transistor M_i, and Δf is the BW in Hz over which the noise is measured. It is apparent from the equation above that in order to minimize the thermal noise contribution of resistor R_1, its resistance must be set to a small value.

The amplitude of the signals to be processed in our application is approximately in the range from 10 μV to 15 mV. The maximum allowed differential input signal range of the proposed IA, is determined by the product of the DC bias current source I_B and R_1, which corresponds to a completely unbalanced input pair. Increasing the input signal much beyond this limit, would result in appreciable output harmonic distortion. In this respect, the values of DC bias current I_B and input stage degeneration resistor R_1, must be carefully selected. A high value of I_B increases the linear input signal range, but also leads to high power consumption. At the same time, it should be taken into account that, for the target frequency range, thermal noise dominates over flicker noise and, therefore, small values of R_1 should be used in order to reduce noise

contributions. Thus, the need for a trade-off choice between input range on the one side and power consumption and noise on the other exists.

The instrumentation amplifier was designed for a differential gain of 2.5 (≈ 7.9 dB). To this end, R_1 and R_2 were set to 800 Ω and 2 kΩ, respectively. With the aim of reducing the noise, the instrumentation amplifier also incorporates circuitry that implements a bandpass filter (1 kHz-1 MHz). Connecting a capacitor (C_2) in parallel with resistor R_2 a pole is introduced, which sets a –3 dB high cutoff frequency equal to

$$f_H = (2\pi R_2 C_2)^{-1} \tag{4.3}$$

It should be pointed out that a high value of the DC gain of the feedback loop around the input stage, given by the product of the transconductances, $g_{m9,10}$, of $M_{9,10}$ and the equivalent impedance at the drain of the input transistors (M_1, M_2), is required to exactly balance the drain currents of these two transistors. Nevertheless, increasing the value of $g_{m9,10}$ involves higher sizes of transistors $M_{9,10}$ and, consequently, higher parasitic capacitances at their gate nodes for any given value of I_B. Hence, The frequency of the internal parasitic pole, f_p, associated to the drain of input transistor M_2, as given by Eq. (4.4), might be designed to be negligible in comparison with the –3 dB cutoff frequency f_H of the IA (i.e. $f_p << f_H$). We have:

$$f_p = \frac{1}{2\pi R_{eq} C_{eq}} \tag{4.4}$$

where

$$R_{eq} \approx 1 \Big/ \left(g_{ds,Md_2} + g_{dsM_2} \right) \tag{4.5}$$

$$C_{eq} \approx C_{gs,M_{10}} + C_{d,M_{d2}} + C_{d,M_2} \tag{4.6}$$

In Eq. (4.6), the Miller effect over the gate-to-drain capacitance of transistor M_{10} has been neglected due to the low value of the gate capacitance for the corresponding technology.

The high-pass filter portion of the bandpass filter is more difficult to implement. The use of a passive *RC* filter is not a good solution for such a low cut-off frequency due to the need for high capacitance values, which in turn means capacitors with high size and, consequently, high area occupation. Hence, the high-pass filter was implemented by using another feedback loop based on a trasnsconductor, G_M, and a capacitor, C_{gm}, around the output stage, as shown in Fig. 4.4. Transconductor G_M acts as a resistor, but offers two advantages over a passive resistor. First, as it is possible to make its transconductance low, a high equivalent resistor (R_{eq} > 1MΩ) can be obtained. Second, there is no resistive loading of the output. The presence of the first-order high-pass G_M-*C* filter in the output stage introduces a pole, which determines the lower cutoff frequency of the instrumentation amplifier, given by

$$f_L = \frac{G_M}{2\pi C_{gm}} \tag{4.7}$$

In order to maximize the CMRR of the instrumentation amplifier, the value of $1/R_1$ and the transconductances of the input pair transistors, $g_{m1,2}$, should be maximized so as to minimize the multiplying factor $1/(g_{m1,2}.R_1)$ which affects proportionally the amplifier common-mode gain [4.32], [4.34]. For the same purpose, high values of the output resistance of current sources $M_{s1,2}$ and the transconductances of transistors $M_{d1,2}$ should be set as high as possible, which has been recognized to provide improvement on the low-frequency CMRR current-feedback IA performance [4.34].

4.3. POST-LAYOUT AND EXPERIMENTAL RESULTS

The designed instrumentation amplifier was laid out and fabricated in double-poly, triple-metal 0.35-μm CMOS technology and, then, experimentally evaluated. Figure 4.5 corresponds to the IA chip microphotograph. It occupies an active area of 0.037 mm^2 with an output buffer, which was included just for testing purposes.

The measured power consumption of the instrumentation amplifier when using a single 2-V supply is 240 μW, which is very low for medical applications of bioelectrical impedance analysis over the target frequency interval from 1 kHz to 1 MHz.

Experimental and post-layout simulations using Cadence Spectre were carried out to evaluate the performance of the designed amplifier. Simulated CMRR values of 125 dB at frequencies close DC and 80 dB at 1 MHz were achieved. Figures 4.6 and 4.7 illustrate the measured small-signal gain and phase response of the fabricated amplifier, respectively.

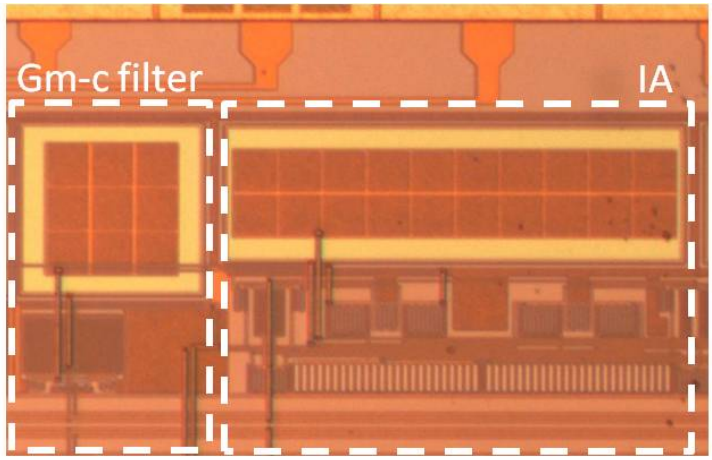

Figure 4.5. Microphotograph of the fabricated instrumentation amplifier.

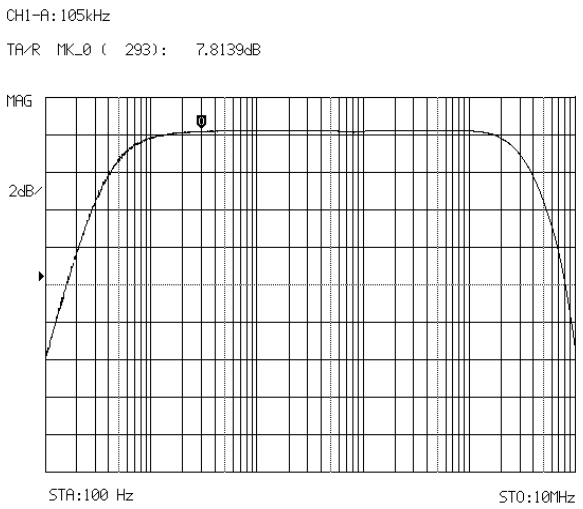

Figure 4.6. Measured magnitude of the frequency response of the designed instrumentation amplifier.

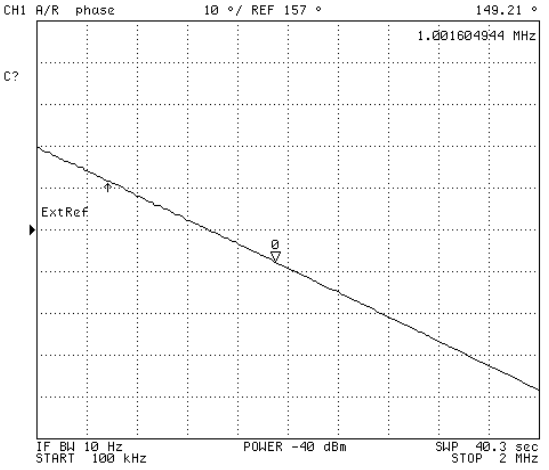

Figure 4.7. Measured phase of the frequency response of the designed instrumentation amplifier.

As shown in Fig. 4.6, a flat small-signal gain of 7.82 dB (≈ 2.46) was obtained over the whole frequency range of interest. The –3dB bandpass bandwidth of the amplifier

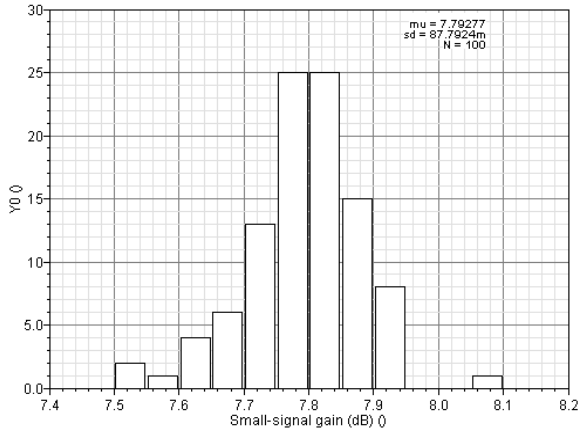

Figure 4.8. Post-layout Monte Carlo simulations for midband small-signal gain.

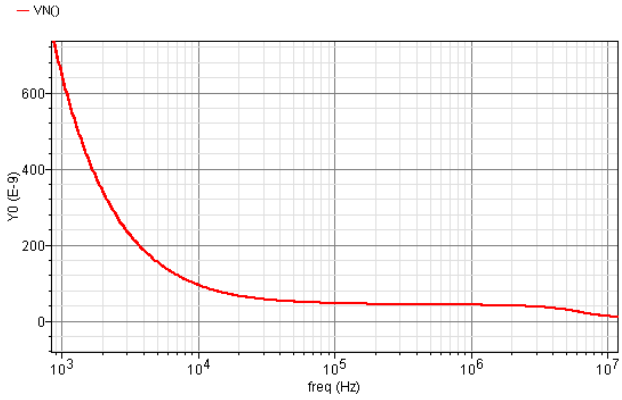

Figure 4.9. Post-layout simulated equivalent output noise of the designed instrumentation amplifier.

goes from 350 Hz to 4.4 MHz. Figure 4.8 illustrates the simulated small-signal gain variations in the presence of fabrication process mismatches.

The post-layout simulated input referred noise, integrated over the whole bandwidth, was about 36 µVrms. In order to compare the noise performance of the designed and other proposed IA circuits, the noise efficiency factor (*NEF*) was used as figure of merit [4.9]. *NEF* is given by the expression:

$$NEF = V_{rms,in}\sqrt{\frac{2\cdot I_{tot}}{\pi\cdot U_T\cdot 4kT\cdot BW}} \tag{4.8}$$

where I_{tot} is the total current drain in the system, $V_{rms,in}$ is the total equivalent input-referred noise, BW is the -3 dB bandwidth of the amplifier, and V_T is the thermal voltage ($V_T = kT/q$, q being electron charge). For the designed IA, circuit the *NEF* calculated according to Eq. (4.8) results 7.66.

Table IV.I provides a comparison of the experimental behavior of the proposed IA and a recently published solution implemented in similar fabrication technology [4.34]. The proposed IA shows higher bandwidth, less active area, and lower power consumption with respect to the previous solution with a comparable noise efficiency factor.

Table IV.I. Performance comparison of the proposed IA and [4.34].

Parameters	This work	[4.34] (measurements)
Technology	0.35-µm CMOS 3M 2P	0.35-µm CMOS 4M 2P
Active area (with output buffer for testing)	0.037 mm^2	0.068 mm^2
Power Supply	2 V	3 V
Power consumption	240 µW (without output buffer)	870 µW (without output buffer)
Gain	2.46 V/V	50 V/V
Bandwidth (–3 dB)	4 MHz	2 MHz
DC offset	2.8 mV	1.5 mV
Total input-referred voltage noise	36 μV_{rms} (BW = 1 Hz – 4 MHz) (post-layout simulation)	16 μV_{rms} (BW = 1 Hz – 3 MHz)
NEF	7.66 (BW = 4 MHz)	6.1 (BW = 3 MHz)
CMRR	80dB @ 1MHz (post-layout simulation)	90dB @ 2MHz

4.4. REFERENCES

[4.1] S. Grimnes and Ø. G. Martinsen, *Bioimpedance and Bioelectricity Basics* (2nd edition), Academic Press, 2008.

[4.2] A. C. Metting van Rijn, A. Peper, and C. A. Grimbergen, "High-quality recording of bioelectric events. Part I: Interference reduction, theory and practice," *Medical & Biological Engineering & Computing*, vol. 28, pp. 389-397, Sept. 1990.

[4.3] J. Zhou and J. Liu, "On the measurement of common-mode rejection ratio," *IEEE Transactions on Circuits and Systems–II, Express Briefs*, vol. 52, pp. 49-53, Jan. 2005.

[4.4] J. Huhta and J. Webster, "60 Hz interference in electrocardiography," *IEEE Transactions on Biomedical Engineering*, vol. 20, pp. 91-101, March 1973.

[4.5] A. Pacela, "Collecting the body's signals," *Journal of Electronics*, vol. 40, pp. 103-112, July 1967.

[4.6] J. Rosell and R. Riu, "Common-mode feedback in electrical impedance tomography," *Clinical Physics and Physiological Measurement*, vol. 13, pp. 11-14, Jan. 1992.

[4.7] R. R. Harrison and C. Charles, "A low-power low-noise CMOS amplifier for neural recording applications," *IEEE Journal of Solid-State Circuits*, vol. 38, pp. 958-965, June 2003.

[4.8] R. Martins, S. Selberherr, and F. A. Vaz, "A CMOS IC for portable EEG acquisition systems," *IEEE Transactions on Instrumentation and Measurement*, vol. 47, pp. 1191-1196, Oct. 1998.

[4.9] M. S. J. Steyaert, W. M. C. Sansen, and C. Zhongyuan, "A micropower low-noise monolithic instrumentation amplifier for medical purposes," *IEEE Journal of Solid-State Circuits*, vol. 22, pp. 1163-1168, Dec. 1987.

[4.10] H. Huang, S. Karthikeyan, and E. K. F. Lee, "A 1 V instrumentation amplifier," *42nd IEEE Midwest Symposium on Circuits and Systems* (MWSCAS), vol. 1, pp. 170-173, Aug. 1999.

[4.11] R. P. Areny and J. G. Webster, "AC instrumentation amplifier for bioimpedance measurement," *IEEE Transactions on Biomedical Engineering*, vol. 40, pp. 830-833, Aug. 1993.

[4.12] C. Kitchin and L. Counts, *A Designer's Guide to Instrumentation Amplifiers*, U.S.A, Analog Devices, Inc., 2000.

[4.13] M. J. Burke and D. T. Gleeson, "A micropower dry-electrode ECG preamplifier," *IEEE Transactions on Biomedical Engineering*, vol. 47, pp. 155-162, Feb. 2000.

[4.14] E. Spinelli, R. Pallas-Areny, and M. A. Mayosky, "AC-coupled front-end for biopotential measurements," *IEEE Transactions on Biomedical Engineering*, vol. 50, pp. 391-395, March 2003.

[4.15] C. J. Yen, W. Y. Chung, and M. C. Chi, "Micro-power low-offset instrumentation amplifier for biomedical system applications," *IEEE Transactions on Circuits and Systems–I, Regular Papers*, vol. 51, pp. 691-699, April 2004.

[4.16] E. M. Spinelli, N. Martinez, M. A. Mayosky, and R. Pallas-Areny, "A novel fully differential biopotential amplifier with DC suppression," *IEEE Transactions on Biomedical Engineering*, vol. 51, pp. 1444-1448, Aug. 2004.

[4.17] C.-C. Wang, C.-C. Huang, J.-S. Liou, Y.-J. Ciou, I.-Y. Huang, C.-P Li, Y.-C. Lee, and W.-J. Wu, "A mini-invasive long term bladder urine pressure measurement ASIC and system," *IEEE Transactions on Biomedical Circuits and Systems*, vol. 2, pp. 44-49, March 2008.

[4.18] P. Horowitz and W. Hill, *The Art of Electronics*, U.K., Cambridge Univ. Press, 1989.

[4.19] G. E. Tobey, J. G. Graeme, and L. P. Huelsman, *Operational Amplifiers: Design and Applications*, McGraw-Hill, pp. 206-207, 1971.

[4.20] F. D. Stott and C. Weller, "Biomedical amplifiers using integrated circuits," *Medical and Biological Engineering*, vol. 14, pp. 684-687, Nov. 1976.

[4.21] J. G. Webster, *Medical Instrumentation: Application and Design*, U.S.A., Houghton Mifflin Co., pp. 111-112, 1978.

[4.22] J. H. Huijsing, *Operational Amplifiers: Theory and Design*, U.S.A, Kluwer Academic, 2001.

[4.23] M. A. Smither, D. R. Pugh, and L. M. Woolard, "CMRR analysis of the 3-opamp instrumentation amplifier," *Electronics Letters*, vol. 13, pp. 594, Sept. 1977.

[4.24] M. Degrauwe, E. Vitoz, and I. Verbauwhede, "A micropower CMOS instrumentation amplifier," *IEEE Journal of Solid-State Circuits*, vol. 20, pp. 805-807, June 1985.

[4.25] P. M. Van Petegem, I. Verbauwhede, and W. M. C. Sansen, "Micropower high-performance SC building block for integrated low-level signal processing," *IEEE Journal of Solid-State Circuits*, vol. 20, pp.837-844, Aug. 1985.

[4.26] C. C. Enz and G. C. Temes, "Circuit techniques for reducing the effects of opamp imperfections: Autozeroing, correlated double sampling, and chopper stabilization," *Proceedings of the IEEE*, vol. 84, pp. 1584-1614, Nov. 1996.

[4.27] H. Krabbe, "A high performance monolithic instrumentation amplifier," *IEEE International Solid-State Circuits Conference*, pp.186-187, Feb. 1971.

[4.28] C. Toumazou, F. J. Lidgey, and D. G. Haigh, *Analogue IC design: the current-mode approach*, U.K., Peter Peregrinus Ltd., Ch.16, pp.569-595, 1990.

[4.29] F. L. Eatock, "A monolithic instrumentation amplifier with low input current," *IEEE International Solid-State Circuits Conference. Digest of Technical Papers*, pp. 148-149, Feb. 1973.

[4.30] A. P. Brokaw and M. P. Timko, "An improved monolithic instrumentation amplifier," *IEEE Journal of Solid-State Circuits*, vol. 10, pp. 417-423, Dec. 1975.

[4.31] R. J. van de Plassche, "A wide-band monolithic instrumentation amplifier," *IEEE Journal of Solid-State Circuits*, vol. 10, pp. 424-431, Dec. 1975.

[4.32] P. A. dal Fabbro and C. A. dos Reis Filho, "An integrated instrumentation amplifier with improved CMRR," *15th Symposium on Integrated Circuits and Systems Design* (SBCCI), pp. 57-61, Sept. 2002.

[4.33] Y.–Q. Zhao, A. Demosthenous, and R. H. Bayford, "A CMOS instrumentation amplifier for wideband bioimpedance spectroscopy systems," *Proceedings of the IEEE International Symposium on Circuits and Systems (ISCAS)*, pp. 5079-5082, May 2006.

[4.34] A. Worapishet, A. Demosthenous and X. Lu, "A CMOS instrumentation amplifier with 90-dB CMRR at 2-MHz using capacitive neutralization: analysis, design considerations, and implementation," *IEEE Transactions on Circuits and Systems–I, Regular Papers*, vol. 58, pp. 699-710, April 2011.

[4.35] B. J. van den Dool and J. H. Huijsing, "Indirect current feedback instrumentation amplifier with a common-mode input range that includes the negative rail," *IEEE Journal of Solid-State Circuits*, vol. 28, pp. 743-749, July 1993.

Chapter 5

GAIN-PHASE DETECTOR

Design considerations on CMOS Gain-Phase detectors, and limiting amplifiers to be used as basics building blocks in power-efficient wide-band logarithmic amplifiers for bioimpedance measurements, are discussed in this Chapter. Next, several approaches of low-voltage gain cell topologies to be incorporated as basic cell of the limiting amplifier are presented. Statistical analyses and results obtained from the experimental characterization of a test-chip prototype are also shown.

5.1. SPECIFICATIONS AND DESIGN CONSIDERATIONS

As stated in Chapter 3, an alternative technique for efficient bioimpedance measurement has been introduced [5.1]. This technique is based on the detection of the magnitude and phase of an unknown impedance. In particular, the extraction of the parameters of the polar representation of a complex magnitude is developed by means of a gain and phase detector. A GPD circuit processes the outputs from two amplifiers to provide ratiometric gain measurement, typically obtained by logarithmic conversions, and phase difference between the referred signals.

In the most commonly used technique for phase detection, the phase difference between two signals having the same frequency –one of which acts as a reference signal– is computed by first converting the signals into respective square waves by means of zero-crossing detection and then measuring the time difference between the pulse edges or centers of the two square waveforms [5.2]. This time difference can be measured as a time interval, either individually or as an averaged on a predetermined number of input signal periods, and can be transformed into an analog quantity.

To implement the method practically, the two analog input signals must first be converted to digital signals having constant amplitude. This can be done with a Schmitt trigger, along with an *RC* stabilizing network at its output. The relative phase of the obtained square waves is translated to a DC voltage by a set-reset (SR) flip-flop and a cascaded averaging filter. In practice, high-accuracy phase estimation requires the switching of the two digitized signals between the high and the low state to be very sharp. This requirement imposes the use of several stages to amplify and clip the analog signals preceding the Schmitt trigger. One of the simplest realizations of a limiter circuit consists in using an operational amplifier in inverting configuration and a pair of Zener diodes in its feedback path. Unfortunately, the non-ideal characteristics of the Zener diodes can wreck circuit accuracy.

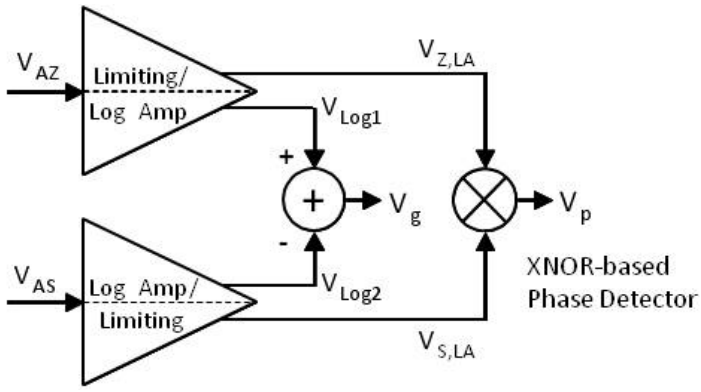

Figure 5.1. Block diagram of the proposed gain-phase detector.

In particular, for reverse voltages below the Zener voltage, a small current leaks through the diode and, hence, the gain of the operational amplifier is modified. In addition, as a consequence of the large breakdown voltage in standard Zener diodes, which is greater than approximately five volts, these components find better application in high-voltage circuits.

Since low power consumption is one of the objectives for the application, Zener diodes should be avoided. Furthermore, classical Schmitt trigger suffers from an amplitude-dependent phase shift caused by fixed hysteresis, which introduces a larger error in phase measurement when the amplitudes of the input signals are not equal (as it usually occurs).

Figure 5.1 shows the architecture of a compact GPD, which circumvents the above mentioned drawbacks with a cost-effective design. In particular, the GPD block consists of two matched limiting/logarithmic amplifiers, an XOR-based phase detector, and a subtracting circuit [5.3]. The two signals V_{AZ} and V_{AS} at the input of the GPD are two amplified voltage signals delivered by two (ideally) identical instrumentation amplifiers (not shown in Fig. 5.1). Each LLA provides two voltage outputs, namely, a squared-limited output V_{LA}, which is a saturated signal over most of the input dynamic range,

and a pseudo-logarithmic output, V_{Log}, which represents a logarithmic conversion of the input voltage. The two saturated signals are applied to the phase detector, which therefore provides the required phase difference information. The two pseudo-logarithmic signals feed the subtractor, which thus yields the magnitude ratio between the two input signals, V_g (in a logarithmic scale). This circuitry is suited to evaluate the magnitude and the phase of an unknown impedance, as is required in bioelectrical impedance analysis.

The main block in the GPD structure is the limiting/logarithmic amplifier. The essential purpose of a logarithmic amplifier (*logamp*) is to compress a signal with a wide dynamic range into its decibel equivalent. In the usual case where all variables are voltages, the relationship between the input, V_{in}, and the output variable, V_{Log}, can be expressed as

$$V_{Log} = V_{SLP} \cdot \log\left(V_{in}/V_{Null}\right) \tag{5.1}$$

where V_{SLP} is a coefficient which represents the slope expressed in volt/decade and V_{Null} is the value of the input voltage which makes $V_{Log} = 0$, and is referred to as the intercept voltage.

Several approaches for implementing a *logamp* have been proposed [5.4-5.11]. On the basis of the circuit technique and architecture used, they may be divided into two types: a) methods that employ the logarithmic current-to-voltage characteristic of semiconductor devices such as *p-n* junction diodes [5.4], light emitting diodes [5.5], photo diodes [5.6], bipolar transistors [5.7], GaAs MESFETs [5.8], and MOS transistors in the subthreshold region [5.9, 5.10], and b) methods which rely on the circuit architecture to produce a pseudo-logarithmic transfer function based on a piecewise linear approximation [5.11].

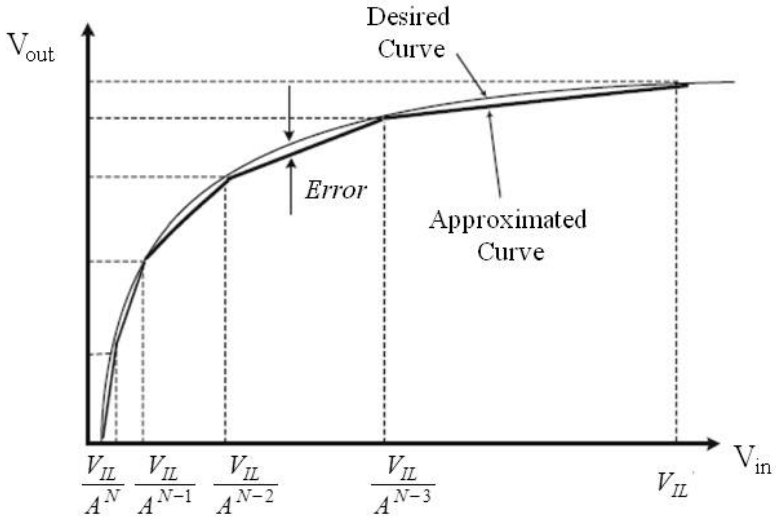

Figure 5.2. Pseudo-logarithmic curve piecewise approximation.

The former solutions use the exponential current-to-voltage (*I*-to-*V*) characteristics of non-linear devices, almost always diodes or bipolar junction transistors (BJT), placed in the feedback path of an operational amplifier to generate a logarithmic *I*-to-*V* relationship. However, the operation this approach degrades at high frequency because of the modification of the basic *V*-to-*I* characteristic law caused by the parasitic elements [5.12]. In addition, unfortunately, reliable BJTs cannot be implemented in standard CMOS-only processes. A subthreshold MOSFET can also be used in the feedback path instead of a BJT in order to realize logarithmic amplification, but it cannot be used at the frequencies required in wideband bioimpedance measurements due to its limited current capability.

A more successful approach in CMOS technology is the piecewise linear approximation of the logarithm function. The piecewise linear approximation architecture consists of the cascade of nonlinear gain stages approximating the logarithmic curve as a piecewise linear function. The approximated curve is

constructed from a series of linear pieces of varying length and slope as illustrated in Fig. 5.2. A pseudo-logarithmic transfer curve is defined as an approximation of an ideal logarithmic curve. This definition implies that the pseudo-logarithmic curve must approach a true logarithmic curve as a limit. Obviously, this approximation has an inherent error that depends on the number of linear pieces and on design parameters – e.g., the small-signal gain of each stage– that strongly affect the practical implementation of the stages.

The true piecewise approximation logarithmic amplifiers are divided into two main classes: series linear limit logarithmic amplifiers and parallel-summation logarithmic amplifiers. Although these two types of amplifiers have different block diagrams, they have similar basics of operation, and basically differ in the small-signal transfer function of the gain cell, usually known as $A/1$ and $A/0$ gain cell, respectively (Fig. 5.3). However, in series linear limit logarithmic amplifiers, the challenges in the realization of the $A/1$ characteristics limit the obtainable dynamic range. In addition, the gain cell in the series limit type has a difficult and complicated circuit design. More specifically, this amplifier needs a high number of transistors with large aspect ratios in the unity-gain circuit along with a large bias current and, consequently, more power to operate. This excess area and power consumption involves all the stages and produces large silicon area occupation and power dissipation [5.13].

In contrast, the parallel summation type has a simple circuit implementation and consumes less area and power. Moreover, the $A/0$ characteristic is easier to be realized. Another preference in the $A/0$ realization is that voltages are converted to currents to be summed. So, more stages can be cascaded and a large dynamic range can be achieved. However, considerations regarding the bandwidth and the power that the parallel summation structure features must be taken into account. The large number of stages causes bandwidth limitation because of the large parasitic capacitors in the summing circuit. Hence, the overall amplifier structure allows the increase of the number of

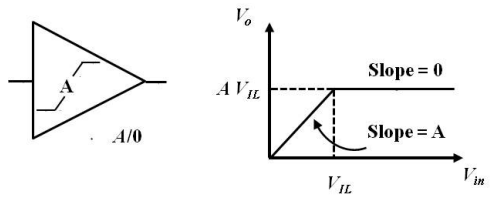

(a)

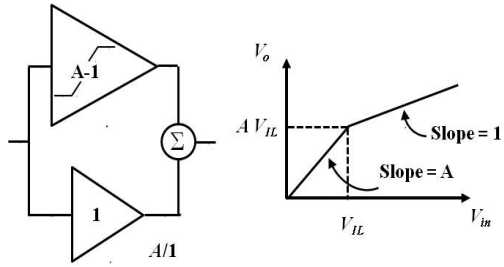

(b)

Figure 5.3. a) $A/0$ stage and its transfer function and b) $A/1$ stage and its transfer function.

stages at the expense of a lower bandwidth and a higher power consumption. Therefore, the parallel summation logarithmic amplifier has advantages over the series linear limit type in dynamic range, silicon area, and power consumption and, accordingly, is a better choice in logarithmic amplifier designs for power- and cost-effective bioimpedance circuitry.

Figure 5.4 (a) corresponds to a block diagram of the parallel-summation logarithmic amplifier (PSLA), which also provides a squared-limited output V_{LA}. The individual gain cells (assumed to be identical) of a PSLA have the ideal transfer characteristic illustrated in Fig. 5.3 (a). The small-signal gain of each stage is equal to A_0 for input levels up to the knee voltage V_{IL}, above which it falls to zero. For small input voltages, the cascade of the gain cells will simply provide amplification by $(A_0)^N$, where N is the number of stages. However, as the input voltage increases, a value $V_{in} = V_{OL}/A_0^N$ will be

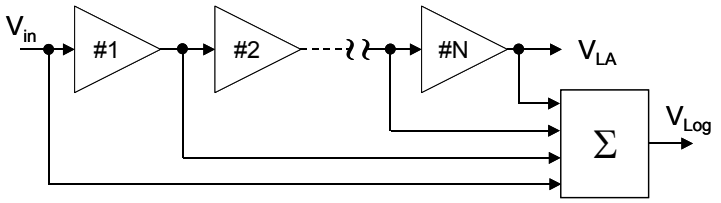

(a)

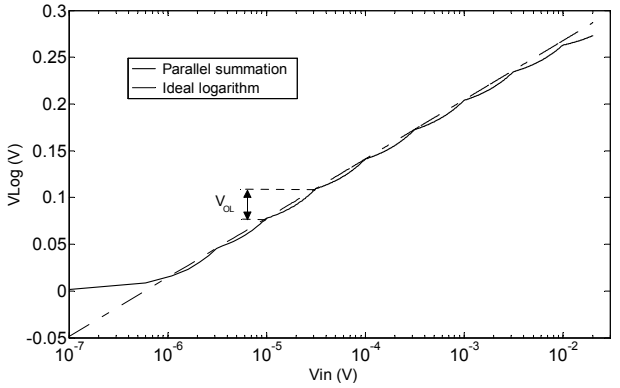

(b)

Figure 5.4. a) Block diagram of the parallel-summation limiting/logarithmic amplifier and b) Pseudo-logarithmic response in semilogarithmic plot (x axis: logarithmic scale; y axis: linear scale) (N = 8, A_0 = 8 dB, V_{IL} = 10 mV).

reached at which the last cell ceases to amplify and provides a constant output voltage V_{OL}. As the input signal becomes progressively larger, the output voltages of the gain cells will successively reach their upper bound, starting with the second-last stage and proceeding backwards toward the first one. Notice that, during normal operation, the last stages in the limiting amplifier tend to work in a large-signal regime, i.e., their output voltage is either at the high or at the low level during most of the time, and switches from one level to the other during transients, and, consequently, the large-signal parameters of the gain cell, V_{IL} and V_{OL}, will determine the limiting amplifier behavior. When the input voltage becomes equal to V_{IL}, the output voltage of the first

stage becomes equal to V_{OL}. The overall response of the *logamp*, which is obtained by summing the output voltages of all stages, approximates a straight line when drawn on a semi-logarithmic plot [Fig. 5.4 (b)].

In order to obtain a mathematical model of the parallel-summation *logamp* that can be employed to develop a design flow for a GPD, let us assume that the output voltage limitation comes from the m-th stage ($1 \leq m \leq N$). Under limiting conditions, the output voltage of the m-th stage is equal to V_{OL}. This signal passes through $N - m$ further stages, each working in limiting conditions, before reaching the output node. The input of the m-th stage, $V_{in,m}$, at the beginning of the limitation region has been amplified linearly by the $m - 1$ preceding stages and, hence, the output voltage of the *logamp* can be expressed as follows:

$$V_{Log} = V_{OL} + (N - m)V_{OL} + V_{OL}\cdot(1/A_0 - 1) \tag{5.2}$$

Since $V_{in,m} = V_{OL}/A_0 = V_{in}\cdot(A_0)^{m-1}$, it can be easily derived that the following expression holds for the desired logarithmic characteristic:

$$V_{Log} = V_{OL}\cdot\left[N + \left(\frac{1}{A_0 - 1}\right)\right] + \frac{V_{OL}}{\log A_0}\cdot\log\left(\frac{V_{in}}{V_{IL}}\right) \tag{5.3}$$

By comparing Eq. (5.1) and Eq. (5.3), it can be readily shown that the intercept voltage and the voltage slope are given, respectively, by

$$V_Z = V_{IL}\cdot A_0^{-\left[N + \frac{1}{A_0 - 1}\right]} \tag{5.4}$$

$$V_{SLP} = V_{OL}\cdot(\log A_0)^{-1} \tag{5.5}$$

Figure 5.4 (b) illustrates the transfer characteristic of the proposed *logamp* when N = 8, A_0 = 10 dB, and V_{IL} = 10 mV. Each time a gain stage reaches its upper bound, the output voltage turns out to be increased by an amount V_{OL} with respect to the value reached when the successive stage entered saturation. Notice that the pseudo-logarithmic curve does not approach the ideal logarithmic curve when the input signal exceeds the ideal value of input dynamic range, DR_{in}.

The logarithmic function is provided when the PSLA is in large-signal operation, namely, for input voltage levels ranging from V_{OL}/A_0^N (when the last stage begins to saturate) to V_{OL}/A_0 (until the first stage leaves its linear region) [5.14]. The input dynamic range DR_{in} of the PSLA is therefore equal to $(A_0)^{N-1}$. Hence, the required overall small-signal gain A_T of the limiting amplifier for a required input dynamic range and the resulting minimum value of N can be expressed, respectively, as

$$A_T = A_0 + DR_{in} \tag{5.6}$$

$$N_{\min} = 1 + DR_{in} / A_0 \tag{5.7}$$

where A_T, A_0, and DR_{in} are expressed in dB.

Following the analysis by Huang *et al*. [5.15], the optimal value of A_0 or, conversely, the optimal number of stages of the limiting amplifier required to maximize accuracy for a given value of A_T can be determined. The small-signal gain A_0 is chosen as a trade-off between the need for achieving high logarithmic response accuracy, which is inversely proportional to A_0, and the need to ensure low power dissipation, which implies using the minimum number of stages required to cover the specified input dynamic range. In Fig. 5.5, the maximum error of the PSLA response with respect to an ideal logarithmic curve is plotted versus N for two different values of A_T. A higher number of stages involves a lower small-signal gain per stage to obtain

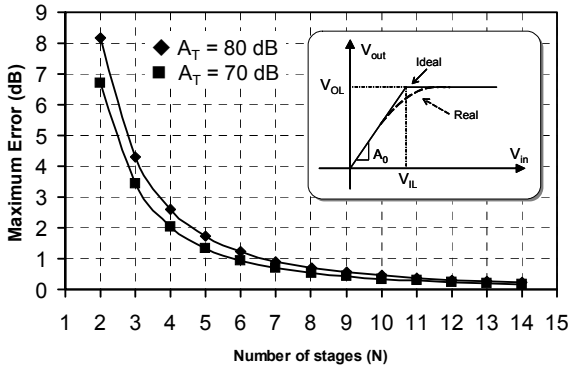

Figure 5.5. Error of a PSLA as a function of the number of stages for different values of the overall small-signal gain AT. The inset shows the transfer function of one gain cell [as from Fig. 5.3 (a)].

the required value of A_T for the whole structure and, consequently, results in higher accuracy. However, as can be observed, an increase in the number of stages only leads to a small accuracy improvement for relatively high values of N. This means that we cannot increase the accuracy of the PSLA above a given limit in the presence of a limited power consumption budget. It is easily deduced from Fig. 5.5 that, for eight stages with A_0 = 9.3 dB in the limiting amplifier, i.e., A_T = 74.5 dB, which is consistent for achieving the 65-dB input dynamic range required of the target application, the relative error is smaller than ±1 dB. This relative error value of is satisfactory for our application.

Assuming a limiting amplifier with N identical gain stages that require an overall small signal gain A_T and a bandwidth f_T, the normalized gain A_0 and the bandwidth f_s of each gain stage can be derived as indicated by R.P. Jindal [5.16]. In particular, the value of the gain-bandwidth product per stage, GBW_s, required to achieve a predetermined bandwidth f_T of the overall limiting amplifier is equal to:

$$GBW_s = \frac{f_T}{\sqrt{2^{1/N} - 1}} \cdot A_T^{1/N} \tag{5.8}$$

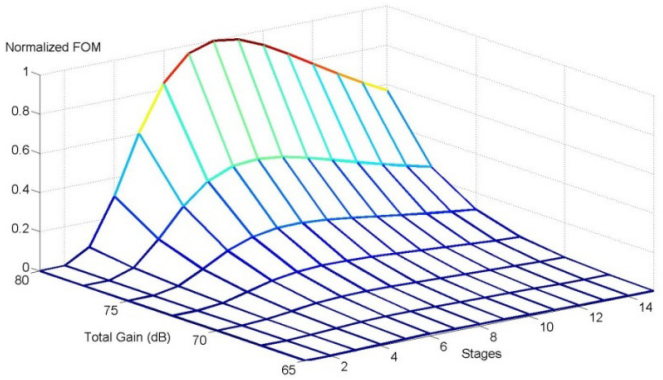

Figure 5.6. FOM of the limiting/logarithmic amplifier. The FOM value is normalized with respect to its maximum value.

As pointed out by the above equation, the higher the overall small-signal gain, the higher the gain-bandwidth product per stage with the same pole frequency. However, there is a trade-off between the number of stages and power consumption. Indeed, the total power increases linearly with the number of stages. In this respect, it should be pointed out that more than one half the total power consumption of a wideband high dynamic range logarithmic amplifier is due to the limiting amplifier. In order to obtain the optimal number of stages, we define a figure of merit, *FOM*, which will be useful for comparing the performance of different schemes. This *FOM* takes the gain-bandwidth product, GBW_T, the maximum error, *Error*, the occupied area, *Area*, and the power consumption, P_T,of the overall amplifier into account:

$$FOM = \frac{GBW_T}{Error \cdot P_T \cdot Area} \tag{5.9}$$

The proposed *FOM* assumes that each gain cell is a one-pole system implemented by a single-stage with a folded-diode load and that the power consumption can be described as $P_T \propto N \cdot (GBW_s)^2$. The normalized *FOM* is plotted in Fig. 5.6 as a function

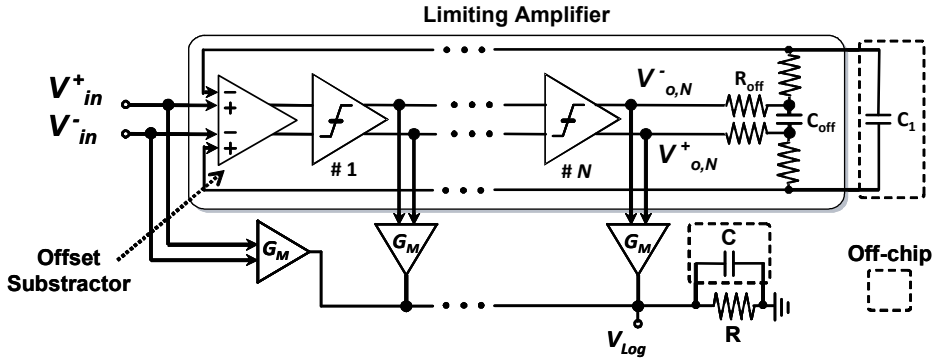

Figure 5.7. Architecture of a parallel-summation logarithmic amplifier. The block diagram of the limiting amplifier with offset cancellation is included.

of the number of stages and the overall small-signal voltage gain.

Figure 5.7 shows the architecture of the proposed PSLA. The gain cells of the limiting/logarithmic amplifier are implemented by voltage-limited differential stages, each having an associated magnitude detector G_M that converts the differential output voltage of the gain stage into a current. The generated currents are then summed into an on-chip passive resistor R, thus obtaining the (pseudo-)logarithmic output voltage, V_{Log}. The magnitude detectors were designed as full-wave rectifiers and hence, an off-chip capacitor C was included in parallel with the on-chip resistor R to filter out the AC components in V_{Log}.

It is straightforward from Fig. 5.7 that the proposed structure of limiting/logarithmic amplifier, which comprise the core of the GPD block, provide convenient and compact architecture to take advantage of obtaining simultaneously the gain (logarithmic output) and phase (square-limited output) information from an input signals, which are especially useful for ratriometric and phase difference measurement between two signals. In addition, two limiting/logarithmic amplifiers and other circuitry which are co-integrated on a single substrate provide a high degree of matching between the amplifiers, thereby cancelling errors in the individual frequency

responses of the individual amplifiers, extending the usable frequency response, and improving effective noise figure.

Due to the large differential gain usually required in limiting amplifiers, even a very small input-referred offset voltage will be able to saturate the output node or even internal nodes of the gain chain, thus restricting the input sensitivity of the limiting amplifier. The input dynamic range of the PSLA will therefore be reduced. To avoid this risk, an offset cancellation scheme must be adopted.

Figure 5.7 shows the feedback-type offset cancellation mechanism incorporated into the proposed design. A second-order low-pass transfer function filters the output voltage-limited signal and extracts the DC offset voltage, which is then subtracted from the input signal. This way, the input-referred offset voltage of the limiting amplifier is reduced by the closed-loop feedback network. The offset subtractor included in the signal path has been implemented as a differential difference amplifier with unity gain. Two input terminals of this block are used for the differential input signal, whereas the other two input terminals are used to feed back the measured offset voltage. The subtractor introduces insignificant amount of parasitic effects, which does not degrade overall operation.

Equations (5.6) and (5.7) can be employed to develop a design flow for limiting amplifiers used in PSLAs. However, these simple expressions do not predict the impact of the real operation of MOS transistors or the effect of process variability and device mismatches on the overall performance of the designed amplifiers. Moreover, technology scaling leads to significant variations in transistor parameters such as transconductance and output conductance, which are therefore affected by statistical variability. Since the individual gain stages in a PSLA must be well matched to one another in order for the amplifier to operate properly over a large dynamic range and a wide bandwidth, some extra compensation circuitry is required. Most of the limiting amplifiers reported in the literature are intended for applications such as radar receivers,

receiving signal strength indicators in wireless transceivers [5.15], [5.17], or optical receiver analog front-ends [5.18]. The above circuit solutions are relatively complex and therefore are not adequate for the requirements of a wearable device. A simple gain-cell structure having a transfer characteristic (and, hence, small- and large-signal responses) insensitive to unavoidable process variations has to be employed, so as to allow the optimal design of low-power biomedical limiting amplifiers.

5.2. CIRCUIT DESIGN AND IMPLEMENTATION

The elementary gain stage in the limiting amplifier has been usually implemented by using unbalanced differential pairs [5.19] or specially biased input pairs [5.15], since these topologies are well-suited for high-speed operation. However, the transfer function of these stages is strongly affected by fluctuations of device parameters due to fabrication process spreads. As a high small-signal gain single-cell is not required in our application, a simple fully differential structure including only low-impedance nodes can be used. This choice allows high operation speed to be easily achieved and eliminates the need for any common-mode feedback (CMFB) circuit to control the output common-mode voltage, with advantages in terms of power consumption and occupied silicon area. In addition, the problems associated with the sensitivity of CMFB circuits to device mismatches and process spreads are avoided, thus leading to a compact and efficient design.

For implementing a CMOS limiting amplifier, the designer has the freedom to choose among a number of gain cell topologies. However, most of these structures either show severe performance degradation in the presence of device mismatches or are not functional at all for low-voltage and low-power operations. On the other hand, a key point for the gain cell that facilitates the cascade connection of several stages consists in setting the input and output common-mode voltages to the same value. On the other hand, setting the output common-mode DC voltage, V_{o_dc}, in the mid-supply voltage range V_{DD} will facilitate the design of the magnitude detector G_M. As mentioned above, in our design the magnitude detector has been implemented with a current rectifier: this rectifier is driven by a pair of transconductor stages that convert the differential output voltages of the gain stages into currents [5.20], as shown below in detail.

Figure 5.8 shows four conventional cells providing a moderate gain. Among these cells, the most basic one consists of a resistor-loaded differential pair, Fig. 5.8 (a). This

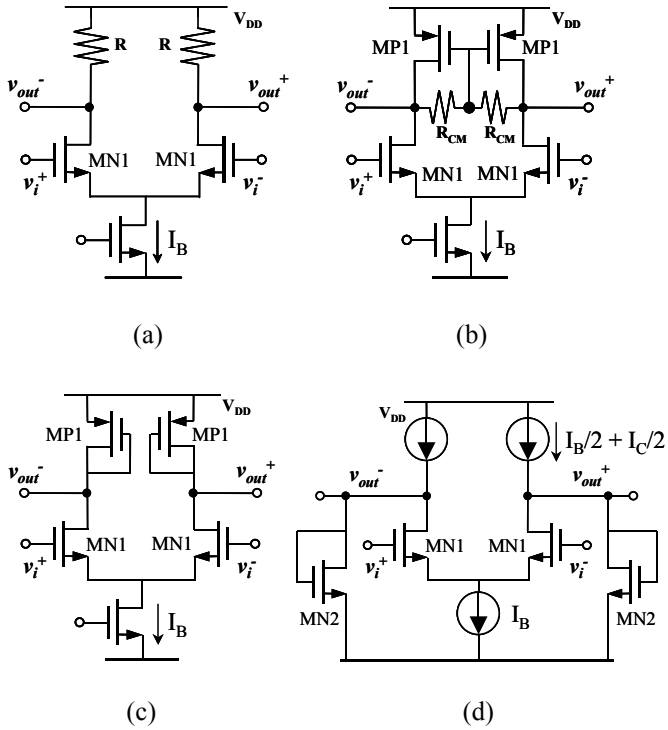

Figure 5.8. Gain stage configurations: a) Resistor-loaded differential pair; b) Differential pair with current-source load; c) Differential pair with diode-connected load and d) Differential pair with diode-connected load transistors folded to ground.

cell has the advantage of simplicity and therefore, features high speed at low-power operation [5.18]. The small-signal gain $A_0 = \left(v_{out}^{+} - v_{out}^{-}\right) \Big/ \left(v_i^{+} - v_i^{-}\right)$ is equal to $g_{m,N1} \cdot R$, where $g_{m,N1}$ denotes the transconductance of input drivers transistors and R is the value of load resistors. The DC output voltage V_{out_dc} is equal to $V_{DD} - R \cdot I_B/2$. To ensure that V_{o_dc} is set to $V_{DD}/2$, R must be chosen equal V_{DD}/I_B and, hence, the transconductance $g_{m,N1}$ should be set to

$$g_{m,N1} = \sqrt{k'_{N1} I_B (W/L)} = A_0 / R = A_0 \cdot \left(I_B / V_{DD}\right) \tag{5.10}$$

where all the symbols have their usual meaning.

According to Eq. (5.10), the required overdrive voltage of devices MN1 (V_{ov} = $2I_{drain}/g_m = I_B/g_{m,N1}$) turns out to be equal to V_{DD}/A_0. Therefore, V_{ov} has a large value in the presence of low values of A_0, which implies that the aspect ratio W/L of transistors MN1 must be chosen small. To ensure saturated operation of the transistor implementing the tail current generator, the biasing current I_B must be increased under very low-voltage supplies, i.e., $V_{DD} \leq 2$ V, thereby increasing power consumption.

In order to alleviate the above power demand, the drain load of the differential pair can be implemented by PMOS current sources, thus obtaining the gain cell shown in Fig. 5.8 (b). Resistors R_{CM} sense the output common-mode voltage and drive the active load. This way, transistors MP1 and resistors R_{CM} form a local common-mode feedback loop, which suppresses the common-mode gain, and load devices appear as diode-connected for common-mode signals [5.21]. The small-signal differential gain of this cell is

$$A_0 = g_{m,N1} \cdot (R_{CM} \,||\, r_{o,N} \,||\, r_{o,P}) = g_{m,N1} \cdot R_{out} \tag{5.11}$$

where $R_{out} = R_{CM} \,||\, r_{o,N} \,||\, r_{o,P}$ is the impedance at the output nodes and $r_{o,N}$ ($r_{o,P}$) denotes the drain-to-source resistance of transistors MN1 (MP1). To provide a high enough differential gain, R_{CM} must be sufficiently large. However, large resistors R_{CM} add parasitic poles to the output nodes, thus lowering the bandwidth.

Figure 5.8 (c) shows a differential pair with diode-connected loads [5.22]. The total resistance seen at the output nodes is equal to $(1/g_{m,P1})||r_{o,N}||r_{o,P}$ where $g_{m,P1}$ is the transconductance of MP1. The small-signal gain is equal to

$$A_0 = \frac{g_{m,N1}}{\left(g_{m,P1}^{-1} \,||\, r_{o,N} \,||\, r_{o,P}\right)^{-1}} \approx \frac{g_{m,N1}}{g_{m,P1}} \approx \frac{\sqrt{\mu_{N1} \cdot (W/L)_{N1}}}{\sqrt{\mu_{P1} \cdot (W/L)_{P1}}} \tag{5.12}$$

According to Eq. (5.12), A_0 is independent of the bias currents of the transistors but depends on carrier mobility. Therefore, the small-signal gain and the knee voltage V_{IL} of the cell fluctuate undesirably with process variations, [as in the case of the stages in Figs. 5.8 (a) and 5.8 (b)], with the ensuing penalty of a reduced overall small-signal gain A_T under worst-case conditions. It should be pointed out that diode-connected loads consume a voltage headroom that depend on their size and their bias current, thus leading to the need for a tradeoff between the DC output common-mode voltage and A_0 as in the case of the stages in Fig. 5.8 (a). This trade-off can be avoided by using the gain cell shown in Fig. 5.8 (d). Diode-connected transistors are folded to ground to reduce supply voltage requirements [5.15], [5.23]. The small-signal gain of this cell can be expressed as

$$A_0 = \frac{g_{m,N1}}{\left(g_{m,N2}^{-1} \,||\, r_{o,N} \,||\, r_{o,P}\right)^{-1}} \approx \frac{g_{m,N1}}{g_{m,N2}} \approx \frac{\sqrt{(W/L)_{N1} \cdot I_B}}{\sqrt{(W/L)_{N2} \cdot I_C}} \tag{5.13}$$

where I_C is twice the current flowing through each transistor MN2 and $r_{o,N}$ and $r_{o,P}$ denote the combination of the drain-to-source resistance of transistors MN1 and MN2 and the output resistance of the current sources $I_B/2 + I_C/2$, respectively. Since A_0 is independent of carrier mobility, the sensitivity to process variations is reduced. To improve the gain accuracy of the circuit in Fig. 5.8 (d), PMOS transistors implementing current sources $I = I_B/2+I_C/2$ should be operated in strong inversion by choosing a bias point with a large overdrive voltage and, hence, a small value of $g_{m,P1}/I$ [5.24], where $g_{m,P1}$ is the transconductance of these PMOS devices. However, due to supply voltage constraints and DC output common-mode voltage requirements, i.e., $V_{o\_dc} = V_{DD}/2$, PMOS transistors cannot be biased at high overdrive voltage levels. This leads to a significant contribution from the current factor mismatch error $\Delta\beta$ ($\beta = \mu \cdot C_{OX} \cdot W/L$ with usual meaning of symbols), which is inversely proportional to ($g_{m,P1}/I$), thus reducing

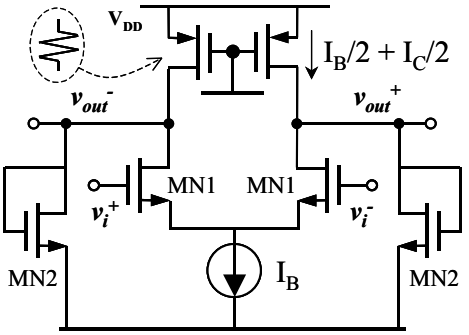

Figure 5.9. Circuit schematic of the proposed gain stage.

gain accuracy performance.

Figure 5.9 illustrates the proposed gain stage, which combines the advantages of low mismatch sensitivity, low power consumption, and low-voltage operation in a single topology. PMOS current sources in the scheme of Fig. 5.8 (d) were replaced by resistors implemented with PMOS devices operating in their triode region. In addition, for reducing the $\Delta\beta$ sensitivity of the gain cell, these resistors allow setting $I_B/2 = I_C/2$. Hence, the small-signal gain A_0 of the selected topology is given by the expression

$$A_0 = \frac{\sqrt{(W/L)_{N1}}}{\sqrt{(W/L)_{N2}}} \tag{5.14}$$

Equation (5.14) shows that A_0 is independent of the bias currents of the differential pair transistors and is therefore substantially insensitive to process and temperature fluctuations. The differential pair is biased with a low overdrive voltage, in order to obtain a moderate value of ratio $g_{m,N1}/I_B$ and reduce the threshold voltage sensitivity of V_{IL}**.** Consequently, these biasing conditions ensure moderate variations of the knee voltage V_{IL}, which is directly proportional to the threshold voltage, V_{TH}, of the NMOS devices in the differential pair.

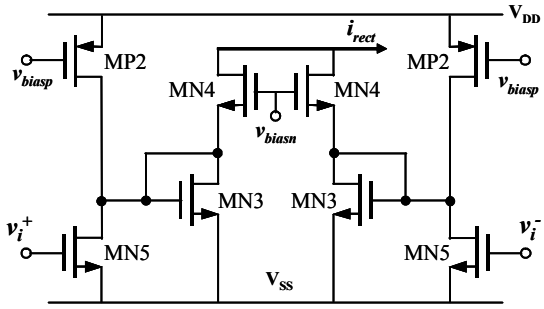

Figure 5.10. Circuit schematic of the full-wave rectifier.

The designed low-voltage full-wave rectifier (FWR) is shown in Fig. 5.10. Devices MN5 and MP2 form transconductance stages that convert the differential input voltages into currents. Each of the two branches made up by transistors MN3 and MN4 operates as a current-mode half-wave rectifier. The two branches are automatically turned on alternatively in each half period. As the output currents of the two branches are summed, a full-wave rectified current, i_{rect}, is obtained at the output. This rectified current is fed to an on-chip first-order low-pass filter in order to convert the summed current to a voltage and simultaneously extract the DC value. The described rectifier scheme features high accuracy while drawing a low DC current.

A block diagram of the designed phase-extractor circuit is depicted in Fig. 5.11. Basically, it consists of three exclusive-or (XOR) gates, two D-type flip-flops with reset capability, and a pair of voltage-driven analog switches. $V_{Z,LA}$ and $V_{S,LA}$ are the square-limited output signals obtained from the limiting/logarithmic amplifiers, which contain the information of the phase between the input voltage signals V_{AZ} and V_{AS} (Fig. 5.1). The digital circuitry in the scheme of Fig. 5.11 compensates for any offset errors that may be introduced by the limiting amplifiers [5.25] and provides an analog output representation of the phase difference between signals $V_{Z,LA}$ and $V_{S,LA}$. More specifically, a pulse train whose average value is proportional to this phase difference is obtained at the output node (node labeled as 1 in Fig. 5.11).

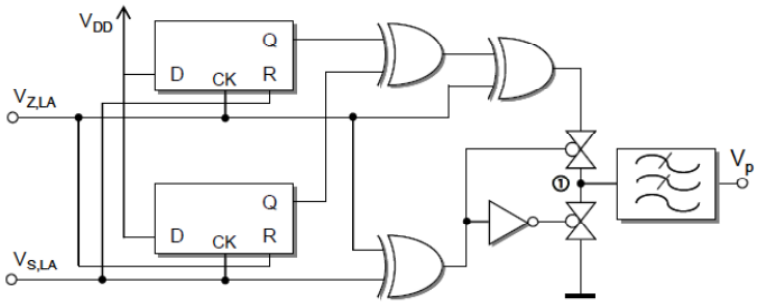

Figure 5.11. Circuit schematic of the designed phase-detector.

Classical phase extractor circuits, such as an XOR gate or two edge-triggered flip-flops, introduce errors when the input waveforms $V_{Z,LA}$ and $V_{S,LA}$ are distorted by offset voltages introduced by preceding analog stages, since the digital waveforms will change state either slightly before or slightly after (depending on the polarity of the offset error) the instant when the associated input signal crosses is zero value. This leads to a timing error in the digital waveforms and, hence, results in a loss of accuracy in the measurement. As mentioned above, the output of the designed phase extractor consists of a pulse-width modulated waveform of varying duty cycle, whose average duty cycle represents the phase difference of the digital signals. The value of the average duty cycle is then obtained by extracting the DC component of the pulse train waveform by means of a low-pass filter, according to the expression:

$$\theta = \frac{180°}{V_{DD}} \cdot V_p \tag{5.15}$$

5.3. POST-LAYOUT AND EXPERIMENTAL RESULTS

The proposed gain and phase detector was designed and fabricated in 0.35-μm double-poly, triple-metal CMOS technology as a component of a gain and phase detector. The microphotograph of the limiting/logarithmic amplifier included in this GPD is illustrated in Fig. 5.12. A full LLA occupies 150 μm x 300 μm, without pads, whereas the active area of the limiting amplifier is only 0.006 mm^2.

The input sensitivity of the limiting amplifier results from the input-referred noise and the output DC offset voltage [5.18]. However, since the proposed amplifier includes an offset cancellation loop, we can assume that the random noise is the dominant factor that limits amplifier sensitivity. The simulated input referred noise of the limiting amplifier was about 0.2 μV_{rms}. Post-layout simulations using Cadence Spectre were also carried out to evaluate the performance of the designed gain cell. Figure 5.13 illustrates Monte Carlo (MC) histograms of small-signal gain A_0, limited output voltage V_{OL}, and DC output common-mode voltage V_{o_dc} for a single gain cell (supply voltage V_{DD} was set to 2 V).

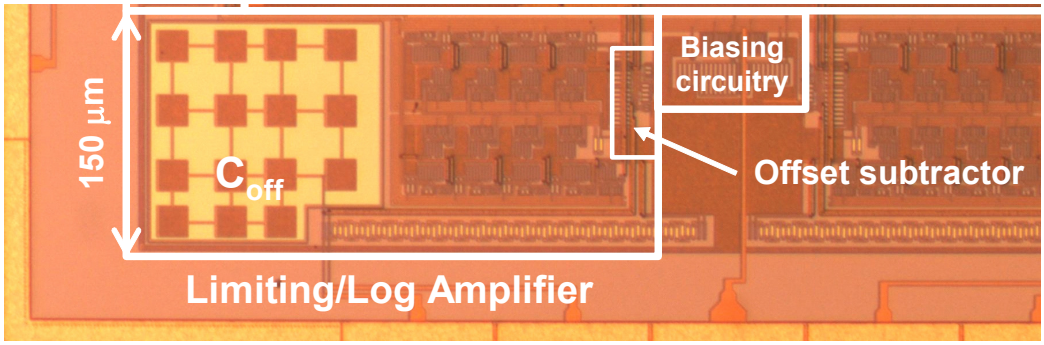

Figure 5.12. Detail of the fabricated chip microphotograph showing one limiting/logarithmic amplifier as a part of a gain-phase detector.

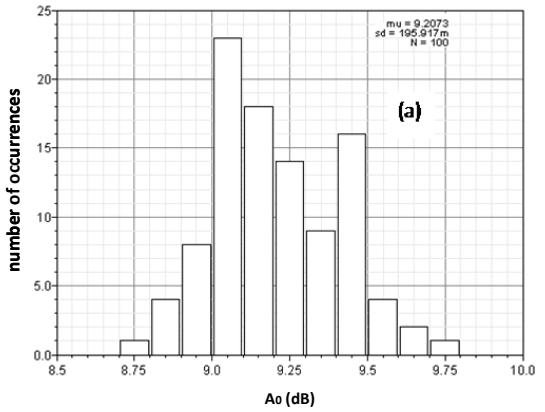

(a)

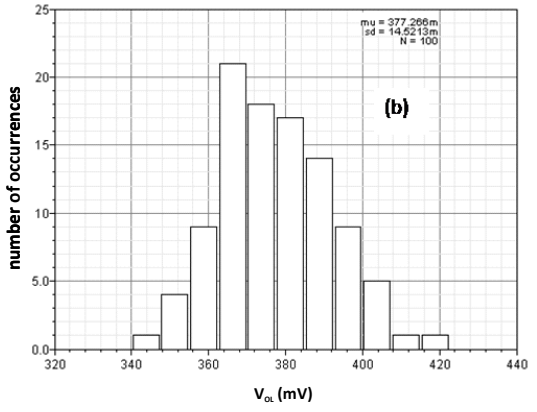

(b)

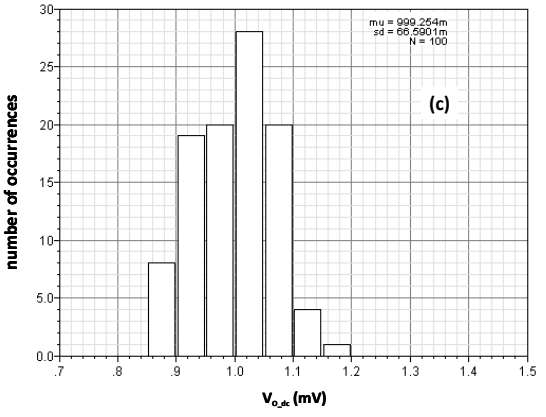

(c)

Figure 5.13. Monte Carlo histograms of: a) Small-signal gain A_0; b) Limited output voltage V_{OL} and c) DC output common-mode voltage V_{o_dc} for a single gain cell (V_{DD} = 2 V).

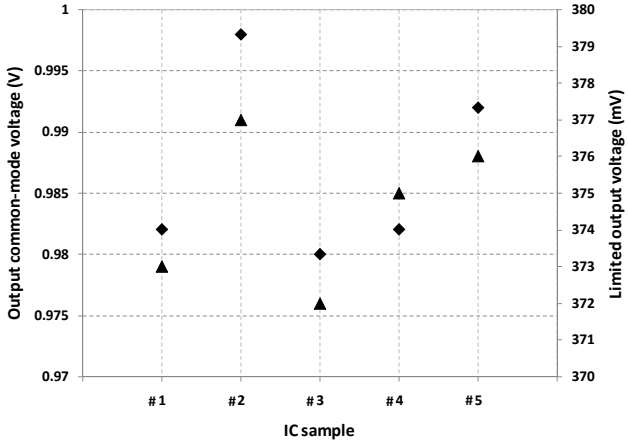

Figure 5.14. a) Measured output common-mode DC voltage of the limiting amplifier (◆) for five IC samples ($v_{in}^{+} = v_{in}^{-} = 1$ V) and b) Measured amplitude for voltage-limited output signal $V_{o,N}$ (▲) of the limiting amplifier.

Device mismatches and process spreads were taken into account during MC simulations. According to Fig. 5.13 (a), the small-signal gain of the cell shows a ±0.2-dB standard deviation around the mean value of 9.2 dB. Consequently, the standard deviation of the small-signal gain of the limiting amplifier (8-stage chain) is only ±1.6 dB. Figure 5.13 (b) reveals that the predicted standard deviation of voltage V_{OL} around the mean value of 377 mV is only about ± 15 mV, whereas Fig. 5.13 (c) predicts a standard deviation of 67 mV around a mean value of 999 mV for V_{o_dc}.

The performance of the fabricated test chip was then experimentally evaluated. Supply voltage V_{DD} was set to 2 V in all measurements. The overall power consumption of the limiting amplifier, including the biasing circuitry, is equal to 620 μW. This experimental result is in good agreement with the simulated power consumption of a gain cell and the subtractor circuit, which were 60 μW and 80 μW, respectively (560 μW plus the power due to the bias circuitry). The above overall value of power consumption is very low for medical applications of bioimpedance analysis over a frequency interval from 1 kHz to 1 MHz.

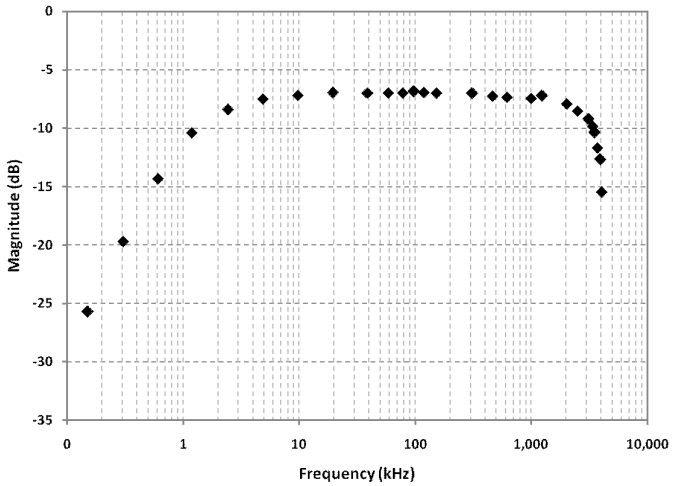

Figure 5.15. Measured small-signal frequency response of the limiting amplifier for a -80 dBm sinewave input signal.

Monte Carlo simulations also demonstrated that the designed gain cell is not very sensitive to process spreads and mismatches. This has been experimentally verified by measuring the DC behavior of the limiting amplifier. Figure 5.14 shows the measured output common-mode DC voltage, V_{o_dc}, and the measured amplitude, V_{OL}, of the voltage-limited output signal of the limiting amplifier for five IC samples. The mean values of V_{o_dc} and V_{OL} of the limiting amplifier are about 0.99 V and 374 mV, respectively. These results are in excellent agreement with the above MC simulations and illustrate that the overall amplifier and a single cell have the same values for V_{o_dc} and V_{OL}.

Although the behavior of limiting amplifier is nonlinear, its small-signal frequency response can be measured by applying a sufficiently small signal to its input, so that all gain stages operate in their linear range. Figure 5.15 illustrates the experimental frequency response of the limiting amplifier for a −80 dBm sinewave input signal. It is worth to point out that the measured frequency response at high frequencies is limited by the instrumentation amplifier that feeds the input signals (V_{AS} or V_{AZ} in Fig. 5.1) to

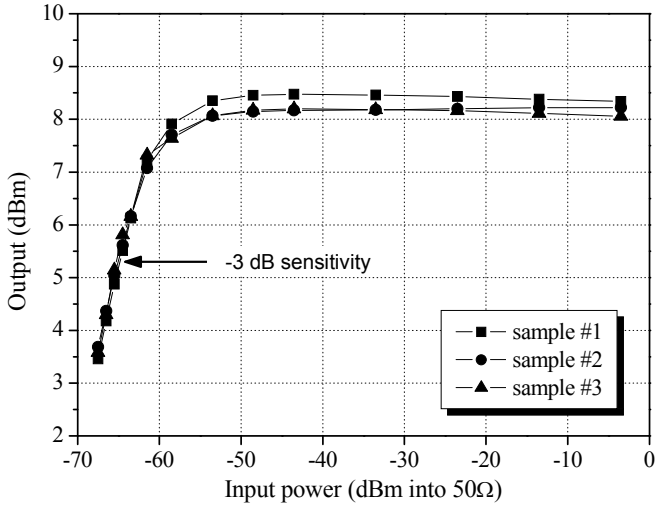

Figure 5.16. Measured input sensitivity of the limiting amplifier for three IC samples.

the limiting/logarithmnic amplifier and the on-chip buffer that drives the output voltage of the limiting amplifier onto the output pad (see Fig. 5.12). Accordingly, the measured –3dB bandwidth, considering the effect of the instrumentation amplifier and buffer circuit, turned out to be about 3.8 MHz. The bandwidth of the limiting amplifier was set to 20 MHz in the design phase, so as to have sufficient margin to process signals up to 1 MHz, which is the upper bound of the frequency range of interest in this work. The effect of the offset cancellation circuit is also apparent in Fig. 5.15, where an attenuation higher than 25 dB is achieved for frequencies lower than 200 Hz.

Figure 5.16 shows the –3 dB input sensitivity of the limiting amplifier, S_{-3dB}, measured in three fabricated samples for a test signal frequency of 400 kHz.

This parameter is defined as the input power that leads to an output power 3 dB lower than the saturated constant level. Therefore, this parameter indicates that, for input signals whose amplitude is lower than S_{-3dB} the limiting amplifier begins to operate in its linear region. From Fig. 5.16, the measured sensitivity is –65 dBm. Only one or two of the last gain cells are in the saturation region. According to the ideal

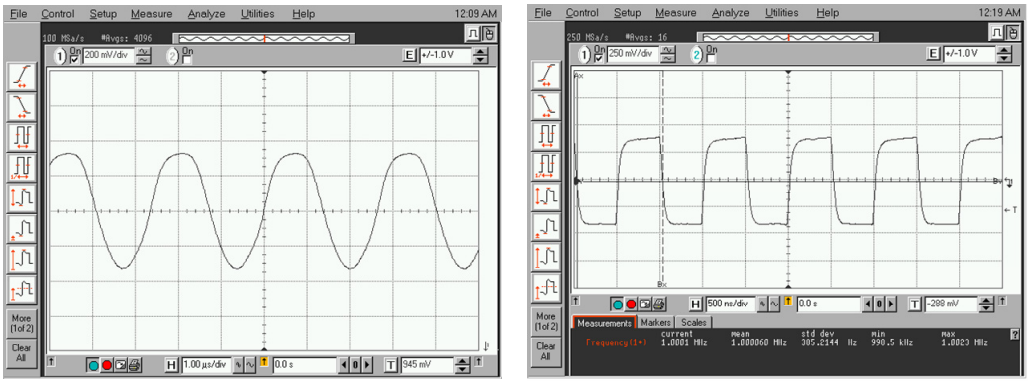

(a) (b)

Figure 5.17. a) Experimental response of the limiting amplifier to a 125-μV_{rms} 375-kHz sinewave signal. Vertical axis: 200 mV/div, horizontal axis: 1 µs/div and b) Experimental response of the limiting amplifier to a 1-mV_{rms} 1-MHz sinewave signal. Vertical axis: 250 mV/div, horizontal axis: 500 ns/div.

transfer characteristic of the gain cell, it can be readily shown that the –3 dB input sensitivity is given by

$$S_{-3dB} = \frac{V_{OL}}{\sqrt{2} \cdot DR_{in}} \tag{5.15}$$

The measured output signal for a –65 dBm 375-kHz input signal is shown in Fig. 5.17 (a). This output signal cannot be considered as a square-wave signal, but the contribution of odd frequency components is apparent. The experimental square-limited performance for a 1 MHz sinewave input signal is depicted in Fig. 5.17 (b). In this case, most of the gain cells work in the large-signal regime and the limited output signal is well established.

Figures 5.18 and 5.19 illustrate both outputs of the GPD circuit, i.e., v_{log} and v_p, respectively. In particular, Fig. 5.18 shows the full-rectified voltage signals of the GPD

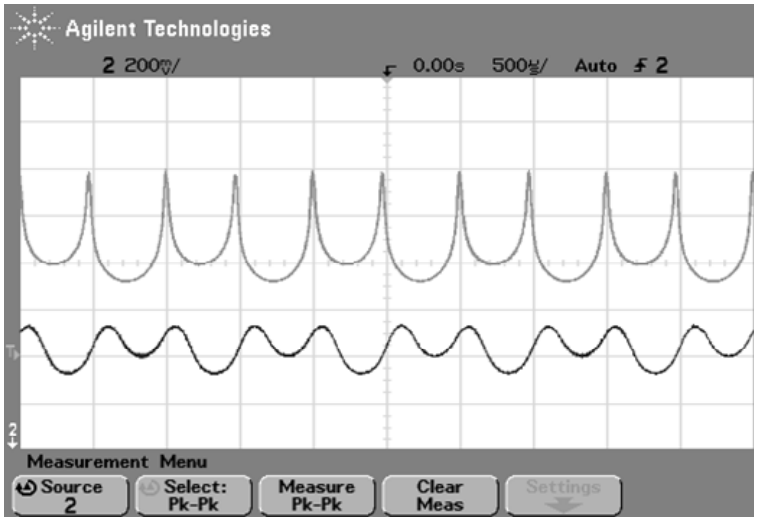

Figure 5.18. Experimental response of the logarithmic outputs of the two chains.

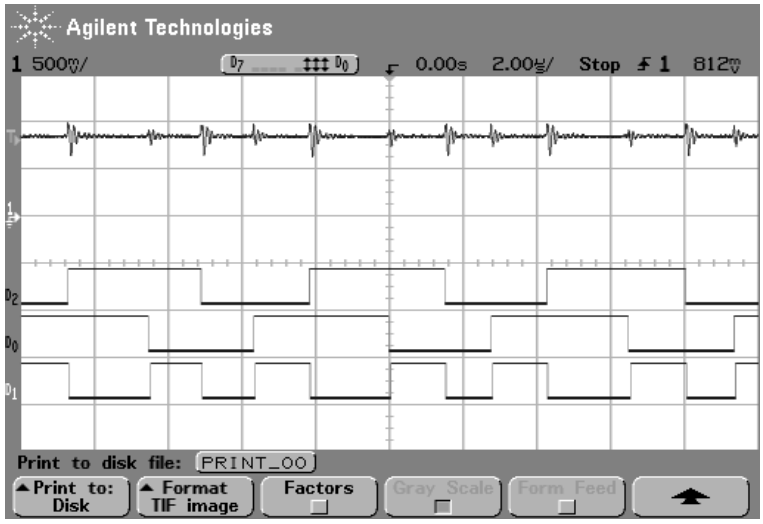

Figure 5.19. Experimental response of the phase detection for a signal with 72º of phase difference.

circuit with the logarithmic conversion information before being filtered and extracted. The measured DC voltage values together with the subtraction circuit allow obtaining

the magnitude ratio between the two signals. Figure 5.19 represents the limited output v_{LA} of the two chains (tracks D_0 and D_1), together with the XNOR signal that carries the phase difference information (track D_2) and its filtered version, i. e., v_{phase} (top trace, 812 mV, in Fig. 5.19).

Table V.I compares the performance of the proposed limiting amplifier with other previously reported solutions included in frequency shift keying (FSK) demodulators [5.23, 5.26], which are widely adopted for short-range receivers in biomedical systems and frequency-modulated (FM) receivers [5.22]. FSK and FM receivers use limiting amplifiers to generate rail-to-rail square wave versions of small input signals, and their bandwidth does not usually exceed a few tens of MHz. According to the above comparison, the proposed limiting amplifier consumes the lowest power with a comparable input sensitivity.

Table V.I. Performance summary of the designed CMOS limiting amplifier and comparison with prior works.

	[5.15]	[5.22]	[5.23]	[5.26]	This work
CMOS Technology	0.6 μm	0.8 μm	0.18 μm	0.6 μm	0.35 μm
Supply voltage	2 V	3.3 V	1.2 V	2 V	2 V
Number of gain stages	7	8	6	3	8
Power consumption	< 3 mW	22 mW	< 1 mW	1 mW	620 μW
Single stage gain	12 dB	N/A	N/A	28 dB	9.34 dB **
Single stage bandwidth	70 MHz	N/A	N/A	4.6 MHz	66 MHz **
-3 dB input sensitivity	-78 dBm @ 50Ω	N/A	N/A	-72 dBm @ 50Ω	-65 dBm @ 50Ω
Total gain	70 dB	110 dB	55 dB	N/A	72 dB
Bandwidth	22.58 MHz *	> 10.7 MHz	15 MHz	2.34 MHz *	3.8 MHz ***

(*) Estimated from the single stage bandwidth.
(**) Post-layout simulated result.
(***) Affected by the frequency response of a preceding instrumentation amplifier and the frequency response of a cascaded output buffer.

5.4. REFERENCES

[5.1] Y. Yang, J. Wang, G. Yu, F. Niu, and P. He, "Design and preliminary evaluation of a portable device for the measurement of bioimpedance spectroscopy," *Physiological Measurement*, vol. 27, pp. 1293-1310, Dec. 2006.

[5.2] P. O´Shea, Phase measurement, in *The Measurement, Instrumentation and Sensor Handbook*, J.G. Webster (ed), CRC Press, 1999.

[5.3] J. Cowles and B. Gilbert, "Accurate gain and phase measurement at radio frequencies up to 2.5 GHz," *Analog Dialogue*, vol. 35, nº. 05, Oct. 2001.

[5.4] R. W. Huggins, "Analytical fit of the transfer function of a logarithmic electrometer and correction for ambient temperature variations," *Review of Scientific Instruments*, vol. 44, pp. 297-300, March 1973.

[5.5] Y. B. Acharya and P. D. Vyavahare, "Remodeling light emitting diode in low current region," *IEEE Transactions on Electron Devices*, vol. 45, pp. 1426-1430, July 1998.

[5.6] S. Groiss and M. Koberle, "A high accurate logarithmic amplifier system with wide input range and extreme low temperature coefficient," *Proceedings of the 31st European Solid-State Circuits Conference (ESSCIRC)*, pp. 283-286, Sept. 2005.

[5.7] B. Wilson and M. Al-Gathtani, "Improved logarithmic converter based on a transconductance feedback amplifier," *IEEE International Symposium on Circuits and Systems (ISCAS)*, vol. 1, pp. 651-654, May 2001.

[5.8] A. Madjar, A. Paollela, and P. R. Herczfeld, "The compressive nature of optical detection in GaAs MESFETs and possible application as an RF logarithmic amplifier," *IEEE Transactions on Microwave Theory and Techniques*, vol. 41, pp. 165-167, Jan. 1993.

[5.9] C. Huang and S. Chakarabartty, "Current-input current-output CMOS logarithmic amplifier based on translinear Ohm´s law," *Electronics Letters*, vol. 47, pp. 433-434, March 2011.

[5.10] R. S. Hughes, *Logarithmic Amplification with Application to Radar and EW*, Artech House, 1986.

[5.11] A. Garskamp, "Logarithmic amplifier with sequentially limiting amplifier stages," U.S. Patent 5049829, Sept. 1991.

[5.12] W. L. Barber and E. R. Brown, "A true logarithmic amplifier for radar IF applications," *IEEE Journal of Solid-State Circuits*, vol. 15, pp. 291-295, June 1980.

[5.13] M. Shaterian, A. Abrishamifar, and H. Shamsi, "Analysis and design of the true piecewise approximation logarithmic amplifiers," *Analog Integrated Circuits and Signal Processing*, vol. 72, pp. 193-203, July 2012.

[5.14] J. C. Greer, "Error analysis for pseudo-logarithmic amplification," *Measurement Science Technology*, vol. 3, pp. 939-942, Oct.1992.

[5.15] P.–C. Huang, Y.–H Chen, C.–K. Wang, "A 2-V 10.7-MHz CMOS limiting amplifier/RSSI," *IEEE Journal of Solid-State Circuits*, vol. 35, pp. 1474-1480, Oct. 2000.

[5.16] R. P. Jindal, "Gigahertz-band high-gain low-noise AGC amplifiers in fine-line NMOS," *IEEE Journal of Solid-State Circuits*, vol. 22, pp. 512-521, Aug. 1987.

[5.17] C. Yang and A. Mason, "Process/temperature variation tolerant precision signal strength indicator," *IEEE Transactions on Circuits and Systems–I, Regular Papers*, vol. 55, pp. 722-729, April 2008.

[5.18] E. A. Crain and M. H. Perrott, "A 3.125 Gb/s limit amplifier in CMOS with 42 dB gain and 1 μs offset compensation," *IEEE Journal of Solid-State Circuits*, vol. 41, pp. 443-451, Feb. 2006.

[5.19] K. Kimura, "A CMOS logarithmic IF amplifier with unbalanced source-coupled pairs," *IEEE Journal of Solid-State Circuits*, vol. 28, pp.78–83, Jan. 1993.

[5.20] M. S. Steyaert, W. Dehaene, J. Craninckx, M. Walsh, and P. Real, "A CMOS rectifier-integrator for amplitude detection in hard disk servo loops," *IEEE Journal of Solid-State Circuits*, vol. 30, pp.743–751, July 1995.

[5.21] B. Razavi, *Design of Analog CMOS Integrated Circuits*, McGraw-Hill, 2001.

[5.22] D. Y. Gouda, M. Atef, A. El-Sabban, and M. El-Saba, "A low-cost 110 dB CMOS IF/limiter amplifier with offset cancellation," *Proceedings of the 15th International Conference on Microelectronics*, pp. 176-179, Dec. 2003.

[5.23] Y.–C. Chen, Y.–C. Wu, and P.–C. Huang, "A 1.2-V CMOS limiter/RSSI/demodulator for low-IF FSK Receiver," *Proceedings of the IEEE Custom Integrated Circuits Conference (CICC)*, pp. 217-220, Sept. 2007.

[5.24] P. R. Kinget, "Device mismatch and tradeoffs in the design of analog circuits," *IEEE Journal of Solid-State Circuits*, vol. 40, pp. 1212-1224, June 2005.

[5.25] K. D. Lawson and N. L. Brown, "Phase measuring circuit," U. S. Patent 4246497, Sept. 1981.

[5.26] P.–C. Huang, Y.–H. Chen, and C.–K. Wang, "A 2-V CMOS 455-kHz FM/FSK demodulator using feedforward offset cancellation limiting amplifier," *IEEE Journal of Solid-State Circuits*, vol. 36, pp. 135-138, Jan. 2001.

Chapter 6

AC CURRENT SOURCE

Design considerations on CMOS AC current source to be used as excitation block for bioimpedance measurements are discussed in this Chapter. State of the art of reported structures in literature together with the proposed solution adopted in this work is presented. Performance of the designed block is illustrated.

6.1. CURRENT SOURCE REQUIREMENTS AND TECHNIQUES

During the previous chapters of this work, the basics of the electrical bioimpedance technology have been deeply introduced. At the same time, different integrated techniques have been reported for processing bioimpedance information and, in particular, Chapter 4 and Chapter 5 illustrate the integrated solution proposed in this thesis. Regardless the selected silicon bioimpedance processing technique, an essential analog subsystem is the AC current source for the corresponding injection of the excitation signal. Deciding on a general specification for current sources is difficult, since different types of measurements have different accuracy requirements. Thereby, based on the considerations mentioned in previous chapters, the following criteria might be taken to be desirable: (1) Current amplitude should be as large as possible without compromising safety and low-power consumption. (2) The current source should introduce minimal common-mode voltage into the measuring circuit. (3) The design should meet the specification of the above factors over the design frequency-range. In this chapter the design of this block is discussed.

A well-established solution for obtaining fast bioimpedance response over a certain frequency range consists on the use of a unique excitation signal that contains the whole set of frequencies of interest, which in turns results in a single electrical response with the information of the behavior of the system under test for the complete desired frequency range. In this sense, rectangular wave signals have been explored as excitation signals in bioimpedance measurement systems resulting in effective and fast methods for wideband impedance spectroscopy [6.1]. In addition, the use of different broadband signals, e. g., multisines, chirps, or maximum length sequences, for excitation have been also reported [6.2]. In particular, Eq. (6.1) represents the time domain representation of the chirp excitation signal.

$$x(t) = \sin\left[\phi_0 + 2\pi\left(f_0 t + \frac{k}{2}t^2\right)\right] \tag{6.1}$$

Chirp signal increases the accuracy of measurement and can be easily scaled as in frequency, as well in time domain. Nevertheless, it exists a great complication in the generation of a perfect sine-wave chirp only using analog circuits. In this sense, there are some approaches that reduce the complexity of required software and hardware for chirp generation by using particular chirp signals [6.3]. For all of these wideband excitation solutions, the extraction of the spectral information is based in frequency processing operations, that involves a high design complexity and a large power consumption in silicon integrated implementations.

An alternative excitation technique to the wideband approach for bioimpedance spectroscopy measurements consists on sweeping a pure sinusoidal signal over the frequency range of interest. For this purpose, some previous approaches of excitation current sources were implemented either using an external signal generator [6.4] or FPGA-based direct digital synthesizers [6.5, 6.6]. These solutions offer high accuracy and linearity. Both mentioned approaches give rise to non-optimized power consuming measurement systems in order to be used in applications where low power and small size is required.

Different approaches have been reported in literature focusing on the design and performance of compact AC current source circuits –discrete and monolithic– dealing with electrical bioimpendance measurements [6.7-6.11]. The most important requirement in bioimpedance systems intended to extract information at several frequencies is to assure that the injecting current has constant amplitude over a wide frequency range regardless of the value of working load, which should be obtained by a high output impedance circuit [6.11]. However, non-idealities in the operational amplifiers used in the design of the current source circuits and the presence of stray capacitances make the current amplitude to be reduce and introduce phase shift errors at higher frequencies (> 100 kHz), which imposes a hard restriction when a large enough output impedance is required at these high frequencies [6.12].

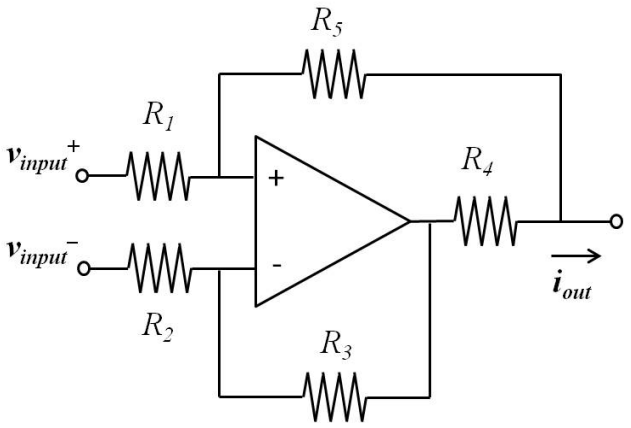

Figure 6.1. Schematic of the modified Howland current source. Redrawn from [6.14].

In particular, most of the AC current sources solutions for exciting a biological tissue are based on either the particular Howland current source (HCS) circuit or operational transconductance amplifiers (OTAs) acting as voltage controlled current sources (VCCS).

The first HCS circuit for converting a voltage into a current was proposed by Howland in 1962. However, the HCS structure suffers from output compliance and large sensitivity to the mismatch between the resistors used in the design of such a current source. In this sense, a modified version was suggested [6.13]. Figure 6.1 shows the modified Howland current source (MHCS) circuit. Taking into account that all resistors are perfectly matched and the operational amplifier has a large open-loop gain, then it can be established that the output current is given by $-v_{input}/r$, where $R_2=R_3=R_5=R$, $R_4=r$, $R_1=R+r$, and v_{input} corresponds to an external voltage signal.

The MHCS current source structure presents an output impedance which is proportional to the gain of the operational amplifier and inversely proportional to value of the load impedance. In addition, if high output impedance is intended for the MHCS circuit in order to get good common mode rejection ratio (CMRR), it is necessary to

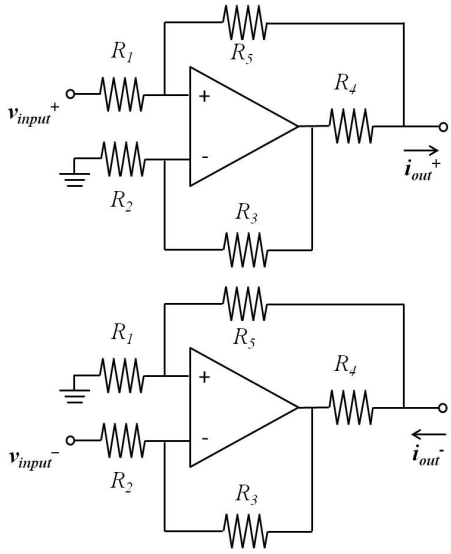

Figure 6.2. Schematic of the mirrored modified Howland current source. Redrawn from [6.14].

trim the resistors and the operational amplifiers should perform high input impedance values. On the other hand, the non-ideal characteristics of the operational amplifiers (i.e., input impedance Z_{in}, output impedance Z_o, and open-loop gain A) reduce frequency bandwidth of the current source.

Two-single-ended Howland circuits set together having a differential output current was proposed, also called as Mirrored Modified Howland Current Source (MMHCS), Fig. 6.2 [6.14]. This type of current source uses two equal input voltages with 180 degrees phase shift from each other but also has a unique reference for both sides of the circuit which, in turns, reduce the feed-through capacitance between output and input terminals.

This topology may significantly reduce the even harmonics distortion of the output current, and then improving its linearity and reducing the amount of output voltage level at each side of this current source. Furthermore, a differential structure increases

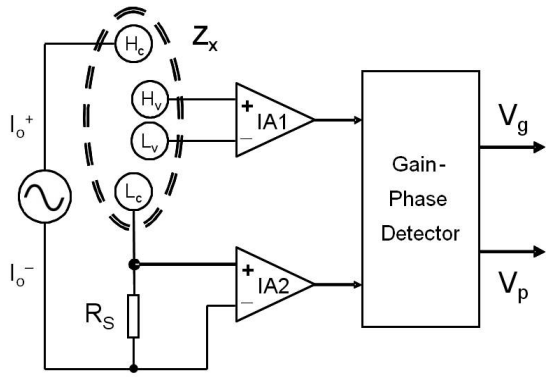

Figure 6.3. Fully differential current source over the tetrapolar electrode configuration.

the amplifier dynamic range, which is significantly important for low-power applications. Therefore, the use of differential current sources allows the minimization of the common mode voltage at the load, and then reducing the errors due to limited common mode rejection ratio of the voltage measuring amplifiers. However, and although the MMHCS circuit has a good performance for the harmonic distortion, OTA-based current sources counterparts have been shown to provide a wider output current frequency response and larger output impedance than the MMHCS circuit [6.15].

Taking into account the benefits of the use of fully differential current source structures, and the characteristic and drawbacks of the previously mentioned current source topologies, alternative differential solutions should be explored in order to face the particular requirements of the application described in this thesis –low-power, low-voltage, compact and wideband measurements with minimized dependence with current excitation value–. Figure 6.3 illustrates the tetrapolar electrode configuration used for bioimpedance monitoring driven by a differential sinusoidal current source.

6.2. WIEN-BRIDGE OSCILLATOR

The solution proposed in this work is based on the well-known harmonic Wien-Bridge oscillator [6.16]. The schematic diagram of the generic Wien-Bridge oscillator using the operational amplifier as an active building block is shown in Fig. 6.4.

In this ideal implementation, the open-loop gain is constant and given by

$$A(j\omega) = 1 + \frac{R_{2f}}{R_{1f}} \tag{6.2}$$

and the voltage-feedback transfer function $\beta(j\omega)$ can be written in the form

$$\beta(j\omega) = \frac{\omega RC}{3\omega RC + j\left(\left[\omega RC\right]^2 - 1\right)} \tag{6.3}$$

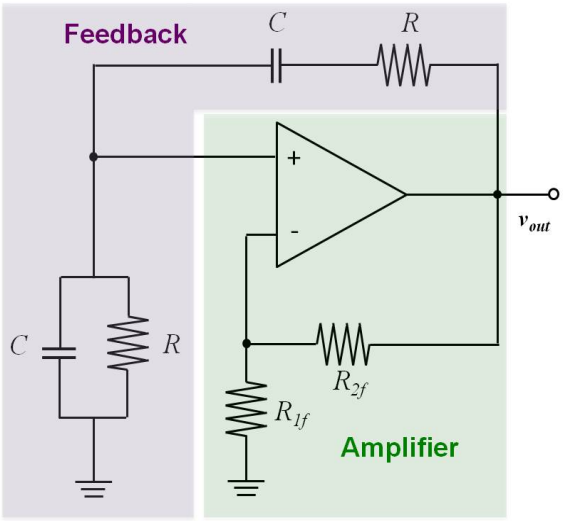

Figure 6.4. Conventional Wien-Bridge oscillator topology using a passive feedback network.

From Eq. (6.2) and Eq. (6.3) it follows that the loop gain is

$$H(j\omega) = \left(1 + \frac{R_{2f}}{R_{1f}}\right) \cdot \frac{\omega RC}{3\omega RC + j\left([\omega RC]^2 - 1\right)} \tag{6.4}$$

The Barkhausen criterion for oscillation is fulfilled when the loop-gain is equal to 1, i.e., the open-loop gain has a value of 3, and zero phase shift is obtained at the oscillation frequency oscillation. These conditions result in the following oscillation frequency, f_O:

$$f_O = \frac{1}{2\pi RC} \tag{6.5}$$

in which R and C are the values of the resistors and capacitors in the feedback network of Fig. 6.4. In particular, and from Eq. (6.2), it is established that $R_{2f} = 2R_{1f}$ in order to accomplish the oscillation criterion. In practice, the open-loop gain should be slightly higher than 3, i.e., 3.1-3.2, to start the oscillation. The Q-factor of this harmonic oscillator is derived from Eq. (6.3) being equal to 1/3.

Because of the fact that the oscillation frequency for the Wien-Bridge structure is only dependent on the passive RC network around the central amplifier, it supposes an interesting and convenience solution as AC excitation signal generator for compact spectroscopy applications with no need of external-applied input signal, where excitation frequency should cover a certain frequency range. From Eq. (6.5), it is observed that the frequency of oscillation can be varied by simultaneously changing the capacitance values and different frequencies ranges can be selected by simultaneously switching different values of the resistors R.

However, the oscillation condition have to be preserved under temperature changes and process variability, and the use of temperature stable passive elements and matching techniques should be consider during physical design stage. In addition, non-ideal operational amplifiers introduces the finite output impedance and phase shift to the transfer function. The output impedance becomes part of the feedback circuit, thereby becoming a determining parameter for the oscillation frequency and making the operational amplifier becomes the critical part of the oscillator circuit.

A temperature and process variability stable oscillator using the conventional Wien-Bridge topology implies the use of a very high-performance operational amplifier configurations, which in turn, limits the low-power operating capabilities of a such a circuit. To avoid this trade-off between power-consumption, temperature stability and absolute accuracy, improved operational amplifier topologies need to be used.

6.3. CIRCUIT DESIGN AND IMPLEMENTATION

Several AC current source implementations have been introduced in the initial section of this chapter. It has been established that the design of an AC excitation current for energy-efficient requirements involves silicon implementations, with low-power consumption, reduced size, and low complexity performance.

In particular, and considering electrical bioimpedance spectroscopy applications, the designed AC excitation source should be capable of working in the β-dispersion region frequency range (1 kHz – 1 MHz), with amplitude values up to 1 mA (peak-to-peak). At the same time, the proposed solution should minimize the degradation of the output impedance of the excitation current source because of the dependence with the load and also the excitation frequency. In this sense, a remark should be done concerning to the fact that the bioimpedance measuring technique implemented in this thesis does not need a constant current amplitude and high output impedance since the basics of the technique is the detection of ratriometric relations, so the absolute value of the current does not determine the accuracy of the obtained measurement.

Table VI.I. Current source implementations.

Current source	Disadvantages	Advantages
Rectangular wave excitation	High complexity	Fast response
Digital sweeping	Power consuming/size	Wideband
Howland based	External excitation	Wideband
OTA-based	External excitation	Wideband
Wien-Bridge oscillator	Process variability	Low power

According to the features presented by the previously mentioned AC current source structures, which are summarized in Table VI.I, it has been selected the one based on the Wien-Bridge oscillator because of its low-power performance and independence

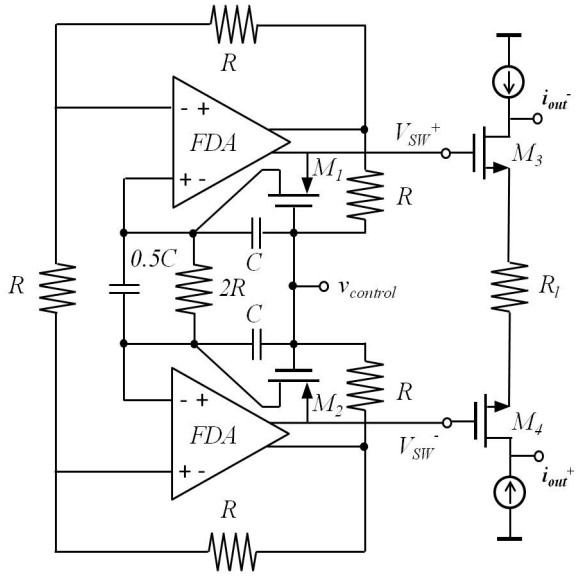

Figure 6.5. Differential sinusoidal AC current source structure. Redrawn from [6.17].

with external excitation. Figure 6.5 shows schematic circuit of a differential Wien-Bridge oscillator that consists of two fully differential amplifiers and an *RC* selective network. The oscillator generates a balanced sinusoidal voltage signal (V_{SW}^+ and V_{SW}^-), where the oscillation frequency value is determined by the *RC* time constant. Magnitude of the sinusoidal signal is adjusted by controlling the gate voltages of transistors $M_{1,2}$, $v_{control}$ in Fig. 6.5, by means of an automatic gain control (AGC) circuit. This compact structure allows programmability for the amplitude and oscillation frequency values of the current source by proper selection of a control voltage and passive components values, respectively. In addition, a voltage controlled current source consisting of $M_{3,4}$ and R_l, is series-connected to translate the differential voltage into a balanced current of $(V_{SW}^+ - V_{SW})/ R_l$ with a constant output impedance.

There exists a large variety of fully differential amplifier (FDA) structures that can be used as the FDA block of the AC current source presented in Fig. 6.5. Each amplifier structure has its own advantages and limitations and must be carefully

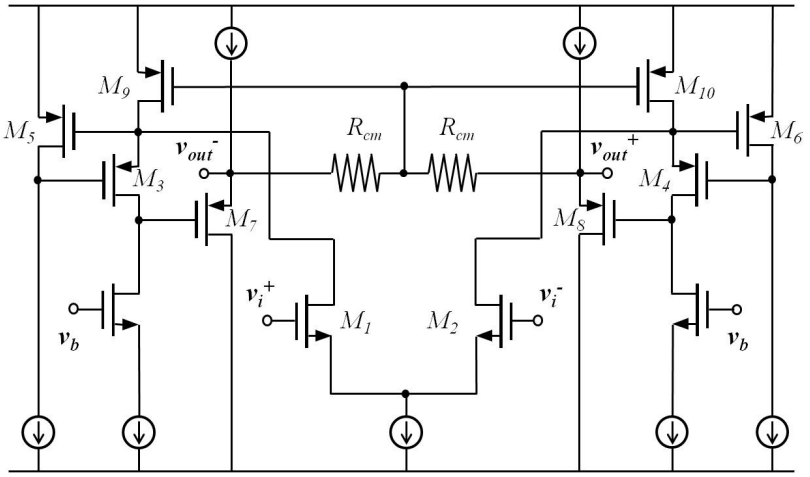

Figure 6.6. Fully differential amplifier (FDA) structure.

selected in order to comprise the low-power and high signal quality requirements. Figure 6.6 illustrates the designed fully differential amplifier. A gain-boosted folded-cascode structure shows the performance that best fit the desired specifications because of its very high DC open loop gain and low voltage operation, which in turn involves low-power consumption and high Q-factor. The Wien-Bridge oscillator requires the unity gain-bandwidth frequency of the FDA to be greater than four decades the oscillation frequency in order to maintain the gain and frequency within 10% of the designed values [6.16].

According to the oscillation frequency expression, Eq. 6.5, passive elements has been designed for obtaining two different oscillation frequencies so as to determine the suitability of the selected current source structure when spectroscopy measurements are required. Selected values of frequency correspond with the most widely use frequency excitation values for bioelectrical impedance measurements, i.e., 50 kHz and 100 kHz.

The absolute value of the passive components and their ratios determine not only the oscillation frequency and signal amplitude, even the harmonic distortion of the AC

output signal. Considering the feedback network and amplifier resistors ratio previously mentioned, i.e., $R_{2f} = 2R_{1f}$ in Fig. 6.4, it is derived a relative low harmonic distortion performance [6.18]. The harmonic distortion introduced by the term HD_3 is below -40 dB.

In order to guarantee an acceptable harmonic distortion at the oscillation frequency of -60 dB, it should be consider a R_{2f}/R_{1f} ratio higher than 2. Consequently, resistors and capacitors that constitute the feedback network in Wien-Bridge structure, should have different values, i.e., R_1-C_1, (pair connected to ground in Fig. 6.4), and R_2-C_2. Following design considerations in [6.18], an harmonic distortion of -60 dB can be obtained with $R_{2f}/R_{1f} \approx 10$ and a R_2/R_1 ratio of 2, considering an output signal of 100 mV and a 2 V supply voltage, V_{DD}.

As mentioned in previous section, process variability influence over passive elements in Wien-Bridge oscillator should be taken into account carefully during design tasks. The resistor value dispersion in the fabrication process utilized in this work can be established by the next expression:

$$\sigma_R = \sigma\left(\frac{\Delta R}{R}\right) = \frac{K_R}{\sqrt{W \cdot L}} \tag{6.6}$$

where σ_R corresponds to the dispersion in monolithic resistors due to fabrication process variability, K_R is a process variation parameter and $W \cdot L$ represents the silicon area occupied by the resistor.

Process dispersion of 0.1% for resistor implementation is set as a design specification, which involves a $W \cdot L$ area of 5000 μm^2 for POLY2 layer resistors in the AMS 0.35-µm fabrication process. The realization of the passive elements has been carried out using interdigitated implementations of Poly-Poly capacitors and serpentine

interdigitated high-resistivity resistors in the CMOS fabrication process used in this work.

Resistors and capacitor specific values for required oscillation frequencies are highlighted in Table VI.II:

Table VI.II. Passive parameters values.

Oscillation frequency	R_1	R_2	C_1	C_2
50 kHz	75 kΩ	150 kΩ	21.22 pF	10.6 pF
100 kHz	150 kΩ	300 kΩ	21.22 pF	10.6 pF

6.4. REFERENCES

[6.1] M. Min, T. Paavle, P. Annus, and R. Land, "Rectangular wave excitation in wideband bioimpedance spectroscopy," *IEEE International Workshop on Measurements and Applications*, pp. 268-271, May 2009.

[6.2] S. Gawad, T. Sun, N. G. Green and H. Morgan, "Impedance spectroscopy using maximum length sequences: application to single cell analysis," *Review of Scientific Instruments*, 78, 054301-1, American Institute of Physics, May 2007.

[6.3] M. Min and T. Paavle, "Broadband discrete-level excitations for improved extraction of information in bioimpedance measurements," *Physiological Measurement*, pp. 997-1010, June 2014.

[6.4] M. –C. Cho *et al.*, "A bio-impedance measurement system for portable monitoring of heart rate and pulse wave velocity using small body area," *Proceedings of the IEEE International Symposium on Circuits and Systems (ISCAS)*, pp. 3106-3109, May 2009.

[6.5] J. –W. Lee *et al.*, "Precission constant current source for electrical impedance tomography," *Proceedings of the25th Annual International Conference of the IEEE Engineering in Medicine and Biology Society*, pp. 1066-1069, Aug. 2003.

[6.6] C. –Y. Chiang *et al.*, "Portable impedance cardiography system for real-time noninvasive cardiac output measurement," *Proceedings of the 16th Annual International Conference of the IEEE Engineering in Medicine and Biology Society*, pp. 2072-2073, Nov. 1994.

[6.7] J. Frounchi, F. Dehkhoda and M.H. Zarifi, "A Low-distortion wideband integrated current source for tomography applications," *European Journal of Scientific Research*, vol. 27, pp. 56-65 , Feb. 2009.

[6.8] S. Grimnes and Ø. G. Martinsen, *Bioimpedance and Bioelectricity Basics* (2nd edition), Academic Press, 2008.

[6.9] R. González-Landaeta *et al.*, "Heart rate detection from plantar bioimpedance measurements," *IEEE Transactions on Biomedical Engineering*, vol. 55, no. 3, pp. 1163-1167, March 2008.

[6.10] H. Hong, M. Rahal, A. Demosthenous and R. H. Bayford , "Floating voltage-controlled current sources for electrical impednace tomography,"*18th European Conference on Circuit Theory and Design*, pp. 208-211, Aug. 2007.

[6.11] P. Bertemes-Filho, *Tissue Characterization Using an Impedance Spectroscopy Probe*, Ph. D. Thesis, University of Sheffield, U.K., 2002.

[6.12] D. X. Chen, X. Deng and W. Q. Yang, "Comparison of three current sources for single-electrode capacitance measurement," *Review of Scientific Instruments*, vol. 81, pp. 1-3, March 2010.

[6.13] F. Seoane, R. Bragós and K. Lindecranz, "Current source for multifrequency broadband electrical bioimpedance spectroscopy: A Novel Approach," *Proceedings of the 28th Annual International Conference of the IEEE Engineering in Medicine and Biology Society*, 3, pp. 5121-5125, Aug. 2006.

[6.14] P. Bertemes-Filho, L.H. Negri, A Felipe and V. C. Vincence, "Mirrored modified Howland circuit for bioimpedance applications: Analytical Analysis," *Journal of Physics: Conference Series*, vol. 407, nº 1, pp. 1-8, 2012.

[6.15] P. Bertemes-Filho, V. C. Vincence, M. M. Santos and I. X. Zanatta, "Low power current sources for bioimpedance measurements: a comparison between Howland and OTA-based CMOS circuits," *Journal of Electrical Bioimpedance*, vol. 3, pp. 66-73, Oct. 2012.

[6.16] L. Yang, J. Bae, S. Lee, T. Roh, K. Song and H. –J. Yoo, "A 3.9 mW 25- electrode reconfigured sensor for wearable cardiac monitoring system," *Journal of Solid State Circuits*, vol. 46, pp. 353-364, Jan. 2011.

[6.17] I. M. Gottlieb, *Practical Oscillator Handbook*, Newnes, 1997.

[6.18] G. Palumbo, M. Pennisi, and S. Penissi, "Wien-Type oscillators: Evaluation and optimization of harmonic distortion,"*IEEE Transaction on Circuits and Systems–II: Express Briefs*, vol. 55, pp. 628-632, July 2008.

Chapter 7

EBI-BSN MULTICHANNEL SYSTEM: REALIZATION AND RESULTS

The realization of a multichannel EBI system based on the BSN principle is the main subject of this Chapter. In particular, the different components of the system, hardware and software, not covered before are described. Experimental results of the bioimpedance CMOS sensor are also provided. In addition, static and dynamic behavior of a wireless EBI node are characterized. Finally, the operation of the whole system illustrating the multisite monitoring of physiological variables is shown.

7.1. OVERALL ANALOG FRONT-END

As stated from the beginning of this work, the final goal of this thesis is the design of a low voltage and power-efficient monolithic electrical bioimpedance spectrometer in order to collaborate in the improvement of the healthcare delivery system for facing the new challenging features that current economical, social and economic context demands.

Previous chapters have illustrated the design and performance of key circuits of the proposed bioimpedance spectrometer. Current chapter face the behavior of the whole multichannel system in the acquisition of complex bioimpedance values and some of the experimental measurements results that are carried out during this work are also presented. In particular, the first section of this chapter contains the results from the silicon integrated bioimpedance spectrometer together with a detailed description of the on-chip biasing section for the whole ASIC.

Figure 7.1 shows a microphotograph of the fabricated spectrometer chip

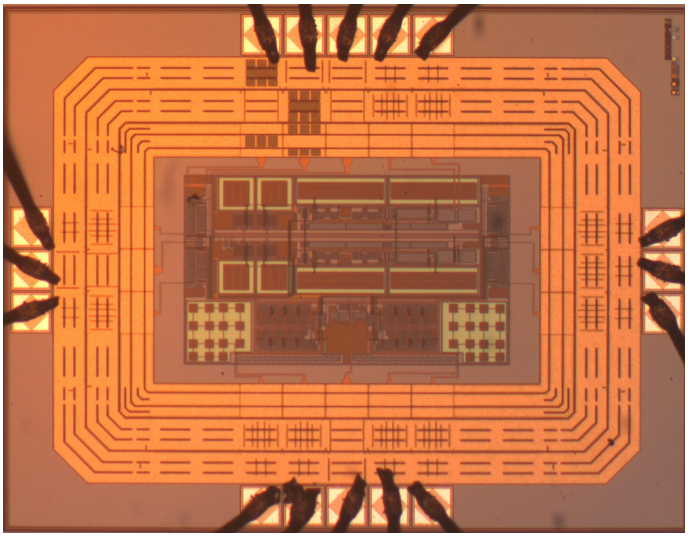

Figure 7.1. Microphotograph of the designed electrical bioimpedance spectrometer.

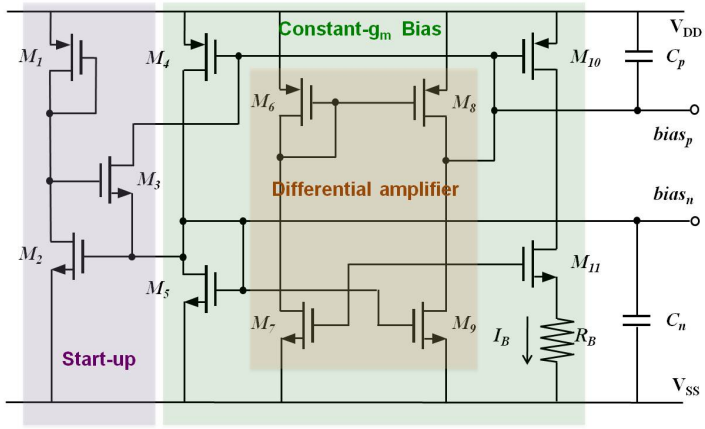

Figure 7.2. Circuit schematic of the on-chip biasing.

implemented in AMS 0.35-µm CMOS process, which occupies about 0.3 mm^2 of active area and 2 mm^2 of area including pads. The selected CMOS process is an affordable and well-proven solution for monolithic sensors currently supplied by most of the integrated circuit foundries.

7.1.1. On-chip biasing circuit

Together with the key analog processing blocks that perform the bioelectrical impedance magnitude and phase extraction, it has been included an on-chip biasing block in the fabricated ASIC, in order to properly establish the corresponding working status of the designed spectrometer. The addition of the on-chip biasing involves a reduction in the number of pads needed in the integrated circuit, together with avoiding the use of external circuitry dedicated to biasing purpose. These considerations agree with the objective of compact and cost-effective solution requirements pursued in this work.

The implemented on-chip biasing structure is shown in Fig. 7.2. The design of the

structure is developed in order to generate the required biasing current, I_B, and the biasing voltages, $bias_p$ and $bias_n$, which will drive the PMOS and NMOS transistors of the overall system, respectively. The circuit is composed of a constant-g_m bias circuit, M_4-M_5-M_{10}-M_{11}, operating in strong inversion, that generates the supply independent current trough resistor R_B. The circuit exhibit little supply dependence if channel-length modulation is negligible. For this reason, relatively long channels (L = 2 μm) are used for the transistors. A start-up circuit (M_1-M_3) is needed for setting a stable operating point [7.1]. Because of the inherent dependence of the circuit with supply voltage, V_{DD}, a differential amplifier (M_6-M_9) with a relative low gain (≈ 10) is added in order to provide independence against supply voltage variations.

The circuit depicted in Fig. 2 utilizes the value of resistor R_B and transistor dimensions for adjusting the biasing current value. The relation that establishes the value of the biasing current according to design parameters is [7.2]:

$$I_B = \frac{2}{\mu_n C_{ox}\left(\frac{W}{L}\right)_5} \cdot \frac{1}{R_B^2}\left(1-\frac{1}{\sqrt{K}}\right)^2 \tag{7.1}$$

where all the symbols have their usual meaning and K corresponds to the ratio $(W/L)_{11}$ / $(W/L)_5$.

The on-chip biasing is designed to provide 20 μA, and accordingly K is set to 4 and R_B is a 4.9 kΩ resistor designed in a serpentine structure implemented in POLY2 layer, which occupies a 576 μm^2 of silicon area. Figure 7.3 corresponds to the reference current trough M_{11} when V_{DD} is swept from 0 V to 2.5 V. The result shows the constant value of the required current once a certain value of supply voltage is reached, and, consequently a suitable performance of the design for minimizing the dependence of the required biasing current with supply voltage is obtained.

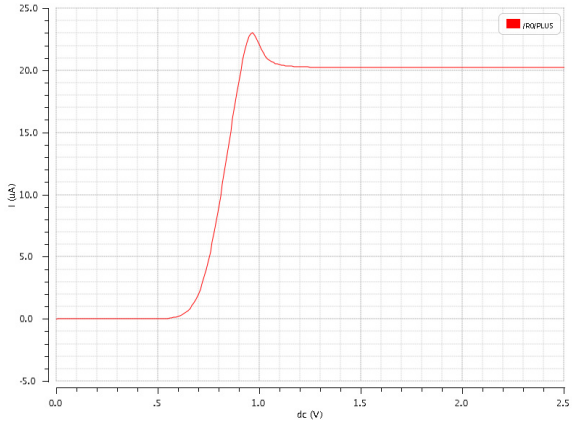

Figure 7.3. Biasing current, I_B, *vs* supply voltage, V_{DD}.

There are some design considerations of interest regarding the implementation of the resistor R_B. In particular, the biasing resistor is recommended to be on-chip in order to avoid external parasitic capacitance which could be present at the pad where the external resistor should be connected. The existence of parasitic capacitance at the source terminal of the transistor labelled M_{11} could give raise to instability effects that affect negatively the power-on circuit performance.

Monte Carlo statistical post-layout simulation results, where design parameter variations due to fabrication process and mismatch effects were considered, are illustrated in Fig. 7.4. In particular, DC voltage, $bias_n$, which supplies the NMOS transistors a biasing current of 20 µA is plotted. The designed value for $bias_n$ so as to obtain the required biasing current is 720 mV. Statistical simulation carries out a mean voltage value of 721 mV and a standard deviation of ±64.65 mV, and shows a voltage value distribution centered at the nominal value. Nevertheless, experimental tests of the fabricated prototypes illustrate some of the samples not working properly, and measured values of $bias_n$ were collected. Figure 7.5 depicts the set of measurements for ten different IC samples, carrying out voltages values corresponding to the upper limit of the post-layout simulations.

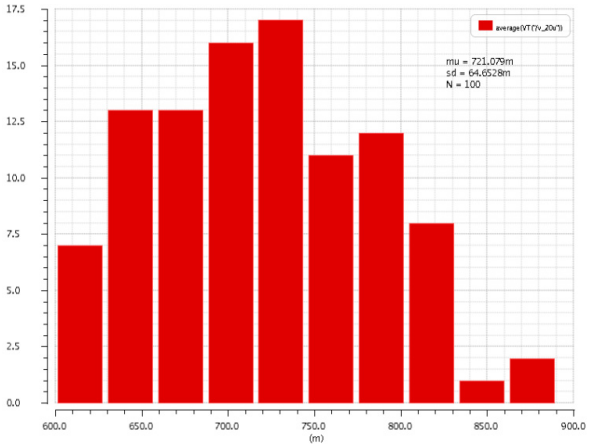

Figure 7.4. Monte Carlo histogram of DC voltage $bias_n$ for the on-chip biasing circuit.

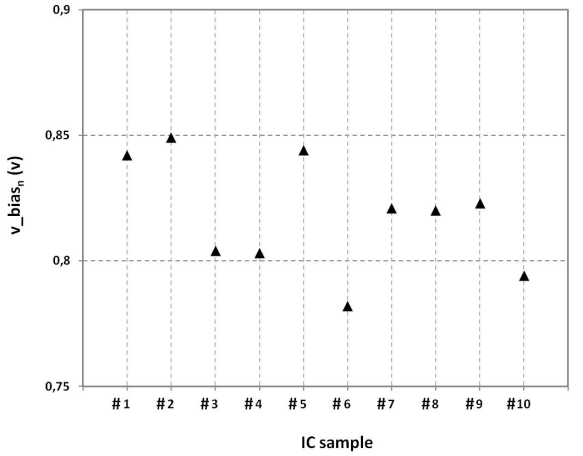

Figure 7.5. Experimental measurements of $bias_n$ voltage for the on-chip biasing circuit.

As a consequence of the experimental results obtained from the fabricated on-chip biasing circuit, it was needed a redesign of the structure in order to guarantee an optimal performance of the overall system. According to the statistical analysis, it was identified the resistor R_B as the component which involves the highest dispersion values. The use of a resistor matrix which consists on a differently size resistors can minimize the negative impact of fabrication process. However, this solution adds circuit complexity to the

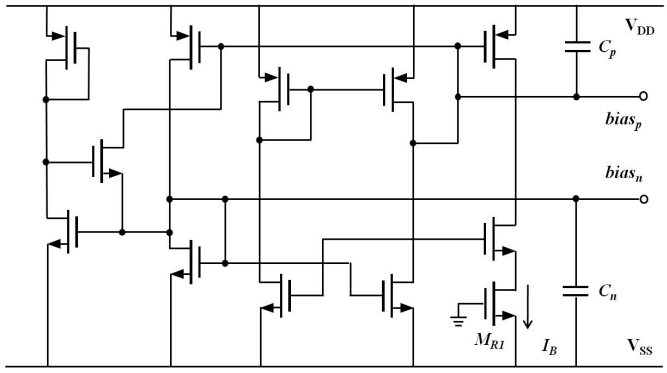

Figure 7.6. Circuit schematic of the redesigned on-chip biasing.

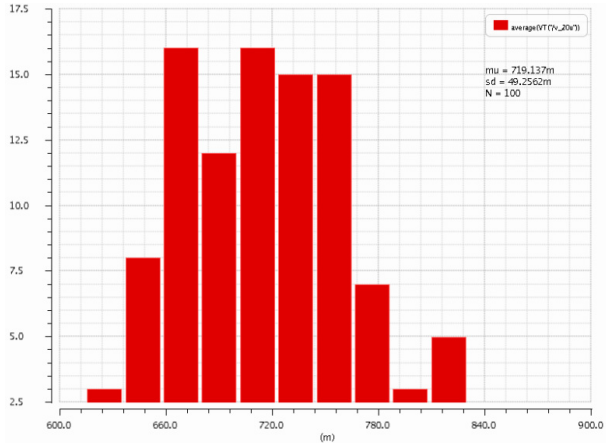

Figure 7.7. Monte Carlo histogram of $bias_n$ voltage for the redesigned on-chip biasing circuit.

design. In order to face this inconvenient, a transistor working in linear region is adopted for implementing the original resistor R_B in Fig. 7.2. Figure 7.6 illustrates the schematic of the modified structure for the on-chip biasing circuit where transistor M_{R1} constitutes the resistive component operating in linear region.

Results from statistical post-layout simulations of the redesigned version under conditions pointed out for the original biasing structure were obtained and are shown in Fig. 7.7. It is derived from the simulation results a mean voltage value of 719 mV and a

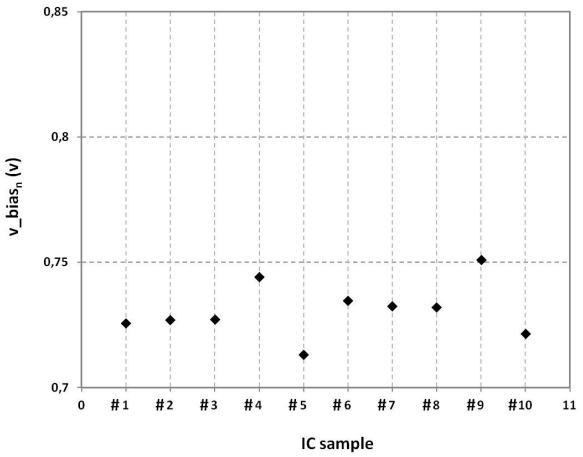

Figure 7.8. Experimental measurements of $bias_n$ voltage for the redesigned on-chip biasing circuit.

standard deviation of ±49.25 mV, which in turn involves a lower dispersion of voltage $bias_n$ values than the ones obtained for the original biasing structure, i.e. a higher robustness against fabrication process and mismatch variations.

In order to check the experimental performance and the suitability of the modified biasing structure, measurements of voltage $bias_n$ for ten IC samples were acquired. These experimental results are represented in Fig. 7.8, and show an overall performance close to the mean value obtained in statistical simulation.

7.1.2. Analog front-end characterization

In order to test the integrated spectrometer, it has been designed and implemented a two-layer PCB with USB communication capability for easy acquisition and processing of the data derived from the measurements provided from the electrical bioimpedance sensor. At the same time, the USB connection allows setting the desired excitation signal to be injected into the spectrometer through an user-friendly interface. Figure 7.9 illustrates the two-layer PCB with USB connection.

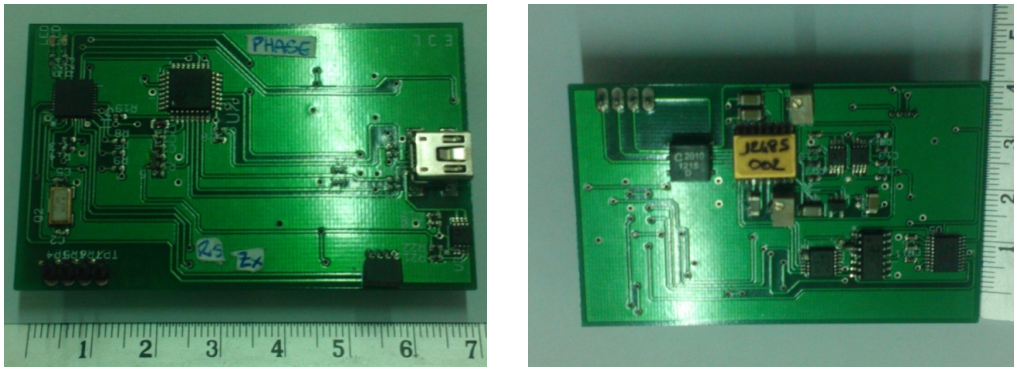

Figure 7.9. Photograph of the designed PCB for test.

A graphical user interface (GUI) was built using Matlab (8.2.0.701, The MathWorks Inc., Natick, MA, 2013) [7.3] in order to control and display the performance of the spectroscopy measurements. The GUI options are used to vary different parameters of the measurements system, such as frequency and/or amplitude of the excitation current. Figure 7.10 (a) presents a screenshot of the designed GUI, where magnitude and phase raw data – without further processing – obtained from the unknown impedance under test are illustrated. In particular, temporal measurements of the DC voltages corresponding to the magnitude and phase impedance information, i.e., V_g and V_p, are also shown.

Figure 7.10 (b) corresponds to the GUI option for representing the logarithmic relation between the magnitude of the unknown load and the DC voltage V_g, supplied by the designed bioimpedance sensor, which represents the magnitude transfer function of the sensor, i.e., Eq. (3.5). This option is especially useful for calibration tasks before performing measurements.

Once the test bench has been defined, the behavior of the sensor under working conditions is evaluated. Measurements over loads of known impedance are connected across the four electrodes in order to obtain V_g and V_p. Figure 7.11 illustrates the test

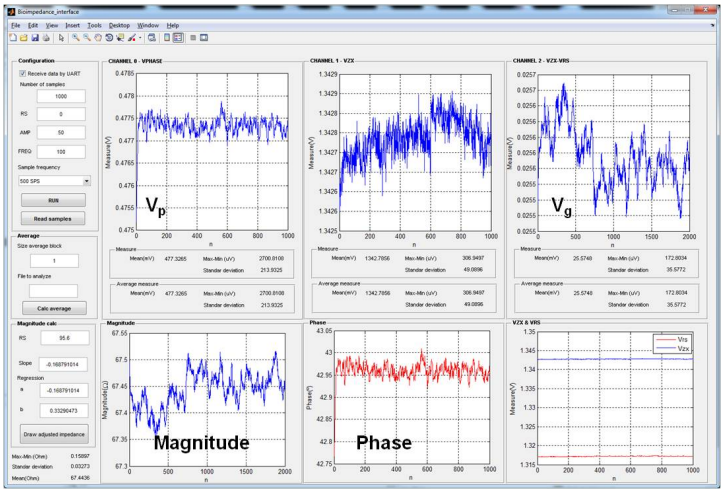

(a)

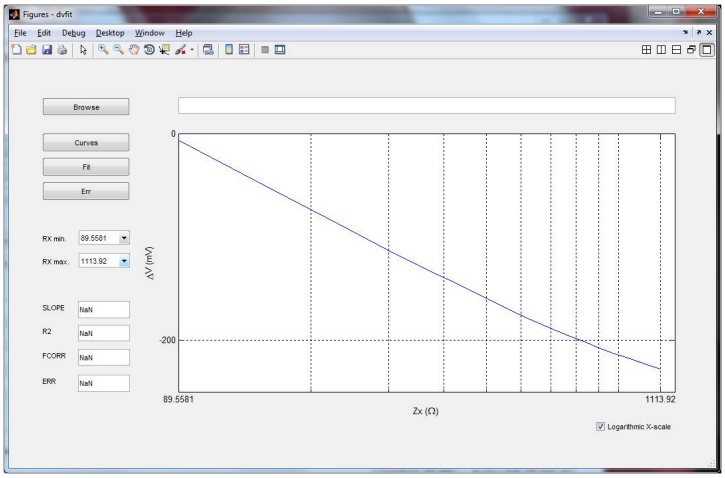

(b)

Figure 7.10. Graphical User Interface for EBI spectrometer test.

setup where the measurement system, i.e. USB designed PCB, is connected to the unknown impedance and is communicated with laptop via USB in order to extract and analyze the corresponding results.

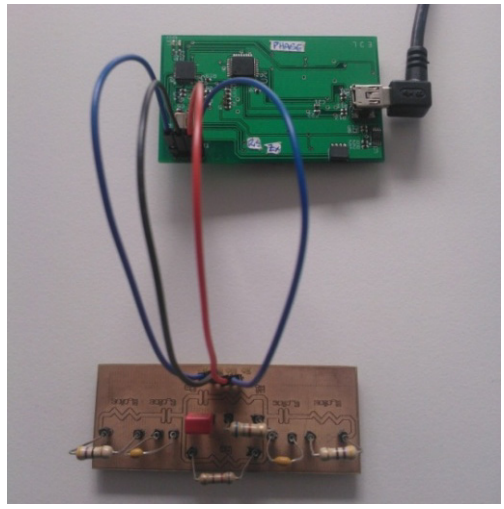

Figure 7.11. Test bench for impedance measurements.

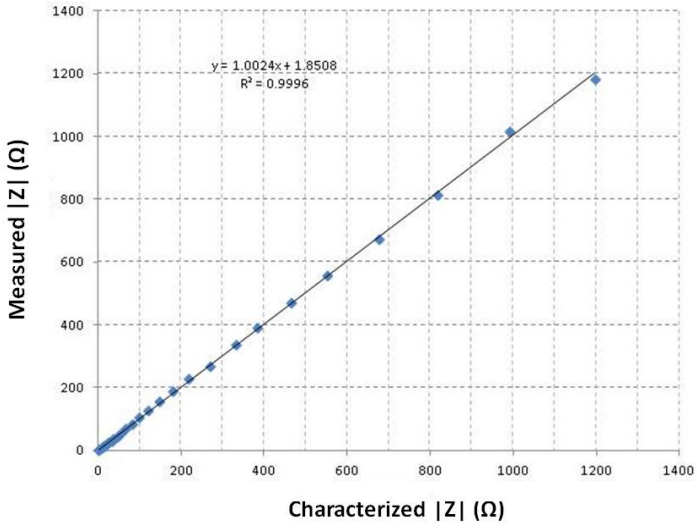

Figure 7.12. Spectrometer magnitude response.

Firstly, 5% metal film resistor loads with values varying from 1.3 Ω to 1.2 kΩ are characterized with a precision multimeter HP3410A, and then used in the test. Results from the above-mentioned test are drawn in Fig. 7.12, where a high correlation factor

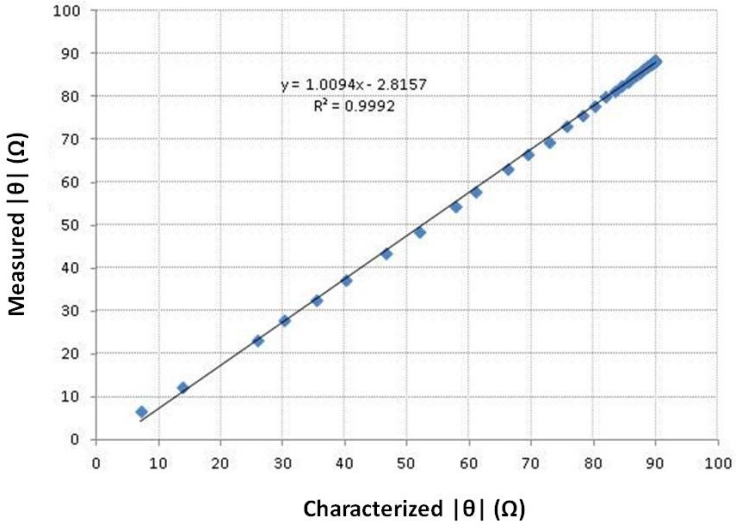

Figure 7.13. Spectrometer phase response.

between the characterized impedance magnitude and the value measured with the bioimpedance sensor, i.e. Eq. (3.5), exists (R^2 = 0.9996).

Once the overall magnitude range has been evaluated, the measurement of the phase variation is performed using a *RC* test circuit as system load. In this case, a 50 nF capacitor together with a resistor in parallel in the range from 1Ω to 10 kΩ have been used, and Fig. 7.13 shows the phase values extracted during the test. Similar to the magnitude performance of the sensor, high correlation factor between characterized and measured phase impedance values, i.e. Eq. (5.15), is obtained (R^2 = 0.9992).

The next step is the verification of the device behavior for *in vivo* measurements. The test circuit shown in Fig. 7.14, also known as *little man* circuit, simulates the typical impedance values obtained *in vivo* measurements, which is used by commercial electrical bioimpedance companies for calibrate their equipments, i.e. *Xitron Technologies* [7.4]. A series and parallel circuit combination is used consisting of a 1%

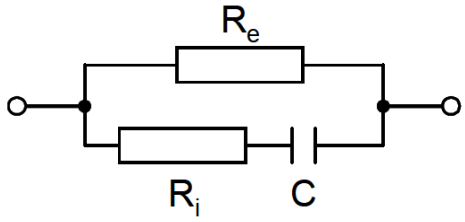

Figure 7.14. *In vivo* impedance equivalent circuit.

Table VII.I. *In vivo* equivalent circuit parameters.

	R_e	R_i	C
Measured value	681 Ω	909 Ω	3.3 nF

681 Ω metal film resistor in parallel with a series 1% metal film 909 Ω resistor and 5% 3.3 nF capacitor (Table VII.I). Capacitance is introduced by a 5% low dielectric absorption capacitor, axial leaded and of round construction, and made from either pollystyrene, polypropylene or teflon. To simulate resistance of contact electrodes, high quality 1% 50 Ω metal film resistors and 5% 100 nF capacitors were placed in series with the voltage and current connection terminals.

Using the *2R1C* equivalent circuit illustrated in Fig. 7.14 for the 5 kHz to 1 MHz frequency spectrum allows verifying the designed spectrometer under *in vivo* conditions. Figure 7.15 shows the spectrometer response together with the ideal value corresponding to the *in vivo* equivalent circuit for certain frequency values.

In order to facilitate the evaluation of the spectrometer performance over frequency, the respective resistive, *R*, and reactive, *X*, components of the measured impedance are computed at each frequency by taking the real and imaginary part of the complex $Z(\omega)$ magnitude. The resulting diagram, widely known as Cole-Cole plot [7.5], is of common use in electrical bioimpedance applications for evaluation of a certain biological material over frequency.

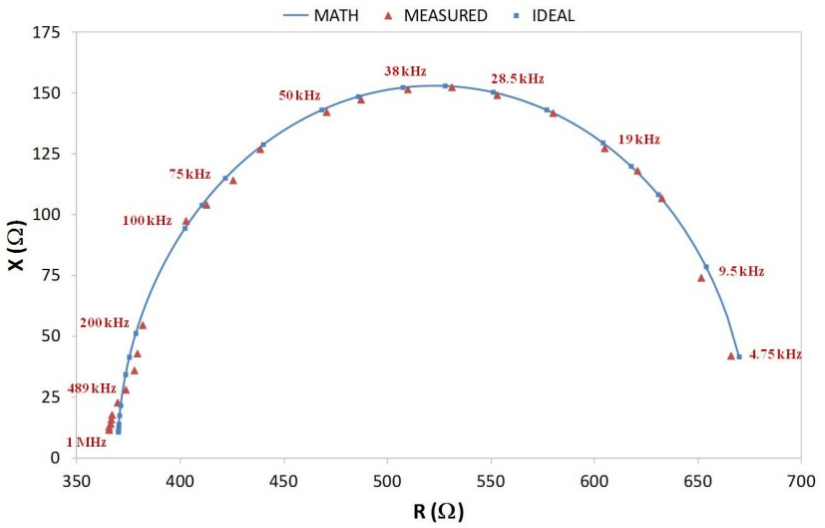

Figure 7.15. Cole-Cole plot in the impedance plane for measured values given in Table VII.I.

The theoretical impedance values presented in Fig. 7.15 are derived from those particular component values *2R1C* shown in Table VII.I by calculating the equivalent impedance of circuit shown in Fig. 7.14, which is given by the following formula:

$$Z(\omega) = R_e\left(\frac{1 + j\omega CR_i}{1 + j\omega C(R_e + R_i)}\right) \rightarrow Z(0) = R_e \text{ and } Z(\infty) = R_e \,||\, R_i \qquad (7.2)$$

Figure 7.15 illustrates certain deviation of the measurements at high-frequency values. The origin of this deviation, also widely known as *hook effect*, which involves a progressive increase of the imaginary component with frequency mainly due to parasitic capacitances, has been studied in literature and at the same time different software techniques have been reported in order to compensate this deviation [7.6, 7.7].

In addition to the presented experimental results of the designed sensor, it has been also obtained its dynamic behavior when variations of the impedance under test occurs

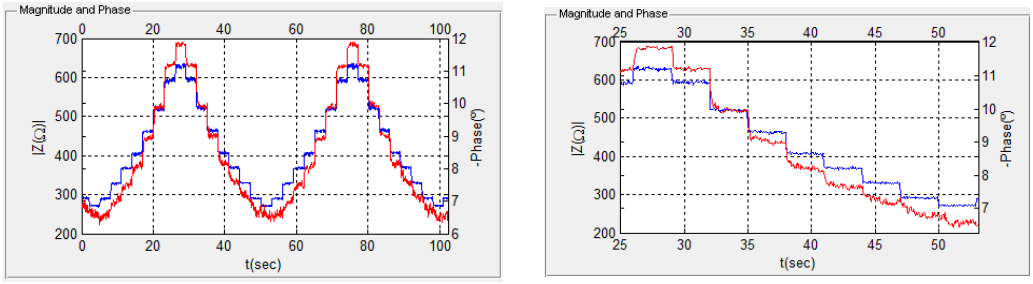

(a) (b)

Figure 7.16. a) Dynamic behavior of the designed bioimpedance sensor and b) Dynamic behavior detail.

Table VII.II. Experimental performance of the EBI sensor and commercial solutions.

	AD5933 (AD)	AFE4300 (TI)	This work
Measuring system	Bipolar	Tetrapolar	Tetrapolar
Excitation signal	Voltage	Programmable current	Programmable current (5 µA - 1 mA)
Frequency operation	1 kHz - 100 kHz	75 kHz	1 kHz - 2 MHz
Magnitude measurement range	1 kΩ - 10 MΩ	0 Ω - 2.8 kΩ	1 Ω - 1.2 kΩ *
Phase measurement range	N/A	N/A	0º - 90º
Supply voltage	2.7 V- 5.5 V	2 V - 3.6 V	2 V
Current consumption	10 mA- 25mA	1 mA	0.8 mA
Package	SSOP-16	TQFP-80	CSOIC-16
CMOS Technology	N/A	N/A	CMOS 0.35-µm

(*) Extended magnitude range (1 Ω – 2.7 kΩ).

in time. Figure 7.16 shows the magnitude ad phase response when the R_e resistor from circuit presented in Fig. 7.14 is implemented by a digital potentiometer which varies cyclically its value, which in turn involves a cyclic response of the measured magnitude and phase.

After the previously mentioned tests, the overall performance of the designed bioimpedance spectrometer is summarized in Table VII.II. In addition, performance of two commercial circuits used in bioimpedance applications are also reported.

It is straightforward from the previous table, the interest of the compact, low-power, high-performance silicon solution for bioimpedance applications presented in this work. Moreover, the solution detailed in the current work involves a promising starting point in order to explore the next steps for massive production.

7.2. EBI-BSN IMPLEMENTATION

Previous sections of this work have stated the need of shifting eHealth from desktop platforms to wireless and mobile configurations in order to enable a distributed and pervasive care model for health and wellness management which improves the quality of healthcare systems. For this purpose, and making use of the potential of the wireless sensor networks (WSNs), a wireless based bioelectrical impedance sensor network has been developed in this work.

Once the viability and feasibility of low voltage, power-efficient, integrated electrical bioimpedance measurement have been proved, this section is dedicated to the design, implementation and validation of remote monitoring of bioimpedance measurements through a wireless multichannel platform. Figure 7.17 shows the concept of the platform developed in this work.

As shown in Fig. 7.17, wireless EBI nodes are placed over the patient's areas of interest in order to carry out independent bioimpedance measurements and transfer the records to the BSN coordinator. The coordinator node is, in turn, wirelessly connected to the patient's end device, where data are processed. The collected records are available

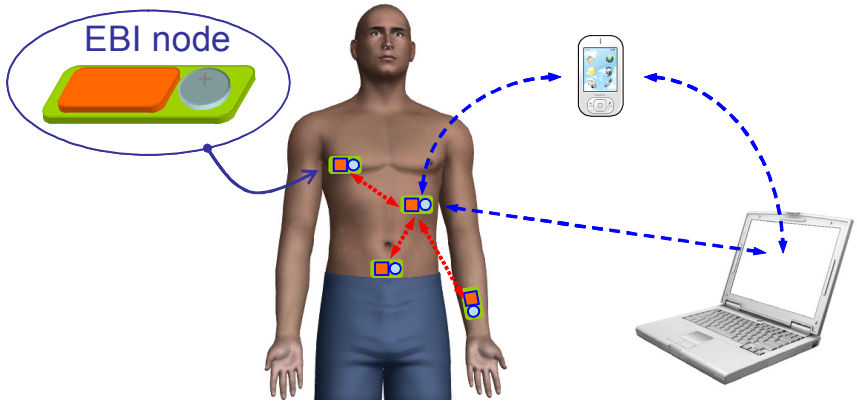

Figure 7.17. Proposed wireless multichannel electrical bioimpedance spectrometer.

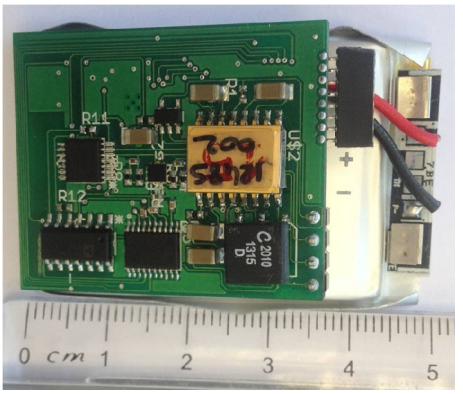

Figure 7.18. Photograph of the realized wireless EBI node.

to be transferred to a PC, laptop, smartphone, tablet, etc, for further analysis. It is straightforward derived that the proposed platform is a powerful instrument for cost-efficient remote monitoring of electrical bioimpedance measurements, leading to a small-factor easy-to-use multichannel healthcare instrument.

The wireless node is based on the electrical bioimpedance sensor characterized in the previous section. In particular, a microcontroller unit (MCU) supervises the operation of the whole EBI node, controls the amplitude and the frequency of the excitation current, and converts the ensuing DC voltages (V_g, V_p) to a digital code by using the inbuilt analog-to-digital converter. The obtained digital words are transmitted by a radiofrequency section following a low-power short-range wireless protocol (*ZigBee*). In addition, the MCU supports calibration tasks that aim at avoiding systematic measurement errors.

Figure 7.18 is a photograph of the realized wireless EBI node including battery supply. The heart of the proposed wireless section is the commercial solution CC2430 System-on-Chip from TI/Chipcon. The CC2430 is optimized for long-term battery operation and includes the CC2420 transceiver and an efficient 8051-based microcontroller, which implements the whole digital processing stage. The operation of

Table VII.III. Programmable parameters of the proposed wireless EBI node.

Parameter	Options	Parameter	Options
EBI analysis	• Single-frequency (SF-BIA) • Bioimpedance spectroscopy (BIS)	Num. of analyses/sweeps	• Single (SF-BIA, BIS) • Analysis time interval (SF-BIA, BIS)
Frequency	• Single value (SF-BIA) • Sweep and interval (BIS)	Amplitude excitation current	• Single value (SF-BIA. BIS) • Automatic tuning (SF-BIA, BIS)

every EBI node can be independently adjusted (Table VII.III) so as to optimally extract the electrical properties more appropriate for the study of a particular physiological event in a certain body location.

A more convenient GUI, EBI-WSN, was further developed in Matlab [7.3] in order to remotely define and control the operation of the wireless EBI nodes and show the performance of the BSN. The analysis and graphical representation of the measured results transmitted by EBI nodes are also included in the software. In addition, processing tasks of data provided by the wireless EBI node –derivative, integral, and FFT– are available in the graphical interface, with the aim of facilite the interpretation by experts of the collected physiological information. At the same time, the Cole model routine has been also implemented by software so as to fit the standard espectral bioelectrical impedance visualization.

Figure 7.19 illustrates the bioimpedance wireless sensor network GUI, and in particular, the graphics in Fig. 7.19 correspond to the raw data frequency behavior (20 kHz to 1 MHz) obtained from two different wireless nodes, i.e., two channels, with their load being the circuit of Table VII.I.

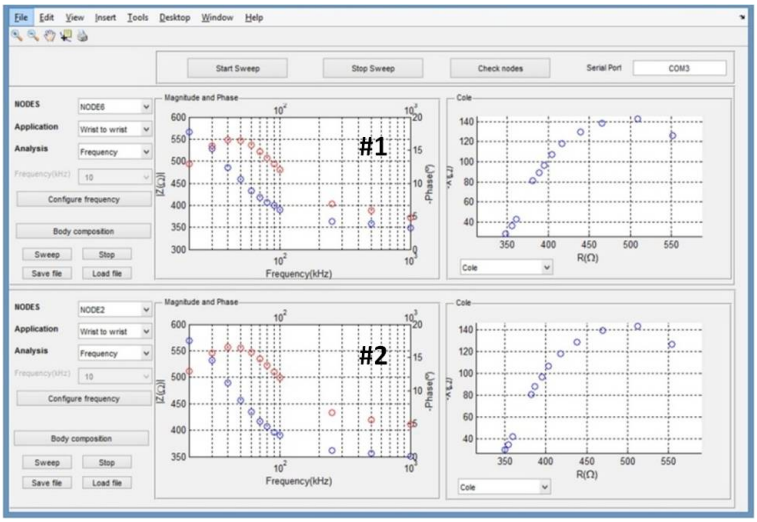

Figure 7.19. Performance of two wireless EBI node over the same load.

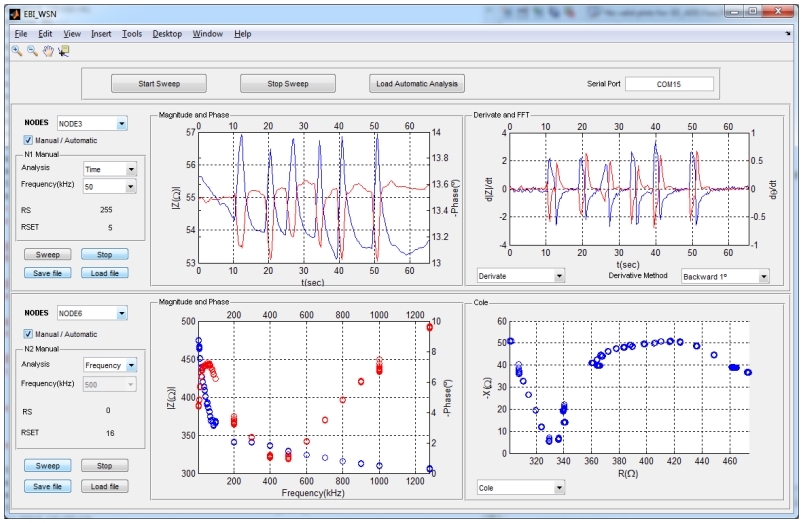

Figure 7.20. Front panel of the designed Matlab-based GUI for multichannel measurements.

The effectiveness of the developed GUI environment for collecting the results obtained from two wireless nodes simultaneously measuring two independent complex bioimpedances, i.e., two channels, is shown in Figure 7.20. In particular, Fig. 7.20

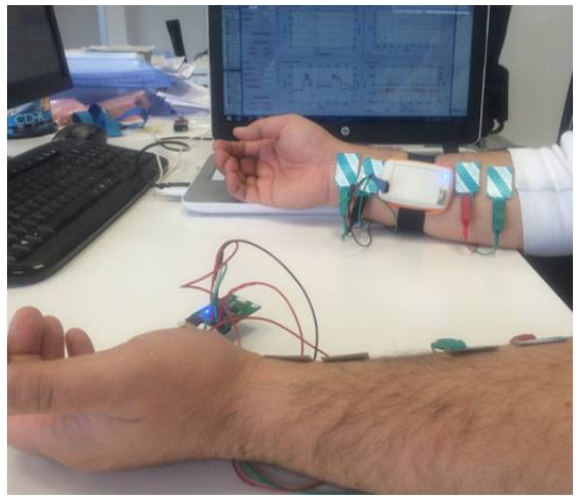

Figure 7.21. Physical deployment of the proposed EBI multichannel system.

illustrates two simultaneous different bioimpedance type of analysis performed by two independent wireless EBI nodes –magnitude (blue)/phase (red) –. The upper part of the graph shows the bioimpedance, magnitude and phase, time-variation under an excitation current of fixed frequency (50 kHz), which is of great interest for determinination of temporal physiological events and/or temporal evolution of physiological parameters related to bioimpedance values. In addition, the time derivative of magnitude and phase signals, which are directly correlated with physiological parameters, are also plotted. Simultaneously, a bioimpedance spectroscopy analysis from 5 kHz to 1 MHz is shown in the lower part of Fig. 7.20. Magnitude and phase values at several frequencies together with the corresponding Cole plot are depicted, which provide hig-valuable information for the determination of the composition/status of biological tissues. A physical deployment of the described measurements of the proposed multichannel electrical bioimpedance wireless sensor network is presented in Fig. 7.21 [7.8].

7.3. REFERENCES

[7.1] M. Paavola, M. Laiho, M. Saukoski, and K. Halonen, "A micropower 2 MHz CMOS frequency reference for capacitive sensor applications," *Proceedings of the 2005 European Conference on Circuit Theory and Design (ECCTD)*, vol. 3, pp. 425-428, Sept. 2005.

[7.2] B. Razavi, *Design of Analog CMOS Integrated Circuits*, Boston: McGraw-Hill, 2000.

[7.3] MATLAB: version 8.2.0.701 (R2013b). The MathWorks Inc., Natick, MA, (2013)

[7.4] http://www.xitrontech.com/assets/002/5854.pdf

[7.5] S. Grimnes and Ø. G. Martinsen, *Bioimpedance and Bioelectricity Basics* (2nd edition), Academic Press, 2008.

[7.6] R. Buendia, *Hook Effect on Electrical Bioimpedance Spectroscopy Measurements. Analysis, Compensation and Correction*, Master Thesis, Borås University, Borås, Sweden, 2009.

[7.7] R. Buendía, F. Seoane, and R. Gil-Pita, "A novel approach for removing the hook effect artefact from electrical bioimpedance spectroscopy measurements," *Journal of Physics: Conference Series*, vol. 224, nº1, 2010.

[7.8] J.L. Ausín, J. Ramos, G. Torelli and J.F. Duque-Carrillo, "Live demonstration: A wireless multichannel bioimpedance spectrometer for patient monitoring," *in Proceedings of the IEEE Biomedical Circuits and Systems Conference (BioCAS)*, Oct. 2014.

Chapter 8

CONCLUSIONS

In this Chapter the original contributions of this dissertation are summarized.

Key research contributions are summarized below:

1. Inspired in the operation of body sensor networks, an original approach for electrical bioimpedance (EBI) multichannel measurements has been proposed in this work. It allows the assessing either assorted physiological parameters or a physiological parameter at different positions of a living organism.

2. The design, realization and evaluation of a multichannel measurement system based on a high-performance integrated circuit for EBI measurements in the frequency range from 1 kHz to 1 MHz, and a low cost commercially available radio frequency transceiver device, have been presented.

3. An analog-front-end has been designed, fabricated in 0.35-µm CMOS technology and experimentally validated. Thanks to the measuring principle in which the operation is based, as well as the advanced analog and mixed-signal microelectronic design techniques used, the circuit acts as a low-voltage (i.e., 2 V) low-power high-performance monolithic EBI sensor.

4. The proposed sensor allows tetrapolar impedance measurements based on a magnitude-ratio and phase-difference detection method. The EBI sensor provides two DC voltage signals proportional to the magnitude and the phase of the measured bioimpedance by using an instrumentation amplifier and a gain-phase detector. This fact decreases the complexity of the rest of hardware and software necessary for bioimpedance processing.

5. A wideband low-power instrumentation amplifier (IA) based on the principle of current feedback has been designed and fabricated in a standard 0.35-µm CMOS process. The measurements have confirmed that the amplifier is capable of processing signals over a frequency interval from 100 Hz to 4 MHz with flat frequency response. The designed IA dissipates only 240 µW from a single 2-V supply.

6. A very compact gain-phase detector, which consists of two matched limiting/logarithmic amplifiers (LLAs), an XNOR-based phase detector, and a subtracting circuit, has been designed and fabricated in a standard 0.35-μm CMOS process. A systematic design procedure has been derived. As an outstanding result, the LLA is composed of eight cascaded gain stages that attain wide bandwidth performance with limited power consumption, whereas the logarithmic conversion of the input variable is carried out with the aid of nine detectors.

7. Design considerations on AC current sources to be used as excitation block for bioimpedance measurements have been discussed. A Wien-Bridge differential sinusoidal oscillator, specially addressed for wearable and implantable bioimpedance monitoring applications, has been designed in a standard 0.35-μm CMOS process.

8. The design of a wireless electrical bioimpedance analyzer/spectrometer – channel or node– that occupies a PCB area of few square centimeters ($< 9\ cm^2$) has been realized. It shows an attractive performance compared with commercially available portable equipment counterparts, in terms of size, weight, cost, and measurement capabilities.

9. The design of a wireless node has been carried out to operate within the β–frequency dispersion range and for covering the magnitude and phase angle bioimpedance variation ranges that occur in living organisms. As consequence, each wireless analyzer/spectrometer can perform physiological assessments through bioimpedance measurements over local areas, regional areas or whole-body.

10. Compared with bioimpedance multichannel measurement systems based on the traditional approaches, the following features of the proposed multichannel system can be highlighted:

- Scalability: operation can be performed with any number of channels/nodes.
- Configurability: channel operation is individually and wirelessly configured.
- Simultaneity: nodes operate simultaneously or according to any timing sequence, but in any case without any multiplexing technique.

11. A specific graphical user interface has been designed to carry out channels configuration in trials as well as for analysis of the bioimpedance measurements realized by the different nodes.
12. The proposed bioimpedance multichannel measurement system has been designed to operate with standard communication protocols, e.g., ZigBee and BLE, which allows to interact with other communication devices such as tablets, smartphones and laptops, and provides efficient solutions for most bioimpedance-based healthcare applications. It constitutes a versatile system for the development of new bioimpedance applications in biomedical research, development, and education.

Finally, and as a general remark, it seems convenient to highlight, at least in our opinion, that the multichannel measurement system introduced in this dissertation can constitute a new perspective for research in clinical applications of electrical bioimpedance thanks to the combination of bioimpedance raw values and avoidance of mathematical prediction models to overcome traditional limitations.

Capítulo 8

CONCLUSIONES

En este Capítulo se presentan las contribuciones originales del trabajo.

A continuación se recogen las contribuciones claves del presente trabajo:

1. Basado en la operación de las redes de sensores corporales, se ha propuesto un enfoque original para medidas multicanal de impedancia bioeléctrica (EBI). Dicho enfoque permite la evaluación de parámetros fisiológicos en diferentes localizaciones del organismo vivo.

2. Se ha presentado el diseño, realización y evaluación de un sistema multicanal basado en un circuito integrado para medidas EBI en el rango de frecuencias desde 1 kHz a 1 MHz, y un dispositivo comercial para comunicaciones inalámbricas.

3. Se ha diseñado, fabricado en una tecnología CMOS de 0.35- μm y experimentalmente validado un circuito de acondicionamiento de señales EBI. Debido a su principio de medida en el que se basa su operación. del mismo modo que a las avanzadas técnicas de diseño microelectrónico analógico y de modo mixto utilizadas, el circuito actúa como un sensor EBI de bajo consumo y altas prestaciones.

4. El sensor EBI propuesto permite medidas tetrapolares de impedancia basadas en el método de detección de relación de magnitud y diferencia de fase. El sensor suministra dos voltajes DC, proporcionales a la magnitud y a la fase de la impedancia compleja, medida mediante el uso de un amplificador de instrumentación y un detector de ganancia y fase. Este hecho disminuye la complejidad del resto del software y hardware necesario para el procesamiento de los datos de bioimpedancia.

5. Un amplificador de instrumentación (IA) con gran ancho de banda y bajo consumo basado en el principio de realimentación de corriente ha sido diseñado y fabricado en un proceso estándar 0.35-μm CMOS. Las medidas han confirmado que el amplificador es capaz de procesar señales en un rango de

frecuencia desde 100 Hz a 4 MHz. El IA diseñado consume 240 μW con alimentación de 2 V.

6. Un compacto detector de ganancia y fase, que consiste en dos amplificadores limitadores/logarítmicos (LLA), un detector de fase basado en XNOR, y un circuito restador, ha sido diseñado y fabricado en un proceso estándar 0.35-μm CMOS. Como resultado relevante, el LLA está compuesto de ocho etapas de ganancia en cascada que dan lugar a un comportamiento con gran ancho de banda y con consumo limitado, mientras que la conversión logarítmica de la variable de entrada se realiza con la ayuda de nueve detectores.

7. Consideraciones de diseño de fuentes de corriente AC para ser usados con bloques de excitación para medidas de bioimpedancia han sido enunciadas. Un oscilador senoidal diferencial basado en la estructura Wien-Bridge, especialmente dirigido para aplicaciones de monitorización wearable e implantable ha sido diseñado en un proceso de proceso estándar 0.35-μm CMOS.

8. El diseño de un analizador/espectrómetro de bioimpedancia eléctrica inalámbrico –canal o nodo– que ocupa pocos cm^2 de área (<9 cm^2) ha sido realizado. Dicho espectrómetro presenta un atractivo comportamiento comparado con las alternativas comercialmente disponibles de equipos portables, en términos de tamaño, peso, coste y capacidades de medida.

9. El diseño de un nodo inalámbrico ha sido llevado a cabo para operar dentro del rango de frecuencias de la región dispersión β para cubrir los rangos de variación de la magnitud y fase de bioimpedancia que ocurre en organismos. Como consecuencia, cada analizador/espectrómetro inalámbrico puede desarrollar evaluaciones fisiológicas a través de las medidas de bioimpedancia sobre áreas localizadas, regiones de área o en cuerpo completo.

10. Comparado con los sistemas multicanal de bioimpedancia basados en los enfoques tradicionales, las siguientes características del sistema multicanal propuesto son resaltadas:

    - Escalabilidad: la operación puede ser realizada por un número escalable de canales/nodos.

    - Configurabilidad: la operación del canal es individualmente e inalámbricamente configurada.

    - Simultaneidad: los nodos pueden operar simultáneamente o de acuerdo a una secuencia temporal, pero en cualquier caso sin utilizar técnicas de multiplexación.

11. Se ha diseñado un interfaz gráfico de usuario específico para realizar la configuración de los canales durante los ensayos, y para la realización del análisis de las medidas de bioimpedancia realizadas por los diferentes nodos.

12. El sistema de medida multicanal de bioimpedancia propuesto ha sido diseñado para operar con protocolos estándares de comunicación, como por ejemplo ZigBee y BLE, que permiten la interacción y comunicación con dispositivos tales como ordenadores portátiles, tablets o smartphones, y proporciona soluciones eficientes para la mayoría de las aplicaciones de salud basadas en bioimpedancia. El sistema constituye una herramienta versátil para el desarrollo de nuevas aplicaciones de bioimpedancia el investigación biomédica, desarrollo y educación.

Finalmente, y como indicación general, creemos conveniente resaltar, al menos en nuestra opinión, que el sistema multicanal presentado en este trabajo puede constituir una nueva perspectiva para la investigación en aplicaciones clínicas de la bioimpedancia eléctrica gracias a la combinación de valores brutos de bioimpedancia y evitando modelos predictivos matemáticos para solventar limitaciones tradicionales.

References

Chapter 1

[1.1] United Nations, Population Facts: Towards global equity and longevity, Population Facts, No. 2012/2, April 2012. Available: http://www.un.org/esa/population/publications/popfacts/popfacts__2012-2.pdf

[1.2] Y. T. Zhang and C. C. Y. Poon, "Innovative biomedical information technologies for low cost healthcare," *6th International Special Topic Conference on Information Technologies Applications on Biomedicine*, pp. 64-65, Nov. 2007.

[1.3] C. C. Y. Poon and Y.–T. Zhang, "Perspectives on high technologies for low–cost healthcare. The Chinese scenario," *IEEE Engineering in Medicine and Biology Magazine*, pp. 42-47, September/October 2008.

[1.4] E. Mosslialos, M. Wenzl, R. Osborn, and C. Anderson, "International Profiles of Health Care Systems, 2014," *The Commonwealth Fund*, Jan. 2015.

[1.5] R. R. Fletcher, M.–Z. Poh, and H. Eydgahi, "Wearable sensors: opportunities and challenges for low-cost health care," *Proceedings of the 32nd Annual International Conference of the IEEE Engineering in Medicine and Biology Society (EMBS)*, pp. 1763-1766, Sept. 2010.

[1.6] R. Allan, "Get your prescription for personal medical electronics," *Electronic Design*, pp. 14-23, 2013.

[1.7] A. Honka, K. Kaipainen, H. Hietala, and N. Saranummi, "Rethinking health: ICT-enabled services to empower people to manage their health," *IEEE Reviews in Biomedical Engineering*, vol. 4, pp. 119-140, 2011.

[1.8] U. Mulasi *et al.*, "Bioimpedance at the bedside: current applications, limitations, and opportunities," *Nutrition in Clinical Practice*, vol. 30, pp. 180-193, April 2015.

[1.9] R. Bayford and A. Tizzard, "Bioimpedance imaging: an overview of potential clinical applications," *Analyst,* vol. 137, pp. 4635-4643, 2012.

[1.10] S. F. Khalil, M. S.Mohktar, and F. Ibrahim, "The theory and fundamentals of bioimpedance analysis in clinical status monitoring and diagnosis of diseases," *Sensors*, vol. 14. pp. 10895-10928, 2014.

[1.11] T. Kanti Bera, "Bioelectrical impedance methods for noninvasive health monitoring: a review," *Journal of Medical Engineering*, 28 pages, http://dx.doi.org/10.1155/2014/381251, 2014.

[1.12] F. G. F. Mitchell, "Clinical achievements of impedance analysis," *Med. Biol. Eng. Comput*., vol. 47, pp. 153-163, 2009.

[1.13] T. Maheshwari and N. Bhardwaj, "Bioelectrical impedance analysis: A healthcare technology of the future," *International Journal of Enhanced in Science Technology & Engineering*, vol. 3, pp. 102-110, 2014.

Chapter 2

[2.1] S. Grimnes and Ø. G. Martinsen, *Bioimpedance and Bioelectricity Basics* (2nd edition), Academic Press, 2008.

[2.2] A. Stahn, E. Terblanche, and H.–C. Gunga, "Use of bioelectrical impedance: general principles and overview," *Handbook of Anthropometry*, Ch. 3, pp. 49-90, Springer-Verlag, 2012.

[2.3] D. Miklavcic, N. Pavšelj, and F. X. Hart, "Electric properties of tissues," *Wiley Encyclopedia of Biomedical Engineering*, vol. 6, pp. 3578-3589, John Wiley & Sons, 2006.

[2.4] J. G. Webster, *Medical Instrumentation. Application and Design* (Fourth edition), John Wiley & Sons, 2010.

[2.5] E. T. McAdams, *A Study of Electrode-Tissue Impedance Encountered in Cardiac Pacing*, Ph. D. Thesis, University of Leeds, UK, 1987.

[2.6] P. Bertemes-Filho, *Tissue Characterization using an Impedance Spectroscopy Probe*, Ph. D. Thesis, University of Sheffield, U.K., 2002.

[2.7] P. Aberg, "Method and apparatus for diagnosing a diseased condition in tissue of a subject," U.S. Patent 2010/0191141, Jul. 2010.

[2.8] F. Goldkuhl *et al*., "Switch probe for multiple electrode measurement of impedance," U.S. Patent 2011/0282180, Nov. 2011.

[2.9] E. Bouty, "Sur la conductibilité electrique de dissolutions salines très étendues," *Journal de Physique Théorique et Appliquée*, vol. 3, pp. 325-355, Aug. 1884.

[2.10] A. O. Ragheb, L. A. Geddes, J. D. Bourland, and W. A. Tacker, "Tetrapolar electrode system for measuring physiological events by impedance," *Medical & Biological Engineering & Computing*, vol. 30, pp. 115-117, Jan. 1992.

[2.11] H. P. Schwan, "Determination of biological Impedances," *Physical Techniques in Biological Research*, Academic Press, 1963, 323.

[2.12] R. Patterson, "Bioelectric Impedance Measurements," *The Biomedical Engineering Handbook*: (Second Edition), CRC Press LLC, 2000.

[2.13] E. Atzler and G. Lehmann, "Über ein neues Verfahren zur Darstellung der Herztätigkeit (Dielektrographie)," *European Journal of Applied Physiology*, vol. 5, pp. 636-680, May 1932.

[2.14] J. Nyboer, *Electrical Impedance Plethysmography* (Second Edition), U.S.A., Charles C. Thomas, 1970.

[2.15] J. Nyboer and J. G. Kornmesser, "Electrical impedance of the abdomen during maternal labor," *Annals of the New York Academy of Science*, vol. 170, pp. 801-803, July 1970.

[2.16] J. Nyboer, "Workable volume and flow concepts of biosegments by electrical impedance plethysmography," *Tower International Technomedical – Journal of Life Sciences*, vol. 2, pp. 1-13, Jan. 1972.

[2.17] P. Squara, "Bioreactance: A New Method for Non-invasive Cardiac Output Monitoring" in *Intensive Care Medicine* (J. L. Vincent, Ed.), pp. 619-630, Springer-Verlag, 2008.

[2.18] D. G. Jakovljevic, M. I. Trenell, and G. A. MacGowan, "Bioimpedance and bioreactance methods for monitoring cardiac output," *Best Practice & Research Clinical Anaesthesiology*, vol. 28, pp. 381-394, 2014.

[2.19] C. D. Ferris, *Introduction to Bioelectrodes*, Plenum Press, 1974.

[2.20] R. Pallàs-Areny and J. G. Webster, *Analog Signal Processing*, John Wiley & Sons, 1999.

[2.21] J. Songer, "Tissue ischemia monitoring using impedance spectroscopy; Clinical evaluation," in *Biomedical Engineering*, vol. Master´s degree, Worcester Polytechnic Institute, 2001.

[2.22] A. Yufera *et al.*, "A tissue impedance measurement chip for myocardial ischemia detection," *IEEE Transactions on Circuits and Systems–I, Regular Papers*, vol. 52, pp. 2620-2628, Dec. 2005.

[2.23] R. Pallàs-Areny and J. G. Webster, "Bioelectric impedance measurements using synchronous sampling," *IEEE Transactions on Biomedical Engineering,* vol. 40, pp. 824–829, Aug. 1993.

[2.24] R. D. Cook *et al.*, "ACT3: A high-speed, high-precision electrical impedance tomograph," *IEEE Transactions on Biomedical Engineering*, vol. 41, pp. 713-722, Aug. 1994.

[2.25] N. Liu, G. J. Saulnier, and J. C. Newell, "A multichannel synthesizer and voltmeter for electrical impedance tomography," *Proceedings of the 25th Annual International Conference of the IEEE Engineering in Medicine and Biology Society,* pp. 3110-3111, Sept. 2003.

[2.26] J. Balendonck and M. A. Hilhorst, "Application of an intelligent dielectric sensor for soil water content, electrical conductivity and temperature," *Proceedings of the 18th IEEE Instrumentation and Measurement Technology Conference*, vol. 3, pp. 1817-1822, May 2001.

[2.27] M. Min, O. Märtens, and T. Parve, "Lock-in measurement of bio-impedance variations," *Measurement*, vol. 27, pp. 21-28, Jan. 2000.

[2.28] R. Casanella, O. Casas, and R. Pallàs-Areny, "Differential synchronous demodulator for modulating sensors and impedance measurements," *Measurement Science and Technology*, vol. 16, pp. 1637-1643, Aug. 2005.

[2.29] P. Aberg, *Skin Cancer as seen by Electrical Impedance*, Ph. D. Thesis, Karolinska Institutet, Stockholm, Sweden, 2004.

[2.30] L. Beckman, D. van Riesen, and S. Leonhardt, "Optimal electrodes placement and frequency range selection of lung water using bioimpedance spectroscopy," *Proceedings of the 29th Annual International Conference of the IEEE Engineering in Medicine and Biology Society*, pp. 2685-2688, Aug. 2007.

[2.31] Y. Yang, J. Wang, G. Yu, F. Niu, and P. He, "Design and preliminary evaluation of a portable device for the measurement of bioimpedance spectroscopy," *Physiological Measurement*, vol. 29, pp. 1293-1310, Dec. 2006.

[2.32] D. Bouchaala, A. Fendri, and O. Kanoun, "Handheld bioimpedance spectrometer for the total frequency range of β–dispersion," *Proceedings SENSOR*, pp. 175-180, 2013.

[2.33] A. Rottigni, M. Carminati, G. Ferrari, and M. Sampiestro, "Handheld bio-impedance measurement system based on an instrument-on-chip," *7th Conference on Ph.D. Research in Microelectronics and Electronics (PRIME)*, pp. 49-52, July 2011.

[2.34] I. F. Triantis *et al*., "A multi-frequency bioimpedance measurements ASIC for electrical impedance tomography," *Proceedings of the European Solid-State Circuits Conference (ESSCIRC)*, pp. 331-334, Sept. 2011.

[2.35] P. Kassanos et al., "An integrated analog redout for multi-frequency bioimpedance measurements," *IEEE Sensors Journal*, vol. 14, pp. 2792-2800, 2014.

[2.36] P. Kassanos, I. F. Triantis, and A. Demosthenous, "A CMOS magnitude/phase measurement chip for impedance spectroscopy," *IEEE Sensor Journal*, vol. 13, pp. 2229-2236, 2013.

[2.37] S. Lee *et al*., "A low-power and compact-sized wearable bio-impedance monitor with wireless connectivity," *Journal of Physics: Conference Series (XV Int. Conf. on Electrical Bio-Impedance, ICEBI),* vol. 434, pp. 12013-12016, 2013.

[2.38] M.–C. Cho, Y.–G. Yoon, and S. Cho, "Design of highly programmable bio-impedance measurement IC in 0.18 μm CMOS", *International System-on-Chip (SoC) Conference*, pp. 79-82, 2009.

[2.39] N. Van Helleputte et al., "A 345 μW multi-sensor biomedical SoC with bio-impedance, 3-channel ECG, motion artifact reduction, and integrated DSP", *IEEE Journal of Solid-State Circuits*, vol. 50, pp. 230-244, 2015.

[2.40] J. Kirchner et al., "Heart failure monitoring with implantable defibrillators," *Biomed. Tech*., vol. 57, pp. 1079-1082, 2012.

[2.41] M. R. Cowie, "Monitoring heart failure using an implantable device measuring intrathoracic impedance – Technical and clinical overview," *Business Briefing: European Cardiology*, pp. 1-4, 2005.

[2.42] L. Wang, "Fundamentals of intrathoracic impedance monitoring in heart failure," *The American Journal of Cardiology*, vol. 99, pp. 3G-10G, 2007.

[2.43] M. Theodor *et al*., "Implantable impedance plethysmography," *Sensors*, vol. 14, pp. 14858-14872, 2014.

[2.44] W. H. Ko, "Early history and challenges for implantable electronics," *ACM Journal on Emerging Technologies in Computing Systems*, vol. 8, p. 8:1-8:9, 2012.

[2.45] J. Colomer-Ferrarons, P. Miribel-Catalá, I. Rodríguez and J. Samitier, "CMOS front-end architecture for in-vivo biomedical implantable devices," *35th Annual Conference of the IEEE Industrial Electronics*, pp. 4401-4408, 2009.

[2.46] S. Rodriguez, S. Ollmar, M. Waqar, and A. Rusu, "A batteryless sensor ASIC for implantable bio-impedance applications," *IEEE Transactions on Biomedical Circuits and Systems*, (accepted for publication), 2015.

[2.47] AD5933 Analog Devices Application Note: http://www.analog.com/en/AD5933/productsearch.html

[2.48] IEC 60601-1-2, Medical electrical equipment – Part 1-2: General requirements for safety –Collateral standard: Electromagnetic compatibility – Requirements and tests.

[2.49] F. Seoane, J. Ferreira, J. J. Sánchez, and R. Bragós, "An analog front-end enables electrical impedance spectroscopy system on-chip for biomedical applications", *Physiological Measurement*, vol. 29, pp. S267-S278, June 2008.

[2.50] AFE4300 Texas Instruments: http://www.ti.com/lit/ds/symlink/afe4300.pdf

[2.51] ADuCM350 Analog Devices Datasheet: http://www.analog.com/media/en/technical-documentation/data-sheets/ADuCM350.pdf

[2.52] J. Lamp, "Multi-channel impedance cardiography and method of multi-channel impedance cardiography," US Patent 2011/0301492, Dec. 8, 2011.

[2.53] G. D. Jindal *et al*., "Early detection of coronary heart disease using peripheral pulse analyzer," *BARC Newsletter*, Issue no. 326, pp. 15-21, May-June 2012.

[2.54] L. Ward and B. H. Cornish, "Method and device for measuring tissue oedema," US Patent 8,233,974, Jul. 31, 2012.

[2.55] M. Takeuchi *et al*., "Detecting subclinical secondary lymphoedema using bioimpedance: a preliminary study," *Journal of Lymphoedema*, vol. 8, pp. 16-20, 2013.

[2.56] R. Bayford and A. Tizzard, "Bioimpedance imaging: an overview of potential clinical applications," *Analyst,* vol. 137, pp. 4635-4643, 2012.

[2.57] J. C. Baeg *et al*., "An amplitude-to-time conversion technique suitable for multichannel data acquisition and bioimpedance imaging," *IEEE Transactions on Biomedical Circuits and Systems*, vol 7, pp. 349-354, 2013.

[2.58] Y. Yamamoto, T. Nakamura, T. Kusuhara, and Adli, "Considerations of conditions required for multi-channel simultaneous bioimpedance measurement," *Proceedings of the IEEE Instrumentation and Measurement Technology Conference*, pp. 231-234, 1998.

[2.59] S. Pyo, K. J. Loh, T.–C. Hou, E. Jarva, and J. P. Lynch, "A wireless impedance analyzer for automated tomographic mapping of a nanoengineering sensing skin," *Smart Structures and Systems*, vol. 8, pp. 139-155, July 2011.

[2.60] J. Gracia, V.–P. Seppä, J. Viik, and J. Hyttinen, "Multilead measurement system for the time-domain analysis of bioimpedance magnitude," *IEEE Transactions on Biomedical Engineering*, vol. 59, pp. 2273-2280, Aug. 2012.

[2.61] P. Annus, *Multichannel Bioimpedance Spectroscopy: Instrumentation Methods and Design Principles*, Ph. D. Thesis, Tallin University of Technology, Estonia, 2009.

[2.62] M. Min, T. Parve, A. Ronk, P. Annus, and T. Paavle, "Synchronous Sampling and Demodulation in an Instrument for Multifrequency Bioimpedance Measurement," *IEEE Transactions on instrumentation and Measurement*, vol. 56, pp. 1365- 1372, April 2007.

[2.63] J. Jossinet, "Bioimpedance and p-Health" in *Personalized Health Management Systems: The Integration of Innovative Sensing, Textile, Information and Communications Technologies* (C. D. Nugent *et al*., Eds.), pp. 35-42, IOS Press, 2005.

[2.64] U. G. Kyle *et al*., "Bioelectrical impedance analysis–part I: review of principles and methods," *Clinical Nutrition*, vol. 23, pp. 1226-1243, Dec. 2004.

[2.65] U. G. Kyle *et al*., "Bioelectrical impedance analysis–part II: utilization in clinical practice," *Clinical Nutrition*, vol. 23, pp. 1430-1453, Dec. 2004.

[2.66] M. C. Barbosa-Silva *et al*., "Bioelectrical impedance analysis: population reference values for phase angle by age and sex," *The American Journal of Clinical Nutrition*, vol. 82, pp. 49-52, July 2005.

[2.67] A. V. B. Margutti, J. P. Monteiro, and J. S. Camelo, "Reference distribution of the bioelectrical impedance vector in healthy term newborns," *British Journal of Nutrition*, vol. 104, pp. 1508-1513, Nov. 2010.

[2.68] S. B. Rutkove, P. M. Forgerson, L. P. Garmirian, and A. W. Tarulli, "Reference values for 50-kHz electrical impedance myography," *Muscle & Nerve*, vol. 38, pp. 1128-1132, Sept. 2008.

[2.69] S. C. Eror *et al.*, "Method for diagnosing disease," U.S. Patent 2010/0094160, Apr. 2010.

[2.70] R. L. Gaw, "Impedance measurement process," U.S. Patent 2011/0313311, Dec. 2011.

[2.71] H. C. Lukaski and M. G. Singer, "Phase angle as a prognostic indicator in cancer," *Computational Physiology* (*Association for the Advancement of Artificial Intelligence, Spring Symposium)*, pp. 37-39, 2011.

[2.72] J. Malmivuo and R. Plonsey, "Impedance Plethysmography" in *Bioelectromagnetism – Principles and Applications of Bioelectric and Biomagnetic Fields*, Ch. 25, pp. 405-419, Oxford University Press, 1995.

[2.73] M. –C. Cho *et al*., "A bio-impedance measurement system for portable monitoring of heart rate and pulse wave velocity using small body area," *Proc. IEEE International Symposium on Circuits and Systems (ISCAS)*, pp. 3106-3109, 2009.

[2.74] S. Lee *et al*., "A low power and convenient bio-impedance monitor and its application to respiration monitoring," *Proc. of the 4th Conference on Wireless Health*, Article No. 13, 2013.

[2.75] G. Cybulski, "Impedance Cardiography" in *Ambulatory Impedance Cardiography: The Systems and Their Applications*, Springer-Verlag, 2011.

[2.76] D. G. Jakovljevic et al. "Bioimpedance and bioreactance methods for monitoring cardiac output," *Best Practice & Research Clinical Anaesthesiology*, vol. 28, pp. 381-394, 2014.

[2.77] R. H. Bayford, "Bioimpedance tomography (Electrical impedance tomography)," *Annual Review of Biomedical Engineering*, vol. 8, pp. 63-91, Aug. 2006.

[2.78] D. –W. Kim, "Detection of physiological events by impedance," *Yonsei Medical Journal*, vol. 30, pp. 1-11, 1989.

[2.79] H. C. Lukaski, "Evolution of bioimpedance: a circuitous journey from estimation of physiological function to assessment of body composition and a return to clinical research," *European Journal of Clinical Nutrition*, vol. 67, pp. S2-S9, 2013.

Chapter 3

[3.1] "21 ideas for the 21st century," *Business Week*, pp. 78-167, Aug. 1999.

[3.2] A. Pantelopoulos and N. G. Bourbakis, "A survey on wearable sensor-based systems for health monitoring and prognosis," *IEEE Transactions on Systems, Man, and Cybernetics–Part C: Applications and Reviews*, vol. 40, pp. 1-12, Jan. 2010.

[3.3] C.–Y. Chong and S. P. Kumar "Sensor networks: evolution, opportunities, and challenges," *Proceedings of the IEEE*, vol. 91, pp. 1247-1256, Aug. 2003.

[3.4] R. Verdone, D. Dardari, G. Mazzini, and A. Conti, *Wireless sensor and actuator networks*, Academic Press, 2008.

[3.5] K. Van Dam, S. Pitchers, and M. Barnard, "From PAN to BAN: Why body area networks?," *Wireless World Research*, Second Meeting, 2001.

[3.6] G. Z. Yang, *Body sensor networks*, Springer-Verlag, 2006.

[3.7] B. Latré, B. Braem, I. Moerman, C. Blondia, and P. Demeester, "A survey on wireless body area networks," *Journal of Wireless Networks*, vol. 17, pp. 1-18, Jan. 2011.

[3.8] J. H. Nagel, "Biopotential amplifiers," *Medical devices and systems*, CRC Press, Ch. 52, pp. 1-14, 2006.

[3.9] M. A. Hanson *et al.*, "Body area sensor networks: Challenges and opportunities," *IEEE Computer*, vol. 42, pp. 58-65, Jan. 2009.

[3.10] J. H. Huijsing, "Smart sensor systems: Why? Where? How?," *Smart sensor systems*, U.K., Wiley, Ch. 1, pp. 1-21, 2008.

[3.11] A. O. Ragheb, L.A. Geddes, J. D. Bourlan, and W. A.Tacker, "Tetrapolar electrode system for measuring physiological events by impedance," *Medical & Biological Engineering & Computing*, vol. 30, pp. 115-117, Jan. 1992.

[3.12] J. L. Ausín, J. Ramos, J. F. Duque, "Unit, modular system and method for measuring, processing and remotely monitoring electrical bioimpedance," Patent Num. P201131426, 30-August-2011. International application: PCT/ES2012/070635, 29-August-2012.

Chapter 4

[4.1] S. Grimnes and Ø. G. Martinsen, Bioimpedance and Bioelectricity Basics (2nd edition), Academic Press, 2008.

[4.2] A. C. Metting van Rijn, A. Peper, and C. A. Grimbergen, "High-quality recording of bioelectric events. Part I: Interference reduction, theory and practice," Medical & Biological Engineering & Computing, vol. 28, pp. 389-397, Sept. 1990.

[4.3] J. Zhou and J. Liu, "On the measurement of common-mode rejection ratio," IEEE Transactions on Circuits and Systems–II, Express Briefs, vol. 52, pp. 49-53, Jan. 2005.

[4.4] J. Huhta and J. Webster, "60 Hz interference in electrocardiography," IEEE Transactions on Biomedical Engineering, vol. 20, pp. 91-101, March 1973.

[4.5] A. Pacela, "Collecting the body's signals," Journal of Electronics, vol. 40, pp. 103-112, July 1967.

[4.6] J. Rosell and R. Riu, "Common-mode feedback in electrical impedance tomography," Clinical Physics and Physiological Measurement, vol. 13, pp. 11-14, Jan. 1992.

[4.7] R. R. Harrison and C. Charles, "A low-power low-noise CMOS amplifier for neural recording applications," IEEE Journal of Solid-State Circuits, vol. 38, pp. 958-965, June 2003.

[4.8] R. Martins, S. Selberherr, and F. A. Vaz, "A CMOS IC for portable EEG acquisition systems," IEEE Transactions on Instrumentation and Measurement, vol. 47, pp. 1191-1196, Oct. 1998.

[4.9] M. S. J. Steyaert, W. M. C. Sansen, and C. Zhongyuan, "A micropower low-noise monolithic instrumentation amplifier for medical purposes," IEEE Journal of Solid-State Circuits, vol. 22, pp. 1163-1168, Dec. 1987.

[4.10] H. Huang, S. Karthikeyan, and E. K. F. Lee, "A 1 V instrumentation amplifier," 42nd IEEE Midwest Symposium on Circuits and Systems (MWSCAS), vol. 1, pp. 170-173, Aug. 1999.

[4.11] R. P. Areny and J. G. Webster, "AC instrumentation amplifier for bioimpedance measurement," IEEE Transactions on Biomedical Engineering, vol. 40, pp. 830-833, Aug. 1993.

[4.12] C. Kitchin and L. Counts, A Designer's Guide to Instrumentation Amplifiers, U.S.A, Analog Devices, Inc., 2000.

[4.13] M. J. Burke and D. T. Gleeson, "A micropower dry-electrode ECG preamplifier," IEEE Transactions on Biomedical Engineering, vol. 47, pp. 155-162, Feb. 2000.

[4.14] E. Spinelli, R. Pallas-Areny, and M. A. Mayosky, "AC-coupled front-end for biopotential measurements," IEEE Transactions on Biomedical Engineering, vol. 50, pp. 391-395, March 2003.

[4.15] C. J. Yen, W. Y. Chung, and M. C. Chi, "Micro-power low-offset instrumentation amplifier for biomedical system applications," IEEE Transactions on Circuits and Systems–I, Regular Papers, vol. 51, pp. 691-699, April 2004.

[4.16] E. M. Spinelli, N. Martinez, M. A. Mayosky, and R. Pallas-Areny, "A novel fully differential biopotential amplifier with DC suppression," IEEE Transactions on Biomedical Engineering, vol. 51, pp. 1444-1448, Aug. 2004.

[4.17] C.-C. Wang, C.-C. Huang, J.-S. Liou, Y.-J. Ciou, I.-Y. Huang, C.-P Li, Y.-C. Lee, and W.-J. Wu, "A mini-invasive long term bladder urine pressure measurement ASIC and system," IEEE Transactions on Biomedical Circuits and Systems, vol. 2, pp. 44-49, March 2008.

[4.18] P. Horowitz and W. Hill, The Art of Electronics, U.K., Cambridge Univ. Press, 1989.

[4.19] G. E. Tobey, J. G. Graeme, and L. P. Huelsman, Operational Amplifiers: Design and Applications, McGraw-Hill, pp. 206-207, 1971.

[4.20] F. D. Stott and C. Weller, "Biomedical amplifiers using integrated circuits," Medical and Biological Engineering, vol. 14, pp. 684-687, Nov. 1976.

[4.21] J. G. Webster, Medical Instrumentation: Application and Design, U.S.A., Houghton Mifflin Co., pp. 111-112, 1978.

[4.22] J. H. Huijsing, Operational Amplifiers: Theory and Design, U.S.A, Kluwer Academic, 2001.

[4.23] M. A. Smither, D. R. Pugh, and L. M. Woolard, "CMRR analysis of the 3-opamp instrumentation amplifier," Electronics Letters, vol. 13, pp. 594, Sept. 1977.

[4.24] M. Degrauwe, E. Vitoz, and I. Verbauwhede, "A micropower CMOS instrumentation amplifier," IEEE Journal of Solid-State Circuits, vol. 20, pp. 805-807, June 1985.

[4.25] P. M. Van Petegem, I. Verbauwhede, and W. M. C. Sansen, "Micropower high-performance SC building block for integrated low-level signal processing," IEEE Journal of Solid-State Circuits, vol. 20, pp.837-844, Aug. 1985.

[4.26] C. C. Enz and G. C. Temes, "Circuit techniques for reducing the effects of opamp imperfections: Autozeroing, correlated double sampling, and chopper stabilization," Proceedings of the IEEE, vol. 84, pp. 1584-1614, Nov. 1996.

[4.27] H. Krabbe, "A high performance monolithic instrumentation amplifier," IEEE International Solid-State Circuits Conference, pp.186-187, Feb. 1971.

[4.28] C. Toumazou, F. J. Lidgey, and D. G. Haigh, Analogue IC design: the current-mode approach, U.K., Peter Peregrinus Ltd., Ch.16, pp.569-595, 1990.

[4.29] F. L. Eatock, "A monolithic instrumentation amplifier with low input current," IEEE International Solid-State Circuits Conference. Digest of Technical Papers, pp. 148-149, Feb. 1973.

[4.30] A. P. Brokaw and M. P. Timko, "An improved monolithic instrumentation amplifier," IEEE Journal of Solid-State Circuits, vol. 10, pp. 417-423, Dec. 1975.

[4.31] R. J. van de Plassche, "A wide-band monolithic instrumentation amplifier," IEEE Journal of Solid-State Circuits, vol. 10, pp. 424-431, Dec. 1975.

[4.32] P. A. dal Fabbro and C. A. dos Reis Filho, "An integrated instrumentation amplifier with improved CMRR," 15th Symposium on Integrated Circuits and Systems Design (SBCCI), pp. 57-61, Sept. 2002.

[4.33] Y.–Q. Zhao, A. Demosthenous, and R. H. Bayford, "A CMOS instrumentation amplifier for wideband bioimpedance spectroscopy systems," Proceedings of the IEEE International Symposium on Circuits and Systems (ISCAS), pp. 5079-5082, May 2006.

[4.34] A. Worapishet, A. Demosthenous and X. Lu, "A CMOS instrumentation amplifier with 90-dB CMRR at 2-MHz using capacitive neutralization: analysis, design considerations, and implementation," IEEE Transactions on Circuits and Systems–I, Regular Papers, vol. 58, pp. 699-710, April 2011.

[4.35] B. J. van den Dool and J. H. Huijsing, "Indirect current feedback instrumentation amplifier with a common-mode input range that includes the negative rail," IEEE Journal of Solid-State Circuits, vol. 28, pp. 743-749, July 1993.

Chapter 5

[5.1] Y. Yang, J. Wang, G. Yu, F. Niu, and P. He, "Design and preliminary evaluation of a portable device for the measurement of bioimpedance spectroscopy," *Physiological Measurement*, vol. 27, pp. 1293-1310, Dec. 2006.

[5.2] P. O´Shea, Phase measurement, in *The Measurement, Instrumentation and Sensor Handbook*, J.G. Webster (ed), CRC Press, 1999.

[5.3] J. Cowles and B. Gilbert, "Accurate gain and phase measurement at radio frequencies up to 2.5 GHz," *Analog Dialogue*, vol. 35, nº. 05, Oct. 2001.

[5.4] R. W. Huggins, "Analytical fit of the transfer function of a logarithmic electrometer and correction for ambient temperature variations," *Review of Scientific Instruments*, vol. 44, pp. 297-300, March 1973.

[5.5] Y. B. Acharya and P. D. Vyavahare, "Remodeling light emitting diode in low current region," *IEEE Transactions on Electron Devices*, vol. 45, pp. 1426-1430, July 1998.

[5.6] S. Groiss and M. Koberle, "A high accurate logarithmic amplifier system with wide input range and extreme low temperature coefficient," *Proceedings of the 31st European Solid-State Circuits Conference (ESSCIRC)*, pp. 283-286, Sept. 2005.

[5.7] B. Wilson and M. Al-Gathtani, "Improved logarithmic converter based on a transconductance feedback amplifier," *IEEE International Symposium on Circuits and Systems (ISCAS)*, vol. 1, pp. 651-654, May 2001.

[5.8] A. Madjar, A. Paollela, and P. R. Herczfeld, "The compressive nature of optical detection in GaAs MESFETs and possible application as an RF logarithmic amplifier," *IEEE Transactions on Microwave Theory and Techniques*, vol. 41, pp. 165-167, Jan. 1993.

[5.9] C. Huang and S. Chakarabartty, "Current-input current-output CMOS logarithmic amplifier based on translinear Ohm´s law," *Electronics Letters*, vol. 47, pp. 433-434, March 2011.

[5.10] R. S. Hughes, *Logarithmic Amplification with Application to Radar and EW*, Artech House, 1986.

[5.11] A. Garskamp, "Logarithmic amplifier with sequentially limiting amplifier stages," U.S. Patent 5049829, Sept. 1991.

[5.12] W. L. Barber and E. R. Brown, "A true logarithmic amplifier for radar IF applications," *IEEE Journal of Solid-State Circuits*, vol. 15, pp. 291-295, June 1980.

[5.13] M. Shaterian, A. Abrishamifar, and H. Shamsi, "Analysis and design of the true piecewise approximation logarithmic amplifiers," *Analog Integrated Circuits and Signal Processing*, vol. 72, pp. 193-203, July 2012.

[5.14] J. C. Greer, "Error analysis for pseudo-logarithmic amplification," *Measurement Science Technology*, vol. 3, pp. 939-942, Oct.1992.

[5.15] P.–C. Huang, Y.–H Chen, C.–K. Wang, "A 2-V 10.7-MHz CMOS limiting amplifier/RSSI," *IEEE Journal of Solid-State Circuits*, vol. 35, pp. 1474-1480, Oct. 2000.

[5.16] R. P. Jindal, "Gigahertz-band high-gain low-noise AGC amplifiers in fine-line NMOS," *IEEE Journal of Solid-State Circuits*, vol. 22, pp. 512-521, Aug. 1987.

[5.17] C. Yang and A. Mason, "Process/temperature variation tolerant precision signal strength indicator," *IEEE Transactions on Circuits and Systems–I, Regular Papers*, vol. 55, pp. 722-729, April 2008.

[5.18] E. A. Crain and M. H. Perrott, "A 3.125 Gb/s limit amplifier in CMOS with 42 dB gain and 1 μs offset compensation," *IEEE Journal of Solid-State Circuits*, vol. 41, pp. 443-451, Feb. 2006.

[5.19] K. Kimura, "A CMOS logarithmic IF amplifier with unbalanced source-coupled pairs," *IEEE Journal of Solid-State Circuits*, vol. 28, pp.78–83, Jan. 1993.

[5.20] M. S. Steyaert, W. Dehaene, J. Craninckx, M. Walsh, and P. Real, "A CMOS rectifier-integrator for amplitude detection in hard disk servo loops," *IEEE Journal of Solid-State Circuits*, vol. 30, pp.743–751, July 1995.

[5.21] B. Razavi, *Design of Analog CMOS Integrated Circuits*, McGraw-Hill, 2001.

[5.22] D. Y. Gouda, M. Atef, A. El-Sabban, and M. El-Saba, "A low-cost 110 dB CMOS IF/limiter amplifier with offset cancellation," *Proceedings of the 15th International Conference on Microelectronics*, pp. 176-179, Dec. 2003.

[5.23] Y.–C. Chen, Y.–C. Wu, and P.–C. Huang, "A 1.2-V CMOS limiter/RSSI/demodulator for low-IF FSK Receiver," *Proceedings of the IEEE Custom Integrated Circuits Conference (CICC)*, pp. 217-220, Sept. 2007.

[5.24] P. R. Kinget, "Device mismatch and tradeoffs in the design of analog circuits," *IEEE Journal of Solid-State Circuits*, vol. 40, pp. 1212-1224, June 2005.

[5.25] K. D. Lawson and N. L. Brown, "Phase measuring circuit," U. S. Patent 4246497, Sept. 1981.

[5.26] P.–C. Huang, Y.–H. Chen, and C.–K. Wang, "A 2-V CMOS 455-kHz FM/FSK demodulator using feedforward offset cancellation limiting amplifier," *IEEE Journal of Solid-State Circuits*, vol. 36, pp. 135-138, Jan. 2001.

Chapter 6

[6.1] M. Min, T. Paavle, P. Annus, and R. Land, "Rectangular wave excitation in wideband bioimpedance spectroscopy," *IEEE International Workshop on Measurements and Applications*, pp. 268-271, May 2009.

[6.2] S. Gawad, T. Sun, N. G. Green and H. Morgan, "Impedance spectroscopy using maximum length sequences: application to single cell analysis," *Review of Scientific Instruments*, 78, 054301-1, American Institute of Physics, May 2007.

[6.3] M. Min and T. Paavle, "Broadband discrete-level excitations for improved extraction of information in bioimpedance measurements," *Physiological Measurement*, pp. 997-1010, June 2014.

[6.4] M. –C. Cho *et al.*, "A bio-impedance measurement system for portable monitoring of heart rate and pulse wave velocity using small body area," *Proceedings of the IEEE International Symposium on Circuits and Systems (ISCAS)*, pp. 3106-3109, May 2009.

[6.5] J. –W. Lee *et al.*, "Precission constant current source for electrical impedance tomography," *Proceedings of the25th Annual International Conference of the IEEE Engineering in Medicine and Biology Society*, pp. 1066-1069, Aug. 2003.

[6.6] C. –Y. Chiang *et al.*, "Portable impedance cardiography system for real-time noninvasive cardiac output measurement," *Proceedings of the 16th Annual International Conference of the IEEE Engineering in Medicine and Biology Society*, pp. 2072-2073, Nov. 1994.

[6.7] J. Frounchi, F. Dehkhoda and M.H. Zarifi, "A Low-distortion wideband integrated current source for tomography applications," *European Journal of Scientific Research*, vol. 27, pp. 56-65 , Feb. 2009.

[6.8] S. Grimnes and Ø. G. Martinsen, *Bioimpedance and Bioelectricity Basics* (2nd edition), Academic Press, 2008.

[6.9] R. González-Landaeta *et al.*, "Heart rate detection from plantar bioimpedance measurements," *IEEE Transactions on Biomedical Engineering*, vol. 55, no. 3, pp. 1163-1167, March 2008.

[6.10] H. Hong, M. Rahal, A. Demosthenous and R. H. Bayford , "Floating voltage-controlled current sources for electrical impednace tomography,"*18th European Conference on Circuit Theory and Design*, pp. 208-211, Aug. 2007.

[6.11] P. Bertemes-Filho, *Tissue Characterization Using an Impedance Spectroscopy Probe*, Ph. D. Thesis, University of Sheffield, U.K., 2002.

[6.12] D. X. Chen, X. Deng and W. Q. Yang, "Comparison of three current sources for single-electrode capacitance measurement," *Review of Scientific Instruments*, vol. 81, pp. 1-3, March 2010.

[6.13] F. Seoane, R. Bragós and K. Lindecranz, "Current source for multifrequency broadband electrical bioimpedance spectroscopy: A Novel Approach," *Proceedings of the 28th Annual International Conference of the IEEE Engineering in Medicine and Biology Society*, 3, pp. 5121-5125, Aug. 2006.

[6.14] P. Bertemes-Filho, L.H. Negri, A Felipe and V. C. Vincence, "Mirrored modified Howland circuit for bioimpedance applications: Analytical Analysis," *Journal of Physics: Conference Series*, vol. 407, nº 1, pp. 1-8, 2012.

[6.15] P. Bertemes-Filho, V. C. Vincence, M. M. Santos and I. X. Zanatta, "Low power current sources for bioimpedance measurements: a comparison between Howland and OTA-based CMOS circuits," *Journal of Electrical Bioimpedance*, vol. 3, pp. 66-73, Oct. 2012.

[6.16] L. Yang, J. Bae, S. Lee, T. Roh, K. Song and H. –J. Yoo, "A 3.9 mW 25- electrode reconfigured sensor for wearable cardiac monitoring system," *Journal of Solid State Circuits*, vol. 46, pp. 353-364, Jan. 2011.

[6.17] I. M. Gottlieb, *Practical Oscillator Handbook*, Newnes, 1997.

[6.18] G. Palumbo, M. Pennisi, and S. Penissi, "Wien-Type oscillators: Evaluation and optimization of harmonic distortion,"*IEEE Transaction on Circuits and Systems–II: Express Briefs*, vol. 55, pp. 628-632, July 2008.

Chapter 7

[7.1] M. Paavola, M. Laiho, M. Saukoski, and K. Halonen, "A micropower 2 MHz CMOS frequency reference for capacitive sensor applications," *Proceedings of the 2005 European Conference on Circuit Theory and Design (ECCTD)*, vol. 3, pp. 425-428, Sept. 2005.

[7.2] B. Razavi, *Design of Analog CMOS Integrated Circuits*, Boston: McGraw-Hill, 2000.

[7.3] MATLAB: version 8.2.0.701 (R2013b). The MathWorks Inc., Natick, MA, (2013)

[7.4] http://www.xitrontech.com/assets/002/5854.pdf

[7.5] S. Grimnes and Ø. G. Martinsen, *Bioimpedance and Bioelectricity Basics* (2nd edition), Academic Press, 2008.

[7.6] R. Buendia, *Hook Effect on Electrical Bioimpedance Spectroscopy Measurements. Analysis, Compensation and Correction*, Master Thesis, Borås University, Borås, Sweden, 2009.

[7.7] R. Buendía, F. Seoane, and R. Gil-Pita, "A novel approach for removing the hook effect artefact from electrical bioimpedance spectroscopy measurements," *Journal of Physics: Conference Series*, vol. 224, nº1, 2010.

[7.8] J.L. Ausín, J. Ramos, G. Torelli and J.F. Duque-Carrillo, "Live demonstration: A wireless multichannel bioimpedance spectrometer for patient monitoring," *in Proceedings of the IEEE Biomedical Circuits and Systems Conference (BioCAS)*, Oct. 2014.

List of publications

1. J.L Ausín, J. Ramos, G. Torelli, and J.F. Duque-Carrillo, "A programmable switched-capacitor relaxation oscillator with low phase jitter," *18th European Conference on circuit Theory and Design*, 2007.

2. J.L Ausín, J. Ramos, G. Torelli, and J.F. Duque-Carrillo, "A relaxation-oscillator-based SC square-wave generator with quasi-continuous frequency tunability," *XXII Design of Circuits and Integrated Systems*, 2007.

3. J. Ramos, J.L Ausín, G. Torelli, and J.F. Duque-Carrillo, "A ZigBee-based wireless bioimpedance monitoring system," *XXII Eurosensors Conference*, 2008.

4. J. Ramos, J.L Ausín, G. Torelli, and J.F. Duque-Carrillo, "Power consumption reduction in ZigBee-based networks using received signal strength," *XXIII Design of Circuits and Integrated Systems*, 2008.

5. J.L Ausín, J. Ramos, G. Torelli, and J.F. Duque-Carrillo, "On the design of digitally-controlled SC relaxation oscillators," *XXIII Design of Circuits and Integrated Systems*, 2008.

6. J. Ramos, A. Luque, and J. M. Quero, "Integration of a MEMS capacitive sensor in a wireless transmitter," *VII Spanish Conference on Electronic Devices*, 2009.

7. J.L Ausín, J. Ramos, G. Torelli, and J.F. Duque-Carrillo, "An area-eficient switched-capacitor relaxation oscillator with digitally controlled frequency tunability," *International Journal of Circuit Theory and Applications*, vol. 37, pp. 243-255, March 2009.

8. J. Ramos, J.L Ausín, G. Torelli, and J.F. Duque-Carrillo, "A wireless bioimpedance device for abdominal fatness monitoring," *XXIII Eurosensors Conference*, 2009.

9. J. Ramos, A. Luque , J. M. Quero, and J.L Ausín, "Design and implementation of a MEMS wireless capacitive pressure sensor," *XXIV Design of Circuits and Integrated Systems*, 2009.

10. J. Ramos, J.L Ausín, G. Torelli, and J.F. Duque-Carrillo, "BioBee: A wireless bioelectrical impedance monitoring system," *XXIV Design of Circuits and Integrated Systems*, 2009.

11. J. Ramos, J.L Ausín, G. Torelli, and J.F. Duque-Carrillo, "A wireless sensor network for fat and hydration monitoring by bioimpedance analysis," *VI International Workshop on Wearable Micro and Nano Technologies for Personalized Health*, 2009.

12. J. Ramos, J.L Ausín, G. Torelli, and J.F. Duque-Carrillo, "A 1-MHz analog front-end for a wireless bioelectrical impedance sensor," *6th Conference on Ph.D. Research in Microelectronics & Electronic*, 2010.

13. J. Ramos, J.L Ausín, G. Torelli, and J.F. Duque-Carrillo, "Design of limiting/logarithmic amplifier for wideband bioimpedance measuring devices," *Biomedical Circuits and Systems Conference (BioCAS)*, 2010.

14. J. Ramos, J.L Ausín, G. Torelli, and J.F. Duque-Carrillo, "A 1-MHz 65-dB limiting/logarithmic amplifier for wideband bioimpedance measuring devices," *XXV Design of Circuits and Integrated Systems*, 2010.

15. J. Ramos, J.L Ausín, G. Torelli, and J.F. Duque-Carrillo, "Design considerations on CMOS limiting amplifiers for wearable biomedical systems," *20th European Conference on Circuit Theory and Design*, 2011.

16. J.L Ausín, J. Ramos, G. Torelli, and J.F. Duque-Carrillo, "High-sensitivity power-efficient limiting amplifier for bioimpedance phase angle detectors," *Biomedical Circuits and Systems Conference (BioCAS)*, 2011.

17. J. Ramos, J.L Ausín, G. Torelli, and J.F. Duque-Carrillo, "Design tradeoffs for sub-mW CMOS biomedical limiting amplifiers," *XXVI Conference of Design of Circuits and Integrated Systems*, 2011.

18. J. Ramos, J.L Ausín, G. Torelli, and J.F. Duque-Carrillo, "Wideband low-power current-feedback instrumentation amplifiers for bioelectrical signals," *9th Multi-Conference on Systems Signals & Devices (SSD)*, 2012.

19. J. Ramos, J.L Ausín, G. Torelli, and J.F. Duque-Carrillo, "A high dynamic range wideband CMOS phase angle detector for bioimpedance spectroscopy," *19th IEEE International Conference on Electronics, Circuits and Systems*, 2012.

20. J.L Ausín, J.F. Duque-Carrillo, J. Ramos and G. Torelli, *Pervasive and Mobile Sensing and Computing for Healthcare*, Chp. "From Handheld Devices to Near-Invisible Sensors: The Road to Pervasive e-Health," pp. 135-156, I.S.B.N. 978-3-642-32537-3, 2013.

21. J. Ramos, J.L Ausín, A. M. Lorido, F. Redondo and J.F. Duque-Carrillo, "A wireless, compact, and scalable bioimpedance measurement system for energy-efficient multichannel body sensor solutions," *XVth International Conference on Electrical Bio-Impedance (ICEBI) and XIVth Conference on Electrical Impedance Tomography (EIT)*, 2013.

22. J. Ramos, J.L Ausín, A. M. Lorido, F. Redondo and J.F. Duque-Carrillo, "A wireless multichannel bioimpedance measurement system for personalized healthcare and lifestyle," *10th International Conference on Wearable Micro and Nano Technologies for Personalized Health (pHealth)*, 2013.

23. J. Ramos, J.L Ausín, G. Torelli, and J.F. Duque-Carrillo, "Design tradeoffs for sub-mW CMOS biomedical limiting amplifiers," *Microelectronics Journal*, vol. 44, pp. 904-911, Oct. 2013.

24. J. Ramos, J.L Ausín, A. M. Lorido, F. Redondo and J.F. Duque-Carrillo, "Live demonstration: A wireless multichannel bioimpedance spectrometer for patient monitoring," *Biomedical Circuits and Systems Conference (BioCAS)*, 2014.

25. J. L. Ausín, J. Ramos, J. F. Duque, "Unit, modular system and method for measuring, processing and remotely monitoring electrical bioimpedance," Patent Num. P201131426, 30-August-2011. International application: PCT/ES2012/070635, 29-August-2012.